

IMPROVING MACHINE TOOL DESIGN THROUGH NOVEL ANALYTICAL
AND NUMERIC METHODS

by
ESRA YÜKSEL

Submitted to the Graduate School of Engineering and Natural Sciences in partial fulfilment
of the requirements for the degree of
Doctor of Philosophy

Sabancı University
July 2023

IMPROVING MACHINE TOOL DESIGN THROUGH NOVEL ANALYTICAL
AND NUMERIC METHODS

APPROVED BY:

Prof. Dr. Erhan Budak.....
(Thesis Supervisor)

Prof. Dr. Yusuf Mencelođlu.....

Prof. Dr. Mustafa Bakkal.....

Assoc. Prof. Dr. Lutfi Taner Tunç.....

Assist. Prof. Dr. Orkun Özşahin.....

DATE OF APPROVAL: 25/07/2023

© Esra Yüksel 2023
All Rights Reserved

ABSTRACT

Improved machine tool designs enable countless advantages for process improvement and energy saving, bringing competitiveness. This study presents novel analytical and numeric methods for machine tool design improvements. One of the significant difficulties during numerical machine tool simulations is mechanical interface modeling. The variational inequalities are based on numerical and analytical contact methods. This study introduces Signorini's Contact Problem as a new aspect of machine tool research. Additionally, the FE implementation of the Signorini problem is presented, along with a detailed explanation of thermo-mechanical contact elements in FE. A novel contact interface method RCFM (Reflected Contact Force Method) is presented. The topology optimization problem with contact constraints has been introduced. The importance of mechanical interfaces becomes significant during the design phase of large-scale machine tools. This study demonstrates the analyses and optimization of large-scale gantry and horizontal milling machines with experimental results on manufactured prototypes by considering the mechanical interfaces (with RCFM). Critical points in designing and optimizing large-scale machine tools are discussed. The extension of the RCFM method for Level-Set Topology Optimization (LSTO) is demonstrated on a gantry structure. As well as large-machine tools, the mechanical interfaces become significant during the design of ultra-high-speed spindles since these structures have thousands of interfaces. This study details developing specifications, strategies, and design layouts for a 40 000-rpm spindle. The presented spindle will be optimized and manufactured in the laboratory. Therefore, virtual models of high-speed spindle structures are created using RCSA, bearing, and thermal ROMs (Reduced Order Models) in an optimization platform developed explicitly for fast spindle design. The developed optimization platform is much more potent than other spindle optimization platforms since the ROMs can give FE simulation flexibility and power while offering the speed of analytical models.

Keywords: Contact Interface, Structural Optimization, Large Machine Tools, High-Speed Spindles, Fast Thermal and Dynamic Modelling

ÖZET

Yapısal olarak iyileştirilmiş takım tezgâhı tasarımları, süreç iyileştirme ve enerji tasarrufu vb. gibi açılardan sayısız avantaj sağlayarak rekabet gücü sağlar. Bu çalışma, takım tezgâhı tasarımı iyileştirmeleri için yeni analitik ve nümerik yöntemler sunmaktadır. Nümerik takım tezgâhı simülasyonları sırasındaki önemli zorluklardan biri mekanik kontak yüzeylerinin modellemesidir. Varyasyonel eşitsizlikler metodu sayısal ve analitik temas yöntemlerine dayanmaktadır. Bu çalışma, Signorini'nin Kontak Problemini takım tezgâhı araştırmasının yeni bir yönü olarak ele almaktadır. Ek olarak, Signorini probleminin Sonlu Eleman (FE) uygulaması, sonlu eleman metodunda termo-mekanik kontak elemanlarının ayrıntılı bir açıklamasıyla birlikte sunulmaktadır. Yeni bir kontak arayüzü yöntemi RCFM (Yansıtılmış Kontak Kuvveti Yöntemi) önerilmiştir. Kontak modellerini kısıt olarak alan topoloji optimizasyon problemi tanıtıldı. Büyük ölçekli takım tezgahlarının tasarım aşamasında mekanik kontak yüzeyleri daha da önem kazanmaktadır. Bu çalışma, büyük ölçekli portal ve yatay frezeleme makinelerinin mekanik kontak yüzeyleri (RCFM ile) dikkate alınarak üretilen prototipler üzerinde deneysel sonuçlarıyla analiz ve optimizasyonunu göstermektedir. Büyük ölçekli takım tezgahlarının tasarlanması ve optimize edilmesindeki kritik noktalar tartışılmaktadır. Düzey Ayarlı Topoloji Optimizasyonu (LSTO) için RCFM yönteminin uzantısı, bir portal yapısı üzerinde gösterilmiştir. Büyük takım tezgahlarının yanı sıra, ultra yüksek hızlı iş millerinin tasarımı sırasında mekanik arayüzler de bu yapıların binlerce arayüze sahip olması nedeniyle önem kazanmaktadır. Bu çalışma, 40.000 devir/dakikalık bir iş mili için geliştirme spesifikasyonlarını, stratejilerini ve tasarım düzenlerini ayrıntılarıyla anlatmaktadır. Sunulan iş mili laboratuvarında optimize edilecek ve üretilecektir. Bu nedenle, hızlı iş mili tasarımı için özel olarak geliştirilmiş bir optimizasyon platformunda RCSA, rulman ve termal ROM'lar (İndirgenmiş Sıralı Modeller) kullanılarak yüksek hızlı iş mili yapılarının sanal modelleri oluşturulur. Geliştirilen optimizasyon platformu, diğer iş mili optimizasyon platformlarından çok daha güçlüdür çünkü ROM'lar analitik modellerin hızını sunarken FE simülasyon esnekliği ve gücü de verebilir.

Anahtar Kelimeler: Kontak Yüzeyi, Yapısal Modelleme, Büyük Takım Tezgâhları, Yüksek Hızlı İş Milleri, Hızlı Termal ve Dinamik Modelleme

TABLE OF CONTENTS

ABSTRACT.....	4
ÖZET	5
TABLE OF CONTENTS.....	6
LIST OF FIGURES	9
LIST OF TABLES.....	13
Introduction.....	14
1. Machine Tool Interface Numerical Modelling Methods and Effects on Machine Tool Structural Analysis and Optimization.....	17
1.1. Summary and Novelty.....	17
1.2. Introduction	17
1.3. Research Gap.....	19
1.4. FE Formulation of Contact Problem	20
1.4.1. Signorini Contact Problem.....	20
1.4.2. Implementation to FE Solver	21
1.4.3. Contact Force in FE model	23
1.5. FE Formulation of Thermo-mechanical Contact Problem.....	25
1.6. FE Contact Algorithms and Effects on Topology Optimization.....	26
1.6.1. FE Contact Algorithms and Strain Energy Transmission.....	26
1.6.2. Topology Optimization Problem Statement	27
1.6.3. Example Application	28
1.7. The Proposed Novel Contact Solutions	29
1.7.1. RCFM Method	29
1.7.2. The RCFM Formulation of Contact Problem	31
Contact Force in the RCFM.....	31
1.8. Thermo-Mechanical RCFM Method.....	31
1.9. The Contact Representation and Experimental Identification of Contact Parameters	32
1.10. Topology Optimization and Contact Implementation of RCFM.....	34
1.10.1. Topology Optimization with RCFM.....	34
1.10.2. Topology Optimization with Thermo-mechanical RCFM	36
1.11. Machine Tool Application.....	36
1.11.1. Topology Optimization with RCFM.....	37

1.11.2.	Topology Optimization with Thermo-mechanical RCFM	37
1.12.	Results	38
1.12.1.	Results of Topology Optimization with RCFM	38
1.12.2.	Results of Topology Optimization with Thermo-mechanical RCFM	42
1.13.	Conclusions	44
2.	Design And Analysis of Large-Scale Milling Machines by Considering Mechanical Interfaces.....	45
2.1.	Summary and Novelty.....	45
2.2.	Introduction	45
2.3.	Research Gap.....	46
2.4.	Design of Large Machine Tools.....	47
2.5.	Large-Scale Gantry Type Machine Tools	48
2.5.1.	FE Analyses	49
2.5.2.	Deflection Analysis.....	49
2.5.3.	Modal Analysis	51
2.5.3.1.	IGM FR 3500.....	51
2.5.3.2.	IGM FR 3500 XL	52
2.6.	Experimental Results.....	54
2.6.1.	IGM FR 3500 Modal Investigation.....	54
2.6.2.	IGM FR 3500 XL Modal Investigation	57
2.7.	Topology Optimization	60
2.7.1.	Topology Optimization Problem	60
2.7.2.	Topology Optimization Results	60
2.7.3.	Modal Analysis Results	61
2.8.	Large-Scale Horizontal Milling Machine	61
2.8.1.	FE Analyses	62
2.8.2.	Body Analyses	62
2.8.2.1.	Deflection Analysis	62
2.8.2.2.	Modal Analysis.....	67
2.9.	Topology Optimization	70
2.10.	Critical Points and Conclusions.....	72
3.	Conceptual Design of a High-Speed Spindle	75
3.1.	Summary and Novelty.....	75
3.2.	Introduction	75
3.3.	Research Gap.....	76

3.4.	Fundamental Spindle Components.....	77
3.5.	Campbell Diagram Using FE Simulations	78
3.5.1.	Optimization Problem Statement:.....	80
3.5.2.	Optimization Results for Mode of the critical speed 100 000 RPM.....	81
3.6.	Auxiliary Spindle Components	81
3.7.	Lubrication and Drainage System	86
3.8.	Final Spindle Design and Manufacturing Details	87
3.8.1.	The Shaft Design	87
3.8.2.	Housing Design	91
3.8.3.	Preloading Mechanism Design.....	94
3.8.4.	Bearing Preload Selection and First Optimization	96
3.8.4.1.	Case Study: Dynamic Optimization.....	102
3.8.5.	Cooling System Design Alternatives	104
3.8.6.	Bearing Lubrication System	107
3.8.7.	Labyrinth Seals and Stepped Sleeve Designs	108
3.8.7.1.	Stepped Sleeves for Locking	108
3.8.7.2.	Labyrinth Seals and Pneumatic Sealing Channels	109
3.9.	Conclusions	110
4.	Virtual Modelling of a High-Speed Spindle Structure for Optimization	111
4.1.	Summary and Novelty.....	111
4.2.	Introduction	111
4.3.	Research Gap.....	112
4.4.	Dynamic and Thermal Modelling	113
4.4.1.	Bearing Modelling	113
4.4.2.	Dynamic Modelling	115
4.4.3.	Thermal Modelling	116
4.5.	Reduced Order Models (ROMs) for Optimization Studies.....	117
4.6.	Rotating auxiliary components and shaft design.....	120
4.7.	Sensitivity analysis.....	121
4.7.1.	Dynamic Sensitivity	122
4.7.2.	Thermal sensitivity	125
4.8.	Optimization case study	126
4.9.	Discussion	126
4.10.	Conclusions	129
5.	References.....	130

LIST OF FIGURES

Fig. 1.1 The descriptive monograph of the HSM conditions.....	20
Fig. 1.2 The penalized contact stiffness monograph.....	24
Fig. 1.3 The contact of half cubes: a) The loading conditions and total deformation, b) Deformation at X axis, c) Contact surface, d) Oscillated contact pressure.	24
Fig. 1.4 Contact force variations for different computational methods in FE.	25
Fig. 1.5 The strain energy profiles for the contacted beams.	27
Fig. 1.6 Topology optimization results of the bottom part of the cube assembly with complete and sectional views: a) the Penalty Method; b) the Lagrange Method.....	29
Fig. 1.7 Hybrid Framework of the Reflected Contact Force Method (RCFM).	30
Fig. 1.8 The proposed virtual representation of the thermo-mechanical contact in FE environment	33
Fig. 1.9 (a) Experimental force-deflection graph (b) Experimental thermal work-deflection.	34
Fig. 1.10 Topology optimization results of the bottom part of the cube assembly with complete and sectional views a) the Penalty Method b) the Lagrange Method c) Reflected Contact Force Method.....	35
Fig. 1.11 a) The modelled machine tool structure model. Positions of the machine tool's axes for test conditions: b) rigid c) flexible	37
Fig. 1.12 The topology optimization for different contact methods (a) the PCM, (b) the RCFM.	38
Fig. 1.13 Strain energy densities in the guide sets for both contact methods.	38
Fig. 1.14 The topology optimization results through (a, b, c) the single component optimization, (d, e, f) the PCM, (g, h, i) the RCFM.	39
Fig. 1.15 Dynamic response of the optimized machine tool at: (a) the most flexible, (b) the stiffest position.....	41
Fig. 1.16 Total deflection [mm] of the structure under (a) thermal loading (b) coupled loading.....	42
Fig. 1.17 The results of thermal top. opt. (a) the assembly (b) the spindle holder (c) the ram and (d) the sliding carriage	43
Fig. 1.18 The results of static top. opt. (a) the assembly (b) the spindle holder (c) the ram and (d) the sliding carriage	43
Fig. 2.1 Casting method benefited design strategies a.) The rack and pinion system used for linear motion system, b.) The pretensions on the gantry surface due to casting, and cast rails of linear guideways, c.) The pipeline locations for the cooling of main frame	47
Fig. 2.2 CAD data of the subjected 5-axis CNC with general machine coordinates.	48
Fig. 2.3 The total static deformation of the CNC under gravitational force at the least stiff position.....	50
Fig. 2.4 The directional static deformation results of the CNC under gravitational force at the least stiff position. a) X-axis, b) Y-axis, c) Z-axis.....	50
Fig. 2.5 The mode shapes from the FE analysis a) 1st Mode (21.8 Hz), b) 2nd Mode (23.9 Hz), c) 3rd Mode (41.8 Hz).	52
Fig. 2.6 The mode shapes from the FE analysis a) 4th Mode (43.8 Hz), b) 5th Mode (64.2 Hz), c) 6th Mode (69.3 Hz).....	52
Fig. 2.7 The mode shapes from the FE analysis a) 1st Mode (36 Hz), b) 2nd Mode (42 Hz).	53

Fig. 2.8 The mode shapes from the FE analysis a) 3rd Mode (50 Hz), b) 4th Mode (79 Hz), c) 5th Mode (80 Hz).....	53
Fig. 2.9 IGFR3500 XL has an extended main body structure.	54
Fig. 2.10 The location and reference X-Y plane of the accelerometers, and the hammer tests at a.) the Main Bodies b.) the Gantry c) the Spindle for IGM FR 3500.	54
Fig. 2.11 The location and reference X-Y plane of the accelerometers, and the hammer tests at a.) the Main Bodies b.) the Gantry c) the Spindle for IGM FR 3500 XL.....	57
Fig. 2.12 a.) Front view of the optimized design, b.) Rear view of the optimized design c.) Initial and optimized design.....	61
Fig. 2.13 a.) 1st Mode: 132 Hz, b.) 2nd Mode:145 Hz c.) 3rd Mode: 191Hz for the optimized gantry	61
Fig. 2.14 a.) Original CAD Model b.) Simplified CAD Model for FE.	62
Fig. 2.15 a.) Deformation of the bench under its weight, b.) Local Deformation (Total)	63
Fig. 2.16 a) Y-direction deformation of machine under its weight, b.) Local deformation (Y-direction).....	63
Fig. 2.17 a) Z-direction deformation of machine under its weight, b.) Local deformation (Z-direction).....	64
Fig. 2.18 X-direction deformation of machine under its weight.....	64
Fig. 2.19 a) Equivalent Stress under its weight, b.) Equivalent Strain, c.) Shear Stress for YZ Axis.....	65
Fig. 2.20 Stain energy distribution under the machine weight.	65
Fig. 2.21 Deformation of the worktable under its weight.....	66
Fig. 2.22 X-direction deformation of the machine under its weight.....	66
Fig. 2.23 Y-direction deformation of the machine under its weight.....	67
Fig. 2.24 Z-direction deformation of the machine under its weight	67
Fig. 2.25 Tower part a.) 1st Mode:14.9 Hz , b.) 2nd Mode: 16.9 Hz, c.) 3rd Mode: 48.4 Hz.68	
Fig. 2.26 Tower part a.) 4th Mode: 74.4 Hz , b.) 5th Mode: 78Hz, c.) 6th Mode: 88.1 Hz ...69	
Fig. 2.27 Worktable part a.) 1st Mode: 23 Hz , b.) 2nd Mode: 80 Hz, c.) 3rd Mode: 106.6 Hz.....	69
Fig. 2.28 Worktable part a.) 4th . Mode: 114.8 Hz , b.) 5th Mode: 126.7 Hz, c.) 6th Mode: 128.2 Hz.....	70
Fig. 2.29 Topology optimization a.) Isometric from the Front b.) Isometric from the left c.) From the front, d.) Isometric from the back.....	71
Fig. 3.1 The meshed CAD model of the test spindle.....	78
Fig. 3.2 The Campbell diagram for the test spindle.....	79
Fig. 3.3 The parametrized shaft radiuses and the optimization problem.....	81
Fig. 3.4 The optimized shaft radiuses for 100 K rpm critical speed.....	81
Fig. 3.5 Bearing Spacers	82
Fig. 3.6 Plain and flange type of stepped sleeves to lock bearings.....	83
Fig. 3.7 Labyrinth Seal Design for Rear Bearing	83
Fig. 3.8 a.) Axial and radial labyrinth seals, b.) flingers to avoid lubricant leakage and dirt contamination.....	84
Fig. 3.9 The multi-functional stepped sleeves designed for the MRL-40K.....	84
Fig. 3.10 10 The multi-functional labyrinth seals designed for the MRL-40K.	85
Fig. 3.11 Constant preload mechanism example	86
Fig. 3.12 The designed compact constant preload mechanism for the MRL-40K	86

Fig. 3.13 The designed lubrication and drainage system for the MRL-40K	87
Fig. 3.14 The shaft diameters for the final design	87
Fig. 3.15 The bearing location on the shaft for the final design	88
Fig. 3.16 The motor location and dimension comparison	89
Fig. 3.17 The oil pressurized area for motor dismantling.....	90
Fig. 3.18 The comparison of the initially selected and lastly chosen encoders.	90
Fig. 3.19 The balance ring example from an industrialized 42 000 rpm spindle [57].....	91
Fig. 3.20 The balance rings for the new spindle (40 000 rpm).....	91
Fig. 3.21 The housing design for the front bearings	92
Fig. 3.22 The housing design for the rear bearings.....	93
Fig. 3.23 The cooling region areas for the spindle housing.....	93
Fig. 3.24 The cooling region dimensions for the spindle housing.....	94
Fig. 3.25 The cooling regions for a High-speed and torque Fisher Spindle [58]	94
Fig. 3.26 The preload distribution for ‘O’ configuration with different bearing numbers [59]	95
Fig. 3.27 The preload distribution for ‘O’ configuration with same bearing numbers.....	95
Fig. 3.28 The factory preload adjustment components.....	96
Fig. 3.29 The external preload adjustment components	96
Fig. 3.30 Displacement Curve for Single Angular Contact Ball Bearing.....	98
Fig. 3.31 Factory/Mounting Preload.....	99
Fig. 3.32 Rigid Preloading in Back-to-Back (DB) Arrangement [60,61].....	99
Fig. 3.33 Displacement Curves for Selected Front and Rear Bearing Sets	100
Fig. 3.34 Application of Spring Force	101
Fig. 3.35 Application of Additional Axial Preload.....	101
Fig. 3.36 Bearing Curves for Constant Preload Mechanism [61].....	102
Fig. 3.37 FRF Comparison for MRL spindle with the base spindle	103
Fig. 3.38 Cooling channel designs from different spindle manufacturers [65, 66].	104
Fig. 3.39 Helix cooling channel designs	105
Fig. 3.40 Parallel cooling channel designs.....	105
Fig. 3.41 Parallel cooling channel designs.....	106
Fig. 3.42 The fin structure of the final cooling sleeve design.....	106
Fig. 3.43 The pneumatic inlets and outlets natural convection enhancement	107
Fig. 3.44 The hydraulic inlets and outlets for the front bearing lubrication system	108
Fig. 3.45 The hydraulic inlets and outlets for the rear bearing lubrication system.....	108
Fig. 3.46 The stepped sleeves for the final spindle design	109
Fig. 3.47 The labyrinth sleeves and pneumatic inlet & outlets for the final spindle design..	109
Fig. 4.1 The offered optimization components for dynamic and thermal behavior prediction	113
Fig. 4.2 Bearing coordinate systems and ball free-body diagram, a.) Global coordinate system, b.) Local coordinate system, and c.) Free-body diagram of the bottom ball.	114
Fig. 4.3 Rigid coupling of two substructures	115
Fig. 4.4 The workflow from CAE to ROMs.....	118
Fig. 4.5 The simplified shaft-bearing structure for ROM studies.....	118
Fig. 4.6 The temperature distribution for shaft cooling for ROM studies	119
Fig. 4.7 The thermal growth for shaft cooling for ROM studies	119
Fig. 4.8 The shear safety factor for ROM studies (Shaft Hole Radius:10.5 mm)	119

Fig. 4.9 The normal safety factor for ROM studies (Shaft Hole Radius:10.5 mm).....	120
Fig. 4.10 Spindle shaft auxiliary components and adjustable dimensions	121
Fig. 4.11 Spindle-tip FRF with and without auxiliary components.....	122
Fig. 4.12 Summary of sensitivity analysis	123
Fig. 4.13 Sensitivity of front stepped sleeve length.....	123
Fig. 4.14 Tail length sensitivity	124
Fig. 4.15 Sensitivity of shaft hole radius	125
Fig. 4.16 Thermal sensitivity of shaft's central hole	125
Fig. 4.17 FRF's of pareto optimal solutions.....	128

LIST OF TABLES

Table 1.1 Contact-coupled Optimization Problem Statement by Employing the Penalty Method	28
Table 1.2 The Tangent Matrix Data Transition from Computational to Experimental Method	32
Table 1.3 Contact-coupled Optimization Problem Statement by employing the RCFM.	34
Table 1.4 Problem Statements with Thermo-Mechanical Contact Constraints for Static and Thermal Compliance.....	36
Table 1.5 Reduced Volume Percentage of Different Optimization Types	40
Table 2.1 The axial strokes of IGM FR series.	48
Table 2.2 The modal analysis results for the first 6 modes of IGM FR 3500.	51
Table 2.3 The modal analysis results for the first 5 modes of IGM FR 3500 XL.	52
Table 2.4 The Comparison of results obtained from the FE and impact hammer tests for the body columns for IGM FR 3500.....	55
Table 2.5 The Comparison of results obtained from the FE and impact hammer tests for the gantry for IGM FR 3500.	55
Table 2.6 The most flexible modes of the Spindle and Z column measured by impact hammer tests for IGM FR 3500.	56
Table 2.7 The Comparison of results obtained from the FE and impact hammer tests for the body columns for IGM FR 3500 XL.	57
Table 2.8 The Comparison of results obtained from the FE and impact hammer tests for the gantry for IGM FR 3500 XL.....	58
Table 2.9 The most flexible modes of the Spindle and Z column measured by impact hammer tests for IGM FR 3500 XL.....	59
Table 2.10 Modal Analysis Results	68
Table 2.11 Modal Analysis Results for Optimized Spindle Support Tower	71
Table 3.1 The speed-dependent modes for the test spindle	80
Table 3.2 FRF Optimization Results for Selected Bearings and Final Design.....	103
Table 4.1 Upper and lower bounds of variable dimensions.....	121
Table 4.2 Pareto optimal solutions.....	127

1. INTRODUCTION

This thesis focuses on improving machine tool design by employing novel analytical and numerical models. Today, digital twins and AI require data to create and train machine tool models. The most serious difficulty for analytical and numerical structural models is modeling the mechanical interfaces. The offered theoretical contact models cannot predict more complicated failure mechanisms such as plastic deformation. Furthermore, many of these contact models only apply to a few components with surface stresses. These reasons make the contact theory insufficient for many precision engineering applications. Other than mentioned theoretical reasons, in a contact problem, the actual contact surface on which bodies meet is unknown before the application of loads to a body. The boundary conditions on this unknown surface include unknown stresses and displacements. As a result, mathematical models of contact involve systems of inequalities or nonlinear equations. These nonlinearities cause numerical instability problems and bring a massive computational burden.

Regarding these challenges, the most dominant effect can be seen in topology optimization applications with contact constraints. Most commercial FE (Finite Element) software does not guarantee the predictability of the contact stiffness if it exceeds 10^{16} N/mm. Still, most of the software assigns contact forces higher than this limit. Since topology optimization applications are based on strain energy, transmitting accurate strain energies between the bodies becomes crucial to obtain a reliable optimized structure. Another problem from the practical FE application point of view is related to dynamic and transient analyses. Even a simple modal analysis of machine assembly is more accurate with node sharing between the mechanical interfaces. It gives more precise results than employing built-in contact algorithms in FE software. Thermo-mechanical contact behavior prediction is another problematic issue in FE since contact force changes affect the contact conduction coefficients and evolving boundary conditions at the contact area affected by both changing contact conditions and time.

Machine tool assemblies need to be stiff, accurate, and precise to meet challenging requirements improvements are a necessity, and the cheapest way to achieve this aim is by creating accurate and detailed digital models. However, even a simple spindle assembly consisting of thousands of contact elements and predictions for time-dependent, thermo-mechanical, and dynamic models requires long computational

iterations, which makes machine tool and spindle design and improvements cumbersome and challenging. Therefore, this study addresses the challenges regarding mechanical interface modeling for machine tool bodies and spindle structures. The misleading effect of contact algorithms in FE and topology optimization algorithms are demonstrated, which is a first in the literature to the best of our knowledge. During this research study, Novel numerical mechanical interface modeling methods are offered tailored explicitly for machine tool bodies and ultra-high-speed spindles. First, a novel contact interface modeling method that considers thermo-mechanical and topology optimization applications is submitted called Reflected Contact Force Method (RCFM). The contact forces are greater in large-machine tools, and designing large but lightweight machine tools brings a competitive advantage by offering energy efficiency and physical capability improvements with increased speed, acceleration, and jerk limits. Large-machine tools are investigated by employing RCFM and existing FE software together with structural optimization and improvement suggestions to benefit from all these advantages for machine tool design and improvement. The accuracy and efficacy of the offered method and improvement suggestions are demonstrated on the manufactured prototypes of exceedingly large two 5-axis gantries and a horizontal milling machine.

Like the large-machine tools, spindle structures also involve thousands of mechanical interfaces in a tiny volume compared to machine tool bodies, making mechanical interface modeling more vital. Mechanical interface modeling becomes more critical when the spindle sizes become smaller since the smaller spindles are generally associated with high-speed spindles. A high-speed spindle design requires special considerations due to the desired speed thresholds and components with speed needs. Another challenge is the optimization of a high-speed structure is a challenge due to two main reasons. First, dynamic, and thermal behavior improvements conflict and require a trade-off between the optimization objectives.

The second problem is the design iterations of compact spindle structures require the change of the entire assembly in many cases. When this design challenge is combined with the long simulation hours, developing, and optimizing a high-speed spindle becomes exceedingly expensive, time-consuming, and cumbersome. In this research study, concerning all these challenges, a novel thermo-mechanical contact interface modeling method is offered, improving the prediction accuracy, and significantly reducing simulation time. As mentioned, a small change can result in a change in

spindle design, and optimization of a spindle requires consideration of many parameters and a trade-off between them. In this research, developing specifications, strategies, and design layouts for a 40 000-rpm spindle. The presented spindle will be optimized and manufactured in the laboratory. Therefore, virtual models of high-speed spindle structures are created using RCSA, bearing, and thermal ROMs (Reduced Order Models) in an optimization platform developed explicitly for fast spindle design. The developed optimization platform is much more potent than other spindle optimization platforms since the ROMs can give FE simulation flexibility and power while offering the speed of analytical models. Another challenge for mechanical interface modeling and optimization studies is simulation times for thermo-mechanical analyses. Thus, this study provides a novel method to speed up the transient thermal spindle FE analysis. This study uses thermal modal analysis to determine time coefficients to predict transient to steady state behavior. Element birth and death methods are used in FE to turn transient analysis into a steady state analysis to predict the temperature and thermal growth in spindle structures.

1. MACHINE TOOL INTERFACE NUMERICAL MODELLING METHODS AND EFFECTS ON MACHINE TOOL STRUCTURAL ANALYSIS AND OPTIMIZATION

1.1. Summary and Novelty

When it comes to numerical machine tool simulations, one of the most challenging aspects is mechanical interface modeling. Variational inequalities typically rely on numerical and analytical contact methods, but there is a new approach that has been gaining attention in the field. This is Signorini's Contact Problem, which has a lot of potential for machine tool research. To expand on this, the FE implementation of the Signorini problem has been presented, along with a detailed explanation of thermo-mechanical contact elements in FE. Another exciting development is the introduction of a novel contact interface method called RCFM (Reflected Contact Force Method). Finally, the topology optimization problem with contact constraints has been addressed in this research.

1.2. Introduction

In a machine tool, a mechanical interface plays a crucial role. It comprises two surfaces that may or may not be of the same material, and they are either in contact or separated by a medium such as oil, lubricant, or air. The primary purpose of this interface is to provide support to the joint's mating components while maintaining the desired degree of freedom. The performance of machine tool interfaces has a significant impact with the possibilities of lower friction, less heat generation, better precision and motion accuracy, and increased rigidity on the overall effectiveness of machine tools. As such, researchers have invested a great deal of time and resources into studying these interfaces and identifying ways to improve their functionality. By doing so, they hope to enhance the performance of machine tools and ultimately help manufacturers achieve their production goals more efficiently and effectively [1].

Mechanical interface modelling bases contact problems in elasticity for many engineering applications. In essence, the contact of two deformable bodies is how loads are delivered in a structure or mechanism to sustain loads. It is obvious, therefore, that the character of this contact may play a fundamental role in the behavior of the structure: its deformation, its motion, the distribution of stresses, etc.

In a contact problem, prior to the application of loads to a body, the actual contact surface on which bodies meet is unknown. The boundary conditions on this unknown surface includes unknown stresses and displacements. As a result, mathematical models of contact involve systems of inequalities or nonlinear equations. These types of mathematical problems are classified as variational inequalities.

The general equilibrium of the contact problem using variational inequalities is known as Signorini's contact problem in the literature [2]. The classical Signorini problem in elasticity defines the equilibrium of a linearly elastic body in contact with a frictionless rigid foundation formulated by Signorini in 1933, who presented a complete account of his theory in 1959 [3].

The solution for variational inequality problems can be accomplished through analytical and numerical methods. Simplified 2-D contact problems that feature curved axisymmetric

profiles (Hertz-type problems), or punch problems can be resolved using analytical techniques. Hertz, in the field of elasticity, investigated a static contact problem by considering the balance of two elastic bodies in contact on surfaces whose projections in the plane were conic sections. He came up with formulas for the contact pressure and indentation, assuming that the contact area was confined within an ellipse. Hertz's findings can be applied to several specific problems, including the contact of a circular cylinder or a sphere with a rigid foundation, half-cylinders on foundations, and more which can be defined as a narrowed down version of a classical Signorini problem. Such issues are known as Hertz-type or Hertzian contact problems. Punch problems, on the other hand, are generally assumed with a rigid indenter and an elastic foundation. The geometry and loading in the classical punch problems are usually simple and ideal, and the contact surface is assumed to be known in advance. For such problems, analytical methods such as those employing the theory of linear integral equations, complex potentials, and conformal maps are particularly well-suited for analysis.

Variational inequalities have proven to be a highly effective tool for generating precise approximations and numerical methods. In the solution phase of complex contact problems, numerical methods are frequently employed as the preferred solution. To use numerical methods in complex contact problems the most prominent study was made by Fichera. The research of Fichera [4] delves into the subject of existence and uniqueness of variational inequalities that emerge from the minimization of functionals on convex subsets of Banach spaces. These findings are applicable to problems that are defined by symmetric bilinear forms (or a quadratic strain energy functional). However, certain cases exist where the energy is not coercive, which leads to the imposition of compatibility conditions on the applied forces. Fichera notably tackled the task of minimizing the total potential energy functional.

Panagiotopoulos made significant contributions to the development of discrete models of contact phenomena using variational concepts [5]. He presented a numerical scheme for effectively solving Signorini's problem with friction using stochastic optimization concepts. In the engineering literature, several finite element methods have been proposed for addressing contact problems with friction, including the works of Goodman, Taylor and Brekke, Chan and Tuba, Hardy, Baronet, and Tordion, Ohte, Tsuta and Yamaji, Francavilla and Zienkiewicz, Hughes, Taylor, Sackman, Curnier, and Kanoknukulchai, Fredriksson, Paczelt, Schaeffer, and Herrmann [2]. These authors utilized incremental analyses to efficiently control nonlinearities arising from contact and to model friction effects. Their techniques were based on Lagrange multiplier or Penalty formulations for effectively handling the contact constraint on the displacement field etc. Today, Lagrange multiplier or Penalty formulations are used in nearly all commercial finite element and finite volume software packages [6,7].

Mechanical interface modelling became a primary research area not only in elasticity and machine tool research but also in tribology, continuum mechanics, and applied mathematics[1]. In general, the main challenges regarding mechanical interface modelling as follows,

Problem Definition and Boundary Condition Related:

- To properly model machine tool mechanical interfaces, it is important to consider multiple aspects, including the integration of static, dynamic, and thermal parts of a contacting system into the model. This can result in a complex and nonlinear model that requires careful consideration and analysis.
- Contact problem identification requires selecting suitable mathematical models in contact mechanics with proper boundary conditions for interface behavior predictions.
- To accurately capture the behavior of interfaces in contact, it is often necessary to use a combination of contact models. Simply predicting one variable while keeping other factors constant is often insufficient. This approach fails to consider the complex and mixed boundary conditions that can arise in contact situations. By using a combination of contact models, one can better understand and predict the behavior of interfaces in contact.
- When dealing with boundary conditions, their effects on each other can be quite nonlinear. This can lead to evolving boundary conditions that require entangled loops to capture properly.
- The interaction of different conditions, tribological parameters such as lubricants, wear particles, and scatters due to wear are the other reasons for evolving boundary conditions.

Theoretical Modelling Related:

- The offered theoretical models aren't always able to predict more complicated failure mechanisms such as plastic deformation.
- Furthermore, many of these models are only applicable to a few components with surface stresses.

Solution Algorithm Related:

- The complexity and nonlinearity of the resulting model can be quite high for complete mathematical contact models.
- Even a seemingly simple contact model, without the integration of different aspects, can exhibit significant levels of nonlinearity. Additionally, algorithms designed to solve nonlinear problems can be prone to numerical instability during the solution phase.

1.3. Research Gap

In machine tool research so far, fully analytical methods and contact identification methods like RCSA or equivalent contact representations that avoid direct usage of FE contact algorithms are generally employed [8]. Even a simple modal analysis of a machine tool or another assembly analysis results in more accurate predictions with node sharing/connecting at contact points than directly using FE contact algorithms. However, it has not been extensively explained ‘How the contact algorithms work in FE software?’ and ‘Why are they failing to provide a reliable simulation result?’. Another question is, ‘What are the signs of an unrealistic contact simulation result in an FE simulation result, and How can it be detected from an FE user according to analysis type?’. These questions are crucial; the answer can change according to the analysis type. Let us consider the topology optimization analysis of a machine tool, which is convenient if it can be applied to moving

components, and a deliberately targeted mass reduction can improve the static and dynamic behavior of the machine tool and enhance productivity. The topology optimization methods are based on the homogenization method [9] and topological derivatives [10]. The homogenization method enables the basis for solving the topology optimization problem by allowing the simplest repeating unit of the microstructure to mimic the exact macroscopic behavior of the structure with proper assumptions, which is called the unit cell for FE discretization. Here the critical term is topological derivatives to remove mass from the structure. A topological derivative is a derivative of a shape functional for tiny changes in its topology, such as adding a tiny hole or crack. The binder ingredient of all these terms is strain energy, and transmission of strain energy from one component to another during an assembly-level topology attempt becomes critical to get a reliable result. Strain energy transmission from one component to another via a mechanical interface is another significant concern, especially when a spindle's contact interfaces are considered due to friction-related thermo-mechanical behavior in a machine tool. Thermal analysis in FE is again based on strain rather than stress terms since there is no such thing as 'thermal stress.' Therefore, even simple thermal analysis can give misleading results about the contact areas. However, the reasons behind these misleading results have not been extensively explored, even going further for dynamic analyses.

This study explores the contact-related questions mentioned above, and their effects and significance on machine tool analysis are investigated. A novel mechanical interface modeling framework in FE is presented. The offered method is called RCFM (Reflected Contact Method) and is specially structured for machine tools' topology optimization and thermo-mechanical behavior simulations.

1.4.FE Formulation of Contact Problem

1.4.1. Signorini Contact Problem

The contact models used in current FE software are based on Signorini's contact problem. This contact behavior is expressed as an optimization problem that involves minimizing elastic energy and adhering to the Hertz-Signorini-Moreau (HSM) conditions [2]. These conditions ensure that the bodies in contact cannot penetrate each other. The objective expression, which is the minimization of elastic energy, is a differentiable term. However, the HSM conditions are non-differentiable terms, which makes the contact expression a non-linear optimization problem [2,6]. The non-differentiable part of the contact problem is used to calculate the contact stiffness and contact forces [6].

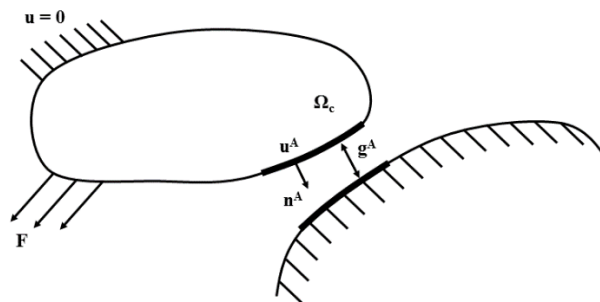


Fig. 1.1 The descriptive monograph of the HSM conditions.

In Fig. 1, the gap element at a specific node is defined as the distance between the contact node and its support in the normal direction. The conditions depicted in Fig. 1 are known as the HSM conditions, which are also referred to as the contact consistency laws. The hitter is assumed to be a linear elastic body, while the foundation is considered rigid. The contact between the foundation and the elastic body is frictionless, as illustrated in Fig. 1. The potential contact surface is represented by a set of potential contact nodes Ω_c , and the normal vector of the contact surface at a specific contact node such as A is denoted \mathbf{n}^A . The gap between the contact node and the support in the normal direction is given by \mathbf{g}_u^A . The kinematic constraint representing the impenetrability of the rigid support can be formulated as in Eq. 1 for node A.

$$\mathbf{g}_u^A - \mathbf{u}^A \mathbf{n}^A \geq 0 \quad (1)$$

$$\mathbf{C}_N \mathbf{u} - \mathbf{g}_u^Y \leq 0 \quad (2)$$

The conditions for all contact nodes can be summarized using Eq. 2, which expresses the kinematic constraint based on the impenetrability of the rigid support (the HSM conditions). In this equation, \mathbf{u} represents the displacement field, and \mathbf{C}_N is the transformation matrix of normal vectors on the potential contact surfaces. The column vector \mathbf{g}_u^Y contains all the gaps. According to this monograph, if the displacement equals the gap, a reaction force \mathbf{R}_N occurs due to contact. However, the reaction force is zero if the displacement is smaller than the gap between the hitter and the foundation. In either case, the multiplication of the reaction force and the kinematic constraint will be zero. These facts are expressed mathematically in Eq. 3, and the set of equations is called the contact consistency laws due to HSM conditions [2].

For all $A \in \Omega_c^2$:

$$\mathbf{C}_N \mathbf{u} - \mathbf{g}_u^Y \leq 0, \quad \mathbf{R}_N \geq 0, \quad \mathbf{R}_N (\mathbf{C}_N \mathbf{u} - \mathbf{g}_u^Y) = 0 \quad (3)$$

It's interesting to note that Eq. 3 can be seen as a continuum problem, and the total potential energy is kept at a minimum at solving such problems. This means that Eq. 3 can be expressed as an optimization problem for the minimum energy [4,2], as stated in Eq. 4.

$$\begin{aligned} \text{Min } \pi(\mathbf{u}) &= \frac{1}{2} \mathbf{u}^T \mathbf{K} \mathbf{u} - \mathbf{F}^T \mathbf{u} \\ \text{st: } \mathbf{C}_N \mathbf{u} &\leq \mathbf{g}_u^Y \\ &: \mathbf{K} \mathbf{u} + \mathbf{C}_N^T \mathbf{R}_N = \mathbf{F} \end{aligned} \quad (4)$$

1.4.2. Implementation to FE Solver

When solving contact problems, computational solution methods are often used. These methods include the Penalty, Lagrange, or Augment Lagrange Method [6,11]. However, some of these methods can impose a penalty term on the strain energy expression of the FE model to satisfy the HSM conditions. Unfortunately, the computational contact models in existing FE

codes are not always sufficient for machine tool designers. These models can be improved in terms of computational cost and prediction accuracy. One problem with computational contact mechanics problems is that they suffer from numerical instability [12,13]. This instability can cause the normal contact pressure and force to exhibit spurious oscillation, which mesh refinement cannot eliminate. In fact, in some cases, mesh refinement can worsen spurious oscillation [13]. To combat this issue, penalty relaxation techniques such as the Penalty Method or the Augmented Lagrange Method can be used. However, relaxing the Penalty values can result in an approximate displacement field in the form of significant interpenetration of contact faces [6,7]. This deviation in the contact displacement field obtained by the Penalty Method can cause inaccurate strain energy transfer between components.

A pure computational expression of the contacted bodies is necessary to achieve a solution in FE solver. This expression should be convenient for the discretization schemes in FE, starting from Signorini's contact consistency rules (HSM) and the weak forms of the governing equations [2,6]. The Penalty Method is frequently used in most of the FE software and structural optimization studies, and it automatically introduces a spring-like term (Eq. 5), referred to as Penalized Contact Stiffness, into the pressure or the force term to satisfy Signorini's contact conditions [6].

$$\mathbf{p}_N = -\epsilon_N \mathbf{g}_N, \epsilon_N > 0 \quad (5)$$

The Penalty Method employs the weak form of total potential energy in an FE solver, with the contact constraint enforcement as its starting point. The weak form of total potential energy comprises two components, the sum of the mechanical work and the contact potential energy because the total potential energy corresponds to a minimum at the solution point for hyper-elastic deflections [6].

The Penalty Algorithm

$$\begin{aligned} \pi_{total}^P &= \pi_{mech} + \pi_{con}^P \rightarrow MIN \\ \delta\pi_{total}^P &= 0 \end{aligned}$$



$$\begin{aligned} \pi_{total}^P &= \pi_{mech} + \frac{\epsilon_N}{2} \mathbf{G}_{con}^P T \mathbf{G}_{con}^P \\ &\rightarrow MIN \\ \delta\pi_{total}^P &= \Delta\pi_{total}^P = 0 \end{aligned}$$

$$\begin{aligned} \text{Nonlinear} \\ \mathbf{G}_{con}^P &= \int_{\Gamma_c} \mathbf{p}_N \delta \mathbf{g}_N dA, \pi_{con}^P = \frac{1}{2} \int_{\Gamma_c} \epsilon_N \mathbf{g}_N^2 dA \end{aligned}$$

To discretize the system linearization
(Δ) is needed

$$\leftarrow \quad (6)$$

As is seen from Eq. 6 [6], the contact potential energy (π_{con}^P) and the weak form of the contact constraint (\mathbf{G}_{con}^P) are non-linear, and their corresponding derivatives are also non-linear. Therefore, linearization is required to discretize the system in FE and to solve the global non-linear equations iteratively. According to minimization of total potential energy, the linearized portion of the potential energy of the contact term should yield zero, as shown in Eq. 7. Eq. 8 represents the linearized version of the contact constraint (Eq.5) [6] at a known displacement(\bar{u}).

$$\left. \begin{aligned} \delta \mathbf{u}^T \mathbf{G}_{con}^P &= 0 & (7) \\ \delta \mathbf{u}^T \mathbf{G}_{con}^P(\bar{\mathbf{u}}) + \delta \mathbf{u}^T \mathbf{K}_T(\bar{\mathbf{u}}) \Delta \mathbf{u} &= 0 & (8) \end{aligned} \right\} \Rightarrow \mathbf{K}_T(u_i) \Delta \mathbf{u}_{i+1} = -\mathbf{G}_{con}^P(u_i) \quad (9)$$

The tangent matrix (\mathbf{K}_T) in Eq. 9 is the crucial element for the Penalty Method. The tangent matrix in the solution algorithm is used as the critical parameter to predict small deformations. The tangent matrix has the same importance for thermo-mechanical contacts. The elastic and thermal deformations are combined using the tangent matrix at the Penalty algorithm in an FE solver.

1.4.3. Contact Force in FE Model

To obtain the reaction force (\mathbf{R}_N) during the solution process of the contact optimization problem, computational methods can be utilized by constraining $\mathbf{C}_N \mathbf{u} - \mathbf{g}_u^y \leq \mathbf{0}$ for the global force equation. However, this process can be quite challenging due to its complexity and the need for high solution accuracy. To address this issue, the Penalty Method is often used in FE software as it requires less computational power and can provide useful estimates for the reaction force. It's important to note that the Penalty Method compensates for any violation of contact consistency laws by increasing the total virtual work and adding an active constraint to the energy equation known as the Penalty Number [2].

For $\epsilon_N > 0$;

$$\pi_p(u) = \frac{1}{2} \mathbf{u}^T \mathbf{K} \mathbf{u} + \frac{1}{2} \mathbf{u}^T \mathbf{C}_N^T \epsilon_N \mathbf{C}_N \mathbf{u} \rightarrow \text{Min} \pi_p(u) = 0 \quad (10)$$

where ϵ_N is the numerically Penalized Contact Stiffness. In Eq. 10, the term $\mathbf{C}_N^T \epsilon_N \mathbf{C}_N$ shows the Penalty Matrix. According to the Penalty Method, the global force equation for the multi-component synthesis of two design domains in normal contact is written as indicated in Eq. 11.

$$\begin{bmatrix} \mathbf{K}^1 + \mathbf{C}_N^T \epsilon_N \mathbf{C}_N & 0 \\ 0 & \mathbf{K}^2 + \mathbf{C}_N^T \epsilon_N \mathbf{C}_N \end{bmatrix} \begin{pmatrix} \mathbf{u}_N^1 \\ \mathbf{u}_N^2 \end{pmatrix} = \begin{pmatrix} \mathbf{f}^1 \\ \mathbf{f}^2 \end{pmatrix} \quad (11)$$

where \mathbf{K}^1 is the stiffness matrix for the first component, \mathbf{K}^2 denotes the stiffness matrix of the second component, and \mathbf{f} stands for the external force vector. This formulation is made compatible with the optimization problem statement for the reaction force (\mathbf{R}_N) during contact as follows:

$$\mathbf{R}_N = (\mathbf{C}_N^T \epsilon_N \mathbf{C}_N) \mathbf{u}_N \quad (12)$$

Eq. 12 is a piece of firm evidence that the condition of the stiffness matrix depends on the Penalized Contact Stiffness value found by the FE software, which can be unreliable under many circumstances.

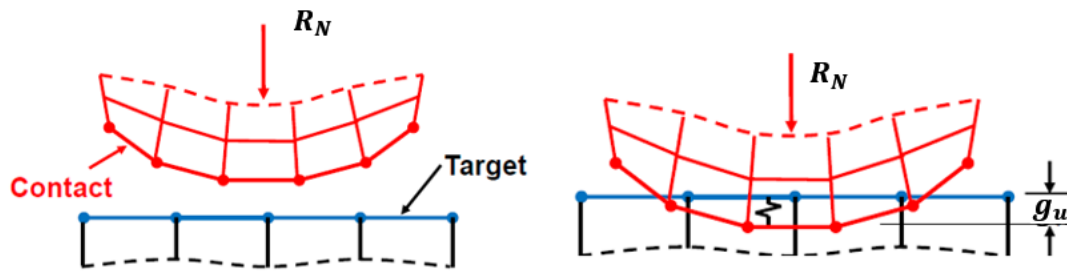


Fig. 1.2 The penalized contact stiffness monograph.

In Fig.2, it is shown that using very small Penalty Numbers can lead to material penetration, while using very high Penalty Numbers can approach the correct solution to meet the HSM conditions. However, the solution procedure of this method relies on Newton-Raphson iterations, which do not guarantee convergence. In fact, the solution procedure can suffer from jumps between two values in consecutive iterations, leading to spurious oscillations in the contact force and pressure profiles [7]. This issue is particularly prevalent when displacement boundary conditions are employed [13]. Fig. 3 illustrates this situation, where two half cubes are pressed against each other via a 0.1m displacement from the top, while the bottom of the cube assembly is fixed. The simulations employ 1000 hexahedral elements with 5302 nodes, and the contact pressure and force profiles are obtained using the Lagrange and Penalty methods. ANSYS serves as the contact formulation solver, and node-to-node and node-to-surface formulations are employed for the contact discretization. The results of the analyses are similar, as the cube example uses hexahedral meshes. Finally, Optistruct is employed as a solver for the topology optimization of the cubes, using a Penalized Contact Stiffness (ϵ_N) magnitude of 10^{16} N/m [13].

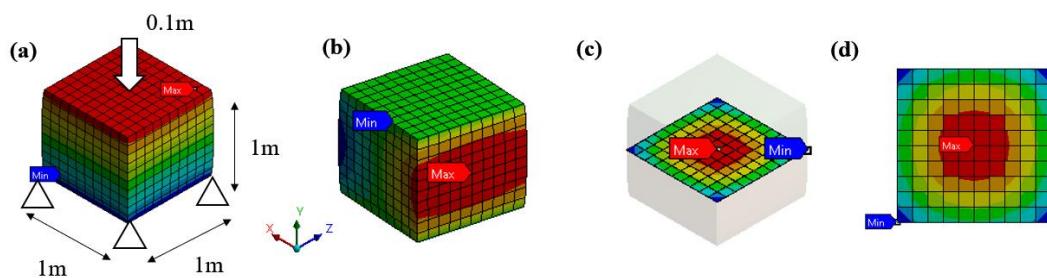


Fig. 1.3 The contact of half cubes: a) The loading conditions and total deformation, b) Deformation at X axis, c) Contact surface, d) Oscillated contact pressure.

As shown in Fig. 4, the contact forces obtained from the sectional view of Fig. 3d are depicted. The stable analytic solution of this punch problem is indicated by a red line, which is based on

Galin's study [14]. The blue line illustrates the contact force profile obtained using the Lagrange method, while the black line represents the contact force profile obtained through the Penalty method.

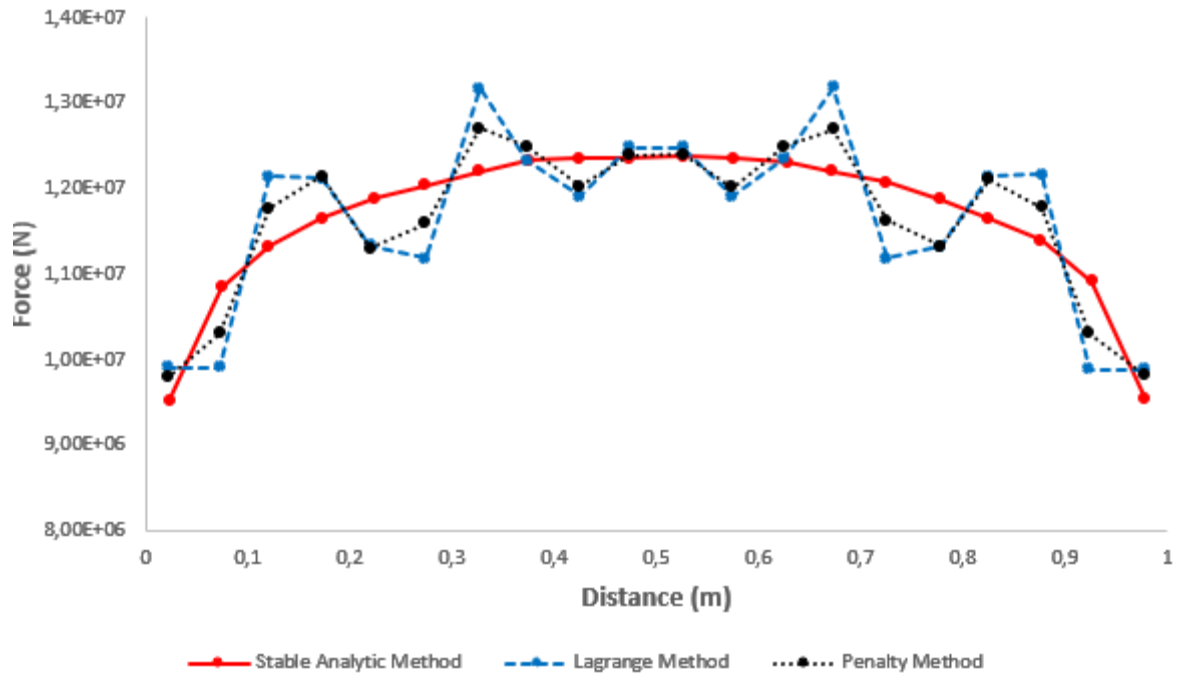


Fig. 1.4 Contact force variations for different computational methods in FE.

As Fig. 4 illustrates, the Lagrange Method allows for more observation of the size and frequency of oscillations, with HSM conditions being precisely imposed. In a previous study [13], constant strain triangle elements showed similar results, highlighting the negative effects of non-conforming meshes and mesh refinement on contact profiles, both frictionless and frictional.

1.5.FE Formulation of Thermo-mechanical Contact Problem

Eq. 13 [2,6] outlines the thermo-mechanical contact conditions according to Signorini problem. These conditions remain largely unchanged for thermo-mechanical cases, with added terms to account for contact pressure. The thermal field undergoes a time-dependent partial equation, resulting in a historical element (H^Y) and a compact structural element (Z^Y) that relies on various factors such as the configuration of the contacted bodies, material velocity, and temperature.

$$g_N \geq 0, \quad p_N(Z^Y, H^Y) \leq 0, \quad g_N p_N(Z^Y, H^Y) = 0 \quad (13)$$

First, the tangent matrix in FE for thermo-mechanical contacts will be explained in this section. Deformation and temperature work together in a mechanical system. Thus, the total deformation comprises elastic and thermal elements, which require separation for FE calculations. The separation of the displacement deformation gradient field is expressed in Eq. 14. Similarly, the gap function between the bodies in contact can be separated into its thermal (θ) and elastic (e) components, as stated in Eq. 15. The separated gap functions are in Eqs. 16 and 17 [6].

$$\mathbf{F} = \mathbf{F}_e \mathbf{F}_\theta \quad (14) \quad g_{NIE} = x_{NI}^2 - x_{NI}^1 \quad (16) \quad \rightarrow \delta g_{NIE} = f(\eta_{NI}^Y) \quad (18)$$

$$g_{NI} = g_{NIE} g_{NI\theta} \quad (15) \quad g_{NI\theta} = \theta_{NI}^2 - \theta_{NI}^1 \quad (17) \quad \rightarrow \delta g_{NI\theta} = f(\vartheta_{NI}^Y) \quad (19)$$

where Eq. 16 represents the geometrical gap function at the normal contact direction (N) at the node (I), and Eq. 17 corresponds to the temperature difference between the contact interfaces. Eqs 18 and 19 yield the variations of thermal and elastic parts of the gap function. Eq. 20 yields the relation between the weak form and the discretized version of the contact constraints. [6,7].

$$\left. \begin{aligned} \mathbf{G}_{(con)e}^P &= \int_{\Gamma_c} p_N \delta g_{Ne} dA & \sum_{I=1}^{n_c} p_{NI} \delta g_{NIE} A_I & \sum_{I=1}^{n_c} \epsilon_N(g_{NIE}) \eta_{NI}^T \mathbf{C}_I A_I \\ \mathbf{G}_{(con)\theta}^P &= \int_{\Gamma_c} q_N \delta g_{N\theta} dA & \sum_{I=1}^{n_c} q_{NI} \delta g_{NI\theta} A_I & \sum_{I=1}^{n_c} q_{NI} \vartheta_{NI}^T \mathbf{C}_I A_I \end{aligned} \right\} \begin{aligned} & \sum_{I=1}^{n_c} \eta_{NI}^T [\mathbf{K}_{Te}] \Delta \mathbf{u} \\ & \sum_{I=1}^{n_c} \vartheta_{NI}^T [\mathbf{K}_{T\theta}] \Delta \theta \end{aligned} \quad (20)$$

The thermo-mechanical contact expression in the coupled form can be obtained from Eq.20, which leads to Eq. 21. The tangent matrix of the thermo-mechanical contact for the Penalty Method is represented by Eq. 22. It is important to mention that for computational thermal calculations, only conduction conditions are considered, and no gas is assumed to be present in the environment.

$$\mathbf{G}_{(con)}^P = \langle \eta_{NI}^T, \vartheta_{NI}^T \rangle [\mathbf{K}_T] \begin{pmatrix} \Delta \mathbf{u} \\ \Delta \theta \end{pmatrix} \quad (21) \quad \mathbf{K}_T = \begin{bmatrix} \frac{\delta \epsilon_N}{\delta g_N} \mathbf{C}_I \mathbf{C}_I^T & \mathbf{0} \\ \frac{\delta q_N}{\delta g_N} \mathbf{C}_I \mathbf{C}_I^T & h_c \mathbf{C}_I \mathbf{C}_I^T \end{bmatrix} \mathbf{A}_I = \begin{bmatrix} \text{elastic term} & \mathbf{0} \\ \text{coupling term} & \text{thermal term} \end{bmatrix} \quad (22)$$

1.6.FE Contact Algorithms and Effects on Topology Optimization

1.6.1. FE Contact Algorithms and Strain Energy Transmission

When it comes to topology optimization algorithms, the strain energy deviation at the contact area is crucial. The Lagrange Method is often considered a good option for contact constraint problems, as it strictly imposes the HSM conditions and reflects actual contact behavior. However, it can create rigid body motion and pressure and force oscillations, making it questionable for a topology optimization problem [15]. While the Nietzsche and Mortar methods have been proposed as alternatives, their reliability is not fully proven, and their implementation is complicated [16,17]. As a result, most industrial FE software packages (Ansys, HyperWorks, COMSOL, and Abaqus) use the Penalty Method, despite its limitations. Accurately reflecting force transmission and strain energy is important for reliable solutions in structural analyses and machine tool topology optimization.

When it comes to contact-coupled topology optimization, the Penalty Method is widely used in FE software to reduce computational complexity and load. This method introduces a spring-like term (Eq.5) into the pressure or force term to meet Signorini's contact conditions. However, very high penalty numbers can lead to an ill-conditioned problem and jumps in consecutive iterations during the solution procedure. To avoid this issue, a smaller penalty number must be selected, which can result in a deviated displacement field and strain energy deviation at contact areas. This deviation can significantly affect the topology optimization results, as the optimization algorithm takes the strain energy as the base [18,19]. Inaccurate strain energy

transfer between components can also affect the prediction of thermo-mechanical deformation in FE tools, leading to misleading topology optimization results for machine tools. Therefore, it is crucial to carefully select the penalty number to obtain accurate results in contact-coupled topology optimization.

The strain energy deviation is exemplified in Fig. 5. In the figure, the strain energy distributions are illustrated for the uniaxial compression. The beam illustration with spring elements (middle) is based on the analytic and experimental solution of the contact problem [14]. At the same time, the right one shows the solution obtained from the Penalty Method in an FE solver. The strain energy results indicate that the Penalty Method represents strain values 30% less than in reality near the contact area. This deviation will affect the topology optimization results. The beams at the left for both figures represent models without a connection to ensure that the springs work accurately for topology optimization.

Similarly, deviated deformation gradients and strain energy values cause higher contact stiffness values in FE models for machine tool applications due to the Penalty Method. This stiffness deviation is very critical for machine tools since the entire stiffness of a machine tool system depends on the least stiff components, which include many contact regions such as bearings, ball screws, and linear guides. Thus, the higher contact stiffness than the actual value results in inaccurate strain energy transfer between the components that affect the prediction of thermo-mechanical deformation in FE tools. This situation causes misleading topology optimization results for machine tools.

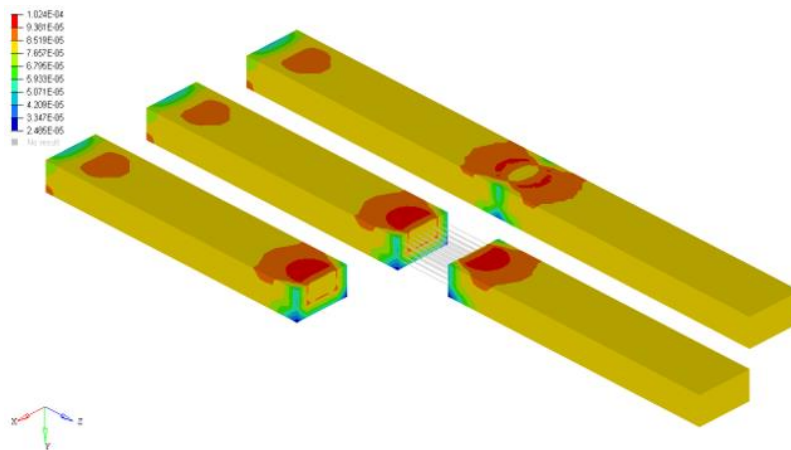


Fig. 1.5 The strain energy profiles for the contacted beams.

1.6.2. Topology Optimization Problem Statement

The primary objective should be to minimize the entire structure's compliance by limiting the total mass to obtain a lightweight but stiff structure. Additionally, the directional stiffness behavior of the machine tool should be controlled by employing displacement constraints on the spindle tip [20]. The topology optimization problem statement is written in Table 1 using the SIMP algorithm according to these needs. The problem statement is based on the HSM contact consistency laws assuming frictionless bilateral contact.

Table 1. Contact-coupled Optimization Problem Statement by Employing the Penalty Method

Table 1.1 Contact-coupled Optimization Problem Statement by Employing the Penalty Method

Statement for Pure Computational Method
$\min_{\rho, u}: \varphi(\rho) = \mathbf{F}^T \mathbf{u}$
$st : \min \pi(u) = \frac{1}{2} \mathbf{u}^T \mathbf{K}(\rho) \mathbf{u} - \mathbf{F}^T \mathbf{u}$
$: \mathbf{C}_N \mathbf{u} \leq \mathbf{g}_w^\gamma, \gamma = 1, \dots, \Omega$
$: V(\rho) = \sum_{e=1}^N v_e \rho_e = v^T \rho \leq V^*, e = 1, \dots, N$
$: \mathbf{g}_u(\rho) \leq \mathbf{g}_w^i, i = 1, \dots, M$
$: 0 \leq \rho_{min} \leq \rho \leq 1$
$: \mathbf{K}(\rho) \mathbf{u} + \mathbf{C}_N^T \mathbf{R}_N = \mathbf{F}$

In Table 1, φ denotes the compliance; ρ is the artificial density for the SIMP algorithm; \mathbf{K} is the stiffness matrix; \mathbf{F} is the force field; \mathbf{R}_N is the reaction force due to contact; V is the total volume; v_e is the elemental volume; v is the elemental density; V^* is the initial volume; and \mathbf{g}_w^i is the displacement limitation on the spindle tooltip. In computational contact mechanics, the contact problem is formulated as an optimization problem that aims to minimize the potential energy (π).

1.6.3. Example Application

In the cube assembly shown in Fig. 3, the bottom part has been optimized in accordance with the problem formulation given in Table 1. This was achieved by utilizing both the Penalty Method and the Lagrange Method for the contact interfaces. The resulting topologies can be seen in Fig.6, after a 30% volume reduction and a 0.1m downward displacement constraint for each contact method. It is worth noting that the topology in Fig. 6a was obtained using the Penalty Method, while the other topology was produced using the Lagrange Method within the problem formulation.

The crevice-like patterns on the contact interfaces resulting from the oscillated contact profiles are shown in Fig. 4, and they depend on the employed contact method. As the Lagrange Method results in more pronounced oscillations on the contact force profile, the depth and width of the crevice-like patterns resulting from the Lagrange Method are more significant than those resulting from the Penalty Method. Although the appropriate penalty parameter was selected for this example, the contact force oscillations could not be avoided due to the numerical nature of the contact algorithms. However, a stable contact force profile will not lead to the occurrence of crevice-like patterns during the structural optimization since the oscillated contact forces result in locally stiffer or weaker structural behavior on some parts of the contact interface for both Penalty and Lagrange methods.

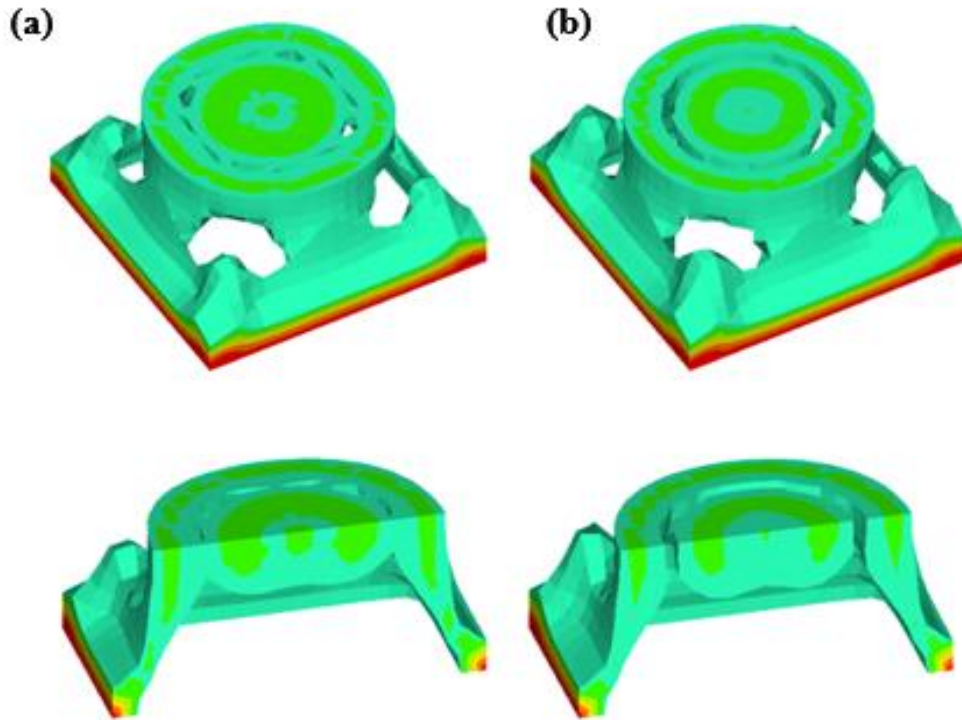


Fig. 1.6 Topology optimization results of the bottom part of the cube assembly with complete and sectional views: a) the Penalty Method; b) the Lagrange Method.

1.7.The Proposed Novel Contact Solutions

1.7.1. RCFM Method

This study introduces the Reflected Contact Force Method (RCFM), a nodal force distribution method based on a contact stiffness function in an FE model to simulate the contact behavior at the contact area, which can be obtained from empirical data or a contact model, for the topology optimization application of machine tools. To obtain a stable contact stiffness function, the contact behavior is mapped to nodal spring elements in the FE model by imposing the non-linear behavior of contacts to the spring stiffness for structural optimization. Fig. 6 indicates the flow chart of the RCFM method. The mapped contact forces are renewed for each iteration of the optimization, and the contact compliance is limited beforehand by using the predefined contact behavior. In this method, possible contact areas of the components are assumed to be in contact during the optimization stage. In contrast to the RCFM method, HSM contact conditions in PCMs define zero contact forces while seeking the contact phenomena between the components. Problematically, zero contact forces in PCMs cause sensitivity values of zero in the SIMP algorithm, which might result in failure of the SIMP algorithm during the optimization process [21]. Hence, to represent realistic contact behavior, zero contact forces are eliminated during the optimization process while applying the RCFM and SIMP algorithm for machine tools.

This study proposes a new method called the Reflected Contact Force Method (RCFM) that utilizes a nodal force distribution technique based on a contact stiffness function in an FE model. This method is used to simulate the contact behavior at the contact area for topology

optimization applications of machine tools. The contact stiffness function is obtained either from empirical data or a contact model. To ensure stability, contact behavior is mapped to nodal spring elements in the FE model, and the non-linear behavior of contacts is imposed on the spring stiffness for structural optimization. The flow chart of the RCFM method is depicted in Fig. 7, where the contact forces are updated at each iteration of the optimization, and contact compliance is limited beforehand by using the predefined contact behavior. During the optimization process, the RCFM and SIMP algorithm are applied for machine tools to represent realistic contact behavior. In comparison to the HSM contact conditions in FE software algorithms, which define zero contact forces while seeking contact phenomena between components, the zero contact forces are eliminated during the optimization process while applying the RCFM and SIMP algorithm for machine tools. This is because zero contact forces in FE software algorithms cause sensitivity values of zero in the SIMP algorithm, which could lead to the failure of the SIMP algorithm during optimization.

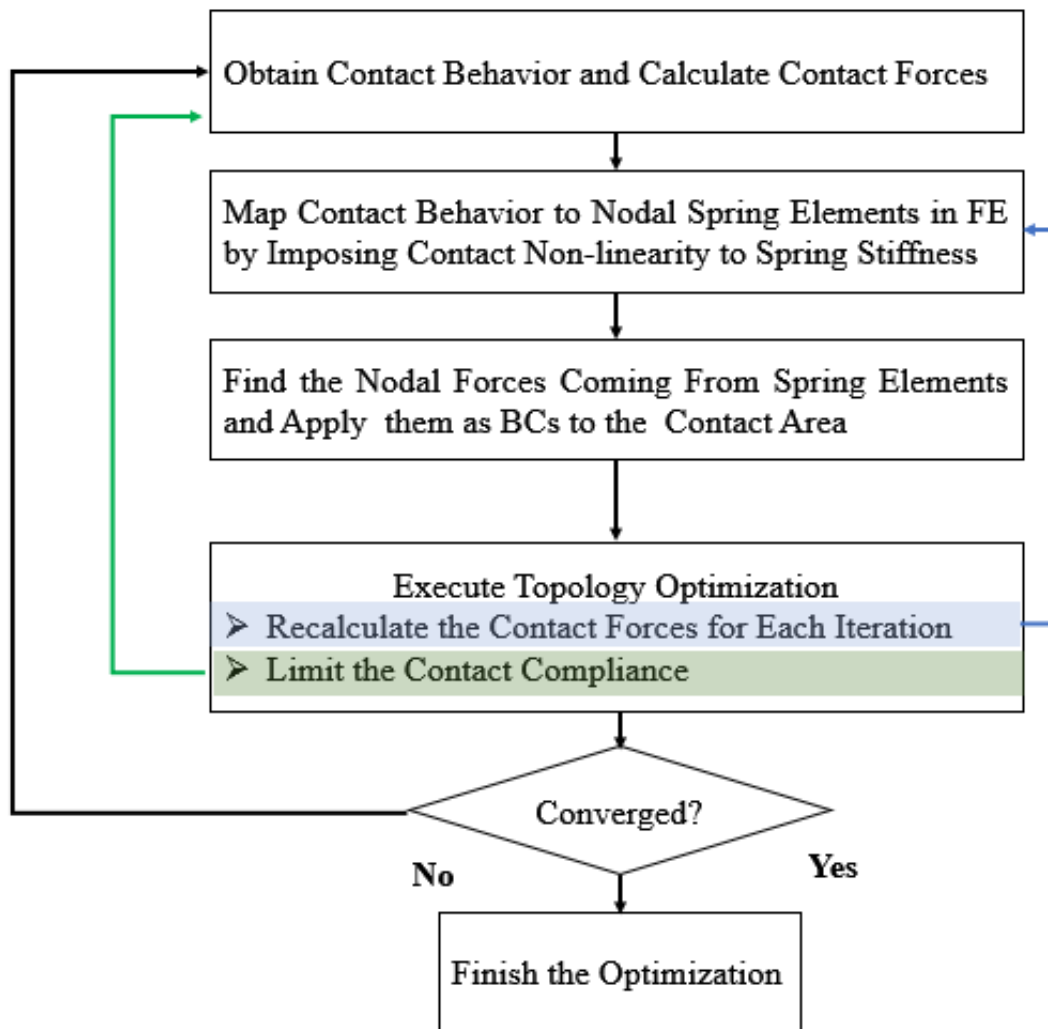


Fig. 1.7 Hybrid Framework of the Reflected Contact Force Method (RCFM).

1.7.2. The RCFM Formulation of Contact Problem

Based on the research, it appears that the contact profiles in machine tools structures have symmetric properties. According to the general constitutive contact force equation (Eq. 23), this applies specifically to symmetric contact profiles [6,7]. It's noteworthy that Eq. 23 can be determined using the Hertz Contact Theory, empirical data from experiments, or the Penalty Method from computational contact mechanics.

$$\mathbf{R}_N = \mathbf{C}(\mathbf{g}_N)^m, \text{ where } \mathbf{g}_N \rightarrow \mathbf{u}_{tr} \text{ if } \mathbf{R}_N > \mathbf{0} \quad (23)$$

C describes the contact stiffness, and m is a coefficient from the chosen contact calculation method. For instance, m yields 1 for the Penalty Method, while it is taken as between 2 and 3.3 for steel-to-steel contact in Hertz Contact Theory [6, 22]. The term in Eq. 23 stands for the gap between the contacting bodies, and in the case of active contact, it must be equal to the translational displacement (\mathbf{u}_{tr}) between the contacting bodies. In RCFM, the contact behavior, which must be transformed to the form given in Eq. 23, is mapped onto spring elements for the topology optimization of machine tools in the FE model using Eq. 24.

$$\mathbf{R}_N = \mathbf{K}_{tr}^s \mathbf{u}_{tr} \quad (24)$$

where \mathbf{K}_{tr}^s is the mapped spring (contact) stiffness and \mathbf{u}_{tr} is the displacement in the translational direction. In this method, the predefined contact forces are only considered in the translational direction because computational methods matter only in normal directions in the FE model [23].

Contact Force in the RCFM

According to the RCFM, the global force equation for the multicomponent synthesis of two design domains in normal contact can be written as follows:

$$\begin{bmatrix} \mathbf{K}^1 + \mathbf{K}_{tr}^s & 0 \\ 0 & \mathbf{K}^2 + \mathbf{K}_{tr}^s \end{bmatrix} \begin{pmatrix} \mathbf{u}_{tr}^1 \\ \mathbf{u}_{tr}^2 \end{pmatrix} = \begin{pmatrix} \mathbf{f}^1 \\ \mathbf{f}^2 \end{pmatrix} \quad (25)$$

where \mathbf{K}^1 is the stiffness matrix for the first component, \mathbf{K}^2 denotes the stiffness matrix of the second component and \mathbf{f} stands for the external force vector. The contacts in this study are represented via spring elements according to contact profiles in the FE model. Then, the measured contact stiffness is reconciled with spring stiffness in the FE model. This new formulation is made compatible with the restated optimization problem for the reaction force (\mathbf{R}_N) during contact. The details extended details of the RCFM can be found in [24].

1.8. Thermo-Mechanical RCFM Method

According to Eq. 20, it is possible to derive the thermo-mechanical contact expression in the coupled form, which leads to Eq. 26. Afterwards, Eq. 27 provides the tangent matrix of the thermo-mechanical contact for the Penalty Method. It is important to mention that computational thermal calculations only consider conduction conditions, as no gas is assumed in the environment.

$$\mathbf{G}_{(con)}^P = \langle \boldsymbol{\eta}_{NI}^T, \boldsymbol{\vartheta}_{NI}^T \rangle [\mathbf{K}_T] (\Delta \mathbf{u}) \quad (26)$$

$$\mathbf{K}_T = \begin{bmatrix} \frac{\delta \epsilon_N}{\delta g_N} \mathbf{C}_I \mathbf{C}_I^T & \mathbf{0} \\ \frac{\delta q_N}{\delta g_N} \mathbf{C}_I \mathbf{C}_I^T & h_c \mathbf{C}_I \mathbf{C}_I^T \end{bmatrix} \mathbf{A}_I = \begin{bmatrix} \text{elastic term} & 0 \\ \text{coupling term} & \text{thermal term} \end{bmatrix} \quad (27)$$

After analyzing the problem, we found that the coupling term varies depending on the contact pressure (as shown in Table 2). However, if the contact pressure remains constant, the coupling term disappears. To address this issue, we implemented a hierarchical analysis scheme where the mechanical part is solved first, followed by the thermal part. Our proposed method involves using substitutions derived from experiments to allow FE solvers to use the same tangent matrix. This eliminates the need for contact enforcements (ϵ_N and q_N) resulting from Signorini's formulation in cases of active contact. During active contact, the gap function reaches its limit, which can be modified using (u_N). Additionally, we replaced the elastic (ϵ_N) and coupling (q_N) term with experimental data (as shown in Table 2) using our proposed method.

Table 1.2 The Tangent Matrix Data Transition from Computational to Experimental Method

Data Transition For Active Contact ($g_N \leftrightarrow u_N$)	Computational Contact Data	Experimental Contact Data	Corresponding FE Element and Matrix
$\frac{\delta \epsilon_N}{\delta g_N} \rightarrow (\epsilon_N \leftrightarrow k_{exp}) \rightarrow \frac{\delta k_{exp}}{\delta u_N}$	$\mathbf{p}_N = \epsilon_N \mathbf{g}_N$	$H = \mathbf{R}_N / \mathbf{u}_N^{3/2}$ $\mathbf{K}_{exp}^{se} = H \mathbf{u}_N^{1/2}$	Spring Element [\mathbf{K}_{exp}^{se}]
$\frac{\delta q_N}{\delta g_N} \rightarrow (q_N \leftrightarrow q_{bearing}) \rightarrow \frac{\delta q_{bearing}}{\delta u_N}$	$\mathbf{q}_N = h_c(\mathbf{p}_N) \Delta \boldsymbol{\theta}^V$ $h_c = h_{spot}(\mathbf{p}_N) + h_{gas} + h_{rad}$	$Q_{bearing} = W_\theta$ $W_\theta = \mathbf{F}_{w\theta} \mathbf{u}_{exp}$ $\mathbf{q}_{bearing} = \mathbf{K}_{exp}^{G\theta} (\Delta \boldsymbol{\theta}^V)$	Virtual Thermal Gap Element [$\mathbf{K}_{exp}^{G\theta}$]

The tangent matrix yields Eq. 28 after imposing the data from experiments. The experimental data transition affects the elastic and coupling term of the tangent matrix.

$$\mathbf{K}_T(\text{new}) = \begin{bmatrix} \frac{\delta \mathbf{K}_{exp}^{se}}{\delta u_N} \mathbf{C}_I \mathbf{C}_I^T & \mathbf{0} \\ \frac{\delta \mathbf{q}_{bearing}}{\delta u_N} \mathbf{C}_I \mathbf{C}_I^T & \mathbf{K}_{exp}^{G\theta} \mathbf{C}_I \mathbf{C}_I^T \end{bmatrix} \mathbf{A}_I \quad (28)$$

1.9. The Contact Representation and Experimental Identification of Contact Parameters

When it comes to machine tools, predicting the contact elements and their contact profiles is a straightforward process. These elements can take the form of cylinders or spheres with a rigid foundation or half cylinders on foundations. To obtain a reliable contact solution for these predictable contacts with homogenous profiles, the Hertz Contact Theory is employed. This theory, along with contact experiments, is used to calculate contact stiffness instead of the proposed method. Once the actual contact stiffness has been determined, a new contact representation method is suggested using springs in FE. Fig. 8 shows the substituted FE elements, which replace the built-in contact elements in the FE libraries. The springs represent

contact stiffness, while the gap elements represent heat conduction between the parts. To map the experimental and FE stiffness, a conformal stiffness mapping method has been proposed, which can be found in [24].

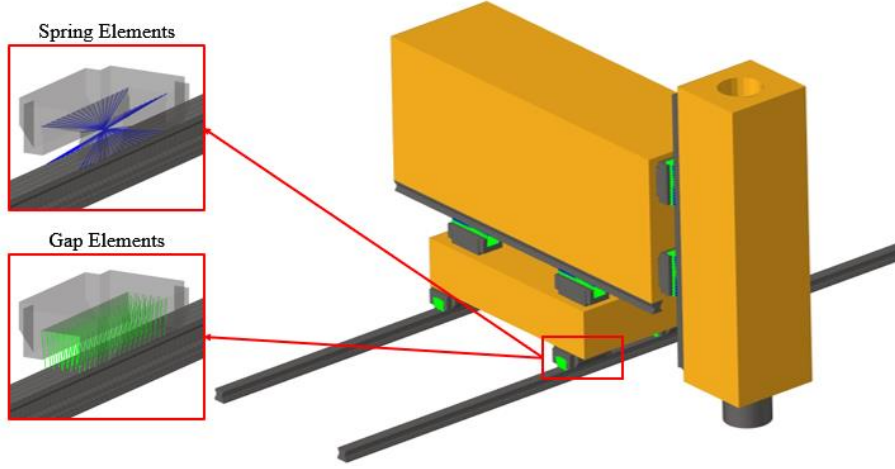


Fig. 1.8 The proposed virtual representation of the thermo-mechanical contact in FE environment

To accurately calculate the conduction matrix ($K_{exp}^{G\theta}$), it's important to first determine the heat production of the spindle bearings. Eq.29 [25] describes the heat produced by these bearings, and to calculate the heat flux data ($q_{bearing}$), the bearing areas in the spindle are used. In order to establish the contact conduction matrix and understand the relationship between the contact conduction coefficient and contact pressure data (as shown in $h_{spot}(p_n) = h_{so} \left(\frac{p_n}{H_V} \right)^w$), it's necessary to gather thermal work and displacement data from experiments.

$$\begin{aligned}
 Q_{bearing} &= P_{bearing}t \\
 P_{bearing} &= P_{load} + P_{visc} \\
 \left. \begin{aligned}
 &P_{load} \\
 &= (1,047 \times 10^{-4})nM_{load} \\
 &M_{load} = F_a f_{load} d_{avg}
 \end{aligned} \right\}
 \end{aligned}
 \quad
 \begin{aligned}
 P_{visc} &= (1,047 \times 10^{-4})nM_{visc} \\
 M_{visc} &= f_{visc}(v_0 n)^{\frac{2}{3}} d_{avg}^3 10^{-7}, v_0 n \geq 2000 \\
 M_{visc} &= f_{visc} 160 \times 10^{-7} d_{avg}^3, v_0 n \leq 2000
 \end{aligned}
 \tag{29}$$

Experimental results are required to obtain contact stiffness and the conduction coefficient for the tangent matrix in the FE solvers. Therefore, contact experiments for critical components-bearings and linear guides were designed to identify contact stiffness [26]. Fig. 9 represents the proposed contact model's experimental results and FE representation. Fig. 9(a) illustrates the force-deflection curve derived from the experimental results. Fig. 9(b) indicates the thermal work-deflection relation for spindle bearings. The thermal work done by spindle bearings was obtained by conducting different experiments. First, heat generated by spindle bearings was determined [27]. Then, laser sensors measured the deflection change over time due to heat generated by the spindles [27]. The thermal work-deflection curve was derived from the combination of these two experiments. After calculating the heat flux, a thermal work-

deflection curve was employed to determine the contact conduction coefficient and contact pressure relation.

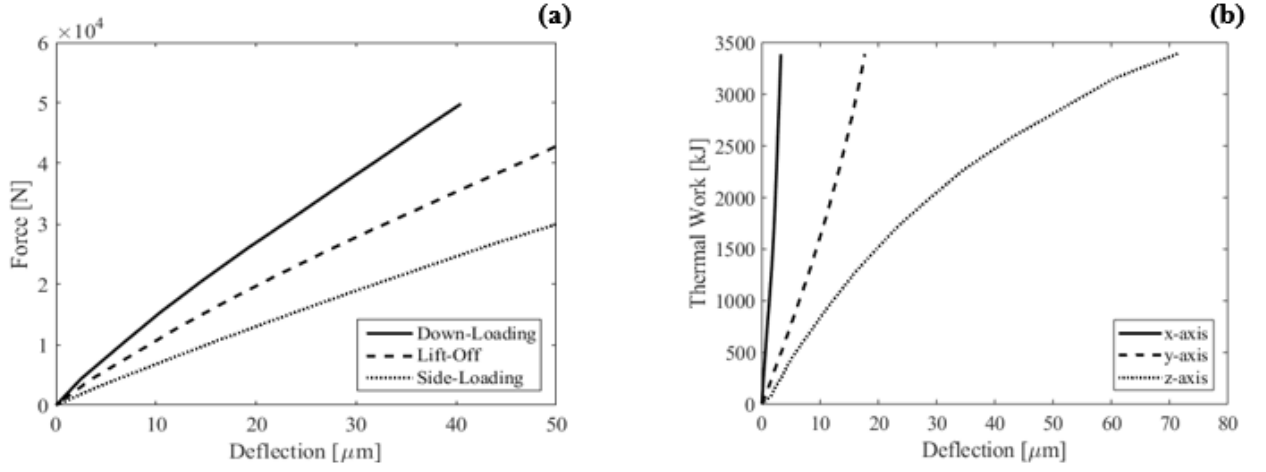


Fig. 1.9 (a) Experimental force-deflection graph (b) Experimental thermal work-deflection

1.10. Topology Optimization and Contact Implementation of RCFM

1.10.1. Topology Optimization with RCFM

The problem statement given in Table 1 is restated according to the proposed method in Table 3 by aiming at the same objectives and employing the SIMP algorithm.

Table 1.3 Contact-coupled Optimization Problem Statement by employing the RCFM.

Statement for the RCFM
$\min_{\rho, u}: \varphi(\rho) = \mathbf{F}^T \mathbf{u}$
$\text{st} : \varphi_c(u_{tr}) = \mathbf{R}_N^T \mathbf{u}_{tr} \leq \varphi_c^*$
$: \mathbf{u}_{tr} \leq \mathbf{g}_w^\gamma, \gamma = 1, \dots, \Omega$
$: V(\rho) = \sum_{e=1}^N v_e \rho_e = \mathbf{v}^T \boldsymbol{\rho} \leq V^*, e = 1, \dots, N$
$: \mathbf{g}_u(\rho) \leq \mathbf{g}_u^i, i = 1, \dots, M$
$: 0 \leq \rho_{min} \leq \rho \leq 1$
$: \mathbf{K}(\rho) \mathbf{u} + \mathbf{K}_{tr}^s \mathbf{u}_{tr} = \mathbf{F}$

Here φ_c stands for the translational compliance at the contact areas in the FE model; φ_c^* denotes the experimentally defined contact compliance; \mathbf{R}_N denotes the normal contact force in the

translational direction of the contact elements; u_{tr} indicates the experimentally identified normal translational displacement between the hitter and its foundation; and K_{tr}^s stands for the predefined translational spring stiffness between the contacting components. Ertürk et al. [23] showed that torsional stiffness was negligible for machine tool stiffness in contact-intense subassemblies such as bearing contacts or linear guides.

Fig. 10 provides a visual representation of the topology optimization results of the Penalty and Lagrange Methods and the RCFM, which were demonstrated in the cube example. The Penalty and Lagrange Methods shown in Fig. 10a and 10b, respectively, represent the contact interfaces. On the other hand, the RCFM in Fig. 10c maps the contact forces smoothly to the contact interface.

In FE models, oscillated contact force profiles and deviated strain energy values can cause locally higher or lower contact stiffness at certain points of the contact interface. This is due to the unstable nature of the Penalty and Lagrange Methods, which can cause different crevice-like patterns on the contact interfaces for cube examples. However, the smooth and realistic prediction of the contact behavior resulted in a different topology for this cube example.

This stiffness deviation is critical for machine tools since the entire stiffness of a machine tool system depends on the least stiff component, which includes many contact regions such as bearings, ball screws, and linear guides. Thus, the higher or lower contact stiffness than the actual value results in inaccurate strain energy transfer between the components that affect the topology optimization results. The RCFM solves this problem during the topology optimization of machine tool structures.

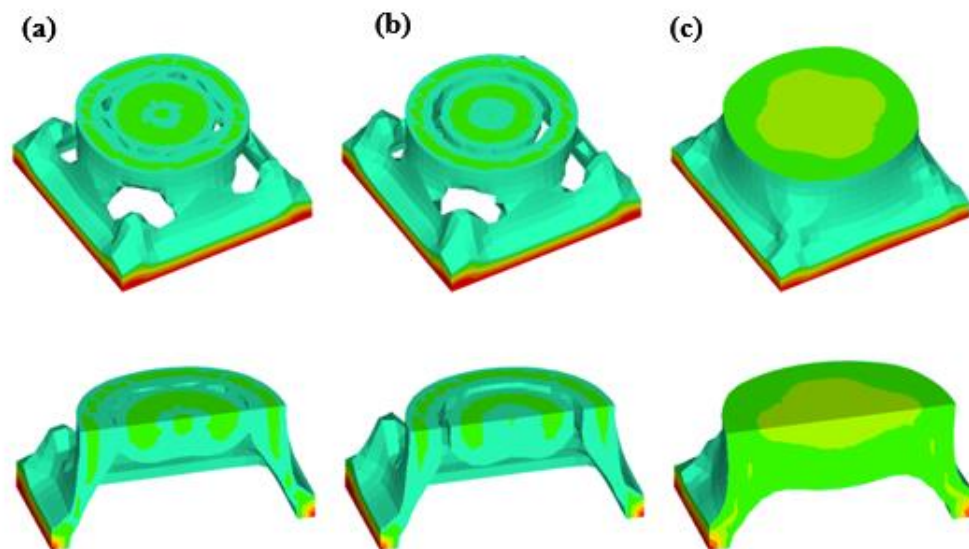


Fig. 1.10 Topology optimization results of the bottom part of the cube assembly with complete and sectional views a) the Penalty Method b) the Lagrange Method c) Reflected Contact Force Method.

1.10.2. Topology Optimization with Thermo-mechanical RCFM

Machine tools have complex assemblies and contain connections among their components in which strain energy is transferred from one component to another via contacts. These contacts occur intensively between the least stiff components of a machine tool-linear guides, and bearings-which can dominate the entire stiffness of a machine tool. Hence, the optimization problem statement for machine tool assemblies must include contact conditions to avoid misleading results. The primary objective should be minimizing the compliance of the entire structure by limiting the total mass to obtain a lightweight but stiff structure. Additionally, the directional stiffness behavior of the machine tool should be secured by employing displacement constraints on the spindle tip [26]. According to these needs, the topology optimization problem is stated in Table 4, where (a) states the minimum static compliance problem by employing the proposed thermo-mechanical model, and (b) states the same problem for the minimum thermal compliance objective. These formulations define the topology optimization problems for the minimum static and thermal compliance objectives for machine tool design by employing the proposed thermo-mechanical contact method (Line 1 in Table 4). The optimization problems are treated with thermo-mechanical contact (Lines 2 and 3 in Table 4), axial stiffness (Line 5 in Table 4), and volume constraints (Line 4 in Table 4) for machine tool design. The loading conditions combine the cutting scenario and heat produced by spindle bearings (Lines 6 and 7 in Table 4).

Table 1.4 Problem Statements with Thermo-Mechanical Contact Constraints for Static and Thermal Compliance

(a) Static Compliance Problem	(b) Thermal Compliance Problem
$\min: \varphi_s = \mathbf{F}^T \mathbf{u}_a$	$\min: \varphi_T = \mathbf{C}$
$st: \min \pi_c(u) = \frac{1}{2} \mathbf{u}_a^T \mathbf{K} \mathbf{u}_a - \mathbf{F}^T \mathbf{u}_a$	$st: \min \pi_c(u) = \frac{1}{2} \mathbf{u}_a^T \mathbf{K} \mathbf{u}_a - \mathbf{F}^T \mathbf{u}_a$
$: \mathbf{u}_N \leq \mathbf{g}_N^\gamma, \gamma = 1, \dots, \Omega$	$: \mathbf{u}_N \leq \mathbf{g}_N^\gamma, \gamma = 1, \dots, \Omega$
$: V \leq V^*$	$: V \leq V^*$
$: \mathbf{g}_u \leq \mathbf{g}_u^i, i = 1, \dots, M$	$: \mathbf{g}_u \leq \mathbf{g}_u^i, i = 1, \dots, M$
$: \mathbf{K}_{Mat} \begin{bmatrix} \mathbf{u}_a \\ \boldsymbol{\theta} \end{bmatrix} + \mathbf{K}_{T(new)} \begin{bmatrix} \Delta \mathbf{u}_n \\ \Delta \boldsymbol{\theta}^\gamma \end{bmatrix} = \begin{bmatrix} \mathbf{F}_s + \mathbf{F}_t \\ \mathbf{Q} \end{bmatrix}$	$: \mathbf{K}_{Mat} \begin{bmatrix} \mathbf{u}_a \\ \boldsymbol{\theta} \end{bmatrix} + \mathbf{K}_{T(new)} \begin{bmatrix} \Delta \mathbf{u}_n \\ \Delta \boldsymbol{\theta}^\gamma \end{bmatrix} = \begin{bmatrix} \mathbf{F}_s + \mathbf{F}_t \\ \mathbf{Q} \end{bmatrix}$
$: \mathbf{F}_s + \mathbf{F}_t = \mathbf{F}$	$: \mathbf{F}_s + \mathbf{F}_t = \mathbf{F}$
	$: \mathbf{C} = \int \nabla \boldsymbol{\theta} \cdot \mathbf{q} dA$

1.11. Machine Tool Application

In this study, the design domain is determined as moving structural components of a CNC system, which includes spindle-holder, ram and sliding table. Linear guides, which carry these heavy structural components in machine tools, are responsible for precision and smoothness of machine tool axes by withstanding cutting forces [28]. Therefore, the contact behavior of linear guides is obtained by the specially designed experiments to predict the holistic assembly behavior of a CNC system. The experiments make the method useful at early design stages

before building the whole CNC assembly for a topology optimization problem. Subsequently, experimental contact behavior is mapped onto the FE model by RCFM for linear guides.

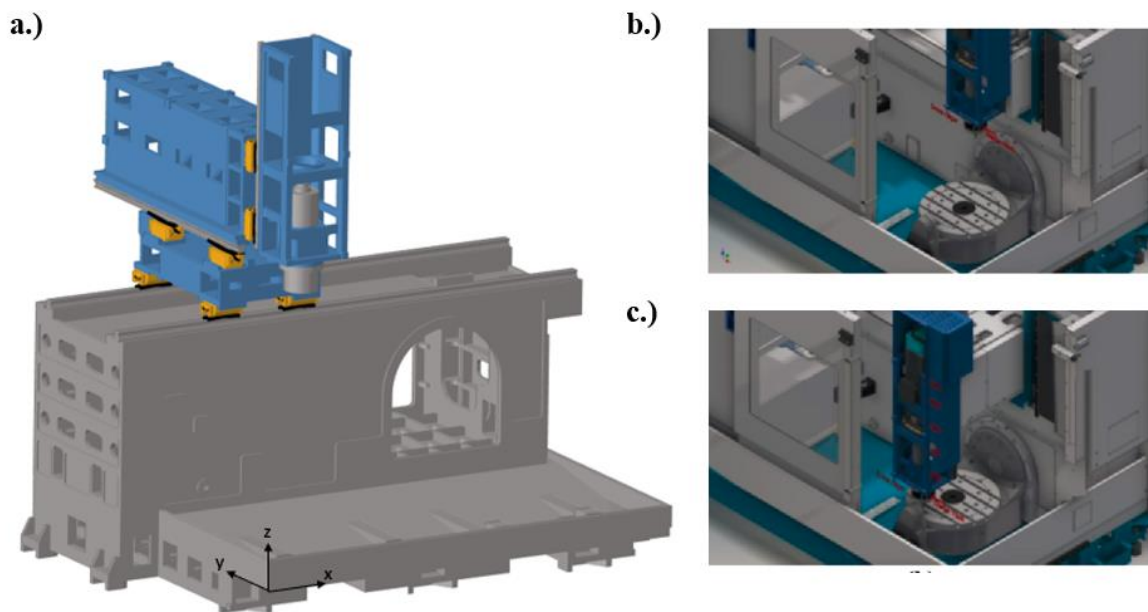


Fig. 1.11 a) The modelled machine tool structure model. Positions of the machine tool's axes for test conditions: b) rigid c) flexible

1.11.1. Topology Optimization with RCFM

In the design process of the machine tool structure, the RCFM was utilized by analyzing the bearing contacts of the linear guide. This method was then employed to optimize the structure. To create the FE model, a CAD model was used, and approx—4 million pyramid elements were utilized for the mesh in HyperWorks. Steel and cast iron were the materials used for the assembly, while 10% material damping was added to the system. However, no additional damping was implemented for the contact elements. The ball screw was modeled using a beam element, and the contact between the carrier and ball screw was assumed to be rigid. The linear guides, on the other hand, were modeled using the contact model explained earlier. Contact elements in the FE library were used to connect the other components outside the design domain. The FE model was fixed to the ground, and the structural loads were applied to the spindle tip. Fig. 11 shows a simplified version of the modeled five-axis machine tool. Before the optimization stage, the RCFM for the FE was verified by experiments as mentioned in an [24].

1.11.2. Topology Optimization with Thermo-mechanical RCFM

The virtual contact representation of Thermo-mechanical RCFM was used to model the thermo-mechanical contacts. The parameters of these contacts were identified based on the heavy cutting conditions and spindle speed of 15 K rpm. To determine the optimized shapes of the milling machine, the moving bodies were simplified using the proposed method on the potential domain. Firstly, the structure was thermally loaded by considering the heat generation of spindle bearings at 15K rpm in idle conditions. Then, the structure was optimized for minimum thermal compliance with volume fraction and displacement limitations. Following

this, it was optimized for minimum static compliance using the same constraints. To combine thermal loading with heavy cutting conditions, a tapered helical ball end mill cutter was used with Ti6Al4V as the workpiece material. The cutting forces were obtained using CutPro™ software, and the axial depth of the cut was 20mm with a feed rate of 0.050mm/tooth [29].

1.12. Results

1.12.1. Results of Topology Optimization with RCFM

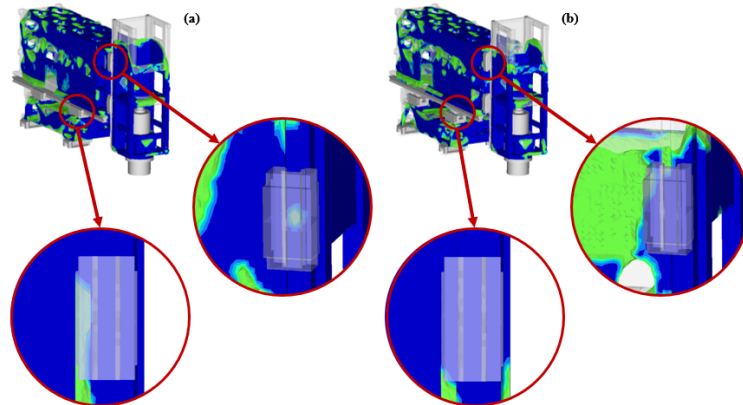


Fig. 1.12 The topology optimization for different contact methods (a) the PCM, (b) the RCFM.

Based on the optimization procedure carried out, the RCFM was initially executed for the machine tool structure, followed using Penalty Method to search for the unknown contact variables. Upon convergence, the optimization algorithm was executed, resulting in two optimized designs, as shown in Fig. 12. The optimized structure using the Penalty Method is shown in Fig. 12a, while the RCFM obtains Fig. 12b for the same constraints. The Penalty Method obtained an inaccurate contact stiffness between the components, resulting in incorrect load transmission calculations from one component to another in the contacts. As a result, the deformation predictions were also inaccurate, leading to unrealistic design obtained by the Penalty Method. The strain energy density transfer from the linear guides to the components is shown in Fig. 13, which helps in investigating the differences between the optimized designs.

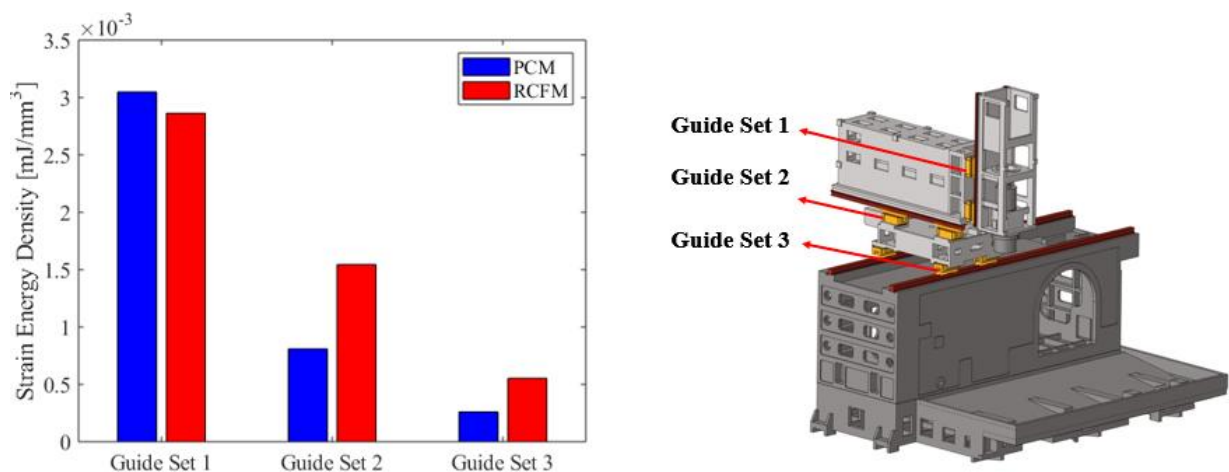


Fig. 1.13 Strain energy densities in the guide sets for both contact methods.

Based on the data in Fig. 13, it appears that the strain energy density transfer from the guides to the components drops considerably among the linear guides for the Penalty Method. However, this trend is more balanced for the RCFM. Interestingly, both cases experience a decrease in strain energy density from Guide Set 1 to Guide Set 3, which can be attributed to the applied load from the spindle tip. This load input causes strain energy transfer at the contacts, which then transfers the loads to the components. Therefore, it is expected that Guide Set 1 would have the greatest strain energy density, while Guide Set 3 would have the lowest. However, the sharp drop in strain energy density in the other guides for the Penalty Method was unexpected. This suggests that the automatically assigned Penalty Numbers caused the contacts to be modeled as more unstable than the actual case. As seen in Fig. 13, Guide Set 1's rigidity is predicted to be more significant, while Guide Set 2 and 3 are expected to be more flexible for the Penalty Method than the RCFM, reflecting the experimental behavior of the linear guides.

It seems that the optimization algorithm may not be producing accurate designs over the design domain, which could lead to unrealistic behavior in the Penalty Method. It appears that there is a sharp drop in the transferred force between the spindle holder and the sliding table, which may indicate that the design proposal obtained by the Penalty Method is not realistic. This could be due to mass removal from different areas, even though the same problem and optimization algorithm were used for both cases. Fig. 12 shows the specific areas where mass removal was suggested.

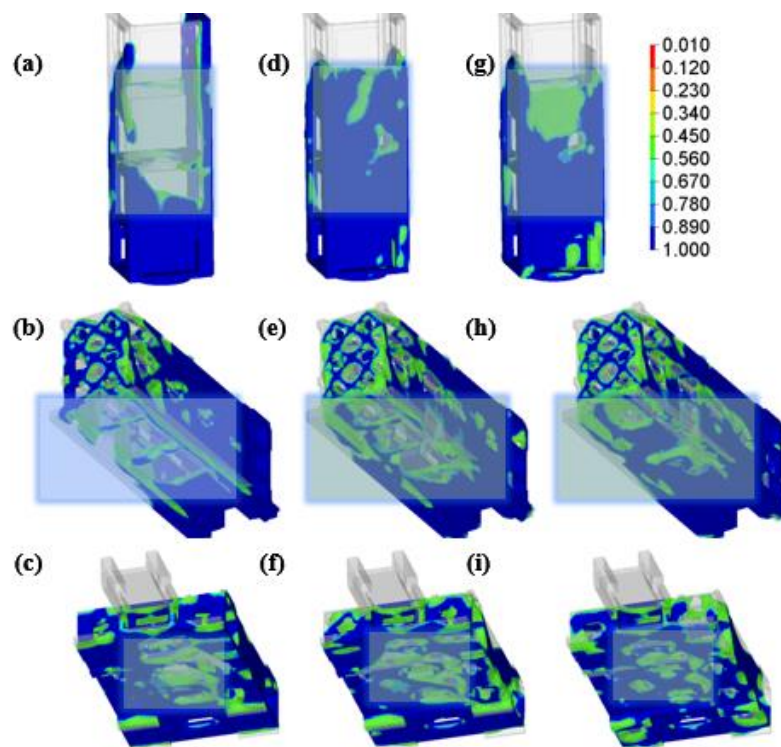


Fig. 1.14 The topology optimization results through (a, b, c) the single component optimization, (d, e, f) the PCM, (g, h, i) the RCFM.

Fig. 14 showcases the spindle holder, ram, and sliding table, with the legend indicating that blue regions are essential areas for the structure, whereas green to red regions signify allowable mass reduction areas. The optimized designs are presented in Fig. 14, with the red regions transformed into transparent wireframes. Different optimization methods were employed to obtain these results. Firstly, single and multi-component optimization approaches were compared, with each component optimized separately, as shown in Fig. 14a, 14b, and 14c. Secondly, multi-component optimization results were compared using Penalty Method and RCFM, with Fig. 14d, 14e, and 14f showing the Penalty Method optimization results, and Fig. 14g, 14h, and 14i showing the RCFM optimization results.

Single-component optimization posed the challenge of determining volume reduction percentages and boundary conditions between the contact interfaces. On the other hand, multi-component optimization automatically calculated volume reduction percentages for each component according to assembly conditions and load distribution, despite requiring more computational time. For single-component optimization, a 30% volume reduction was applied to each component (Fig. 14a, 14b, 14c), while multi-component optimization involved 30% reduction for the entire design (Fig. 14d to 14i). The contact interfaces played a significant role in determining the volume reduction amounts for each component by the end of optimization. Table 5 tabulates the volume reduction amounts of each component for the three optimization methods utilized in Fig. 14..

Table 1.5 Reduced Volume Percentage of Different Optimization Types

Component	Optimization for Single Components	Optimization for Multi-Components by employing PCM	Optimization for Multi-Components by employing RCFM
Spindle Holder	30%	22%	29%
Ram	30%	31%	29%
Sliding Table	30%	36%	32%

In the analysis conducted, it was found that the strain energy transfer from the spindle holder to Guide Set 1 is higher for the Penalty Method as compared to the RCFM. This is due to the fact that the contact interfaces in the Penalty Method are represented more rigidly than in the RCFM. As a result, the optimized tool holder designs in Fig. 14d and 14g show a 24% lower volume reduction amount for the Guide Set 1 and less mass subtracted areas between the Guide Set 1 to preserve the component rigidity. Additionally, it was observed that the static cutting force is applied to the spindle tip for all optimizations, with the direction changing invariably. This effect was seen in the single component optimization for the spindle holder in Fig. 12a. For this reason, the mass was subtracted from the left side of the spindle holder during the optimization process. However, in multi-component optimizations, a symmetric mass reduction was observed for the spindle holder.

Based on the data presented in Fig. 13 and Table 5, it appears that the Penalty Method has a lower strain energy transfer from the spindle holder to Guide Set 2 and 3 compared to the RCFM. This is since the contact interfaces are represented more flexibly by the Penalty Method, resulting in larger mass subtraction areas on the ram and sliding table between the

Guide Set 2 and 3. While the volume reduction amounts are close for both the Penalty Method and RCFM, the subtraction areas are more pronounced in the Penalty Method. Additionally, the single component optimization leads to a 12% lower volume reduction amount for the sliding table compared to the multi-component optimizations. However, the subtraction areas are more dominant between the Guide Set 3 on the table. Overall, these findings highlight the importance of multi-component optimization and contact representation for machine tools, proving the superiority of the RCFM over the Penalty Method and single-component optimization.

In this study, optimization was carried out to improve both the static and dynamic stiffness of a machine tool. The optimized designs resulted in increased static stiffness, preserved directional stiffness values, and reduced mass. To evaluate the effects of the contacts, the normalized FRFs of the optimized designs were compared with the initial design in the FE environment. Fig.15 shows the dynamic responses of the initial design and optimized designs using both methods. To ensure a proper comparison, the RCFM was used in both FRF simulations. The FRF results of the unoptimized design were also embedded in Fig.15 to highlight the mode shifts resulting from the mass reduced optimized designs. The structural modes shifted around 10-15% for the most flexible position in both methods. A similar trend was observed for the rigid position, with the structural modes shifting around 5-10%.

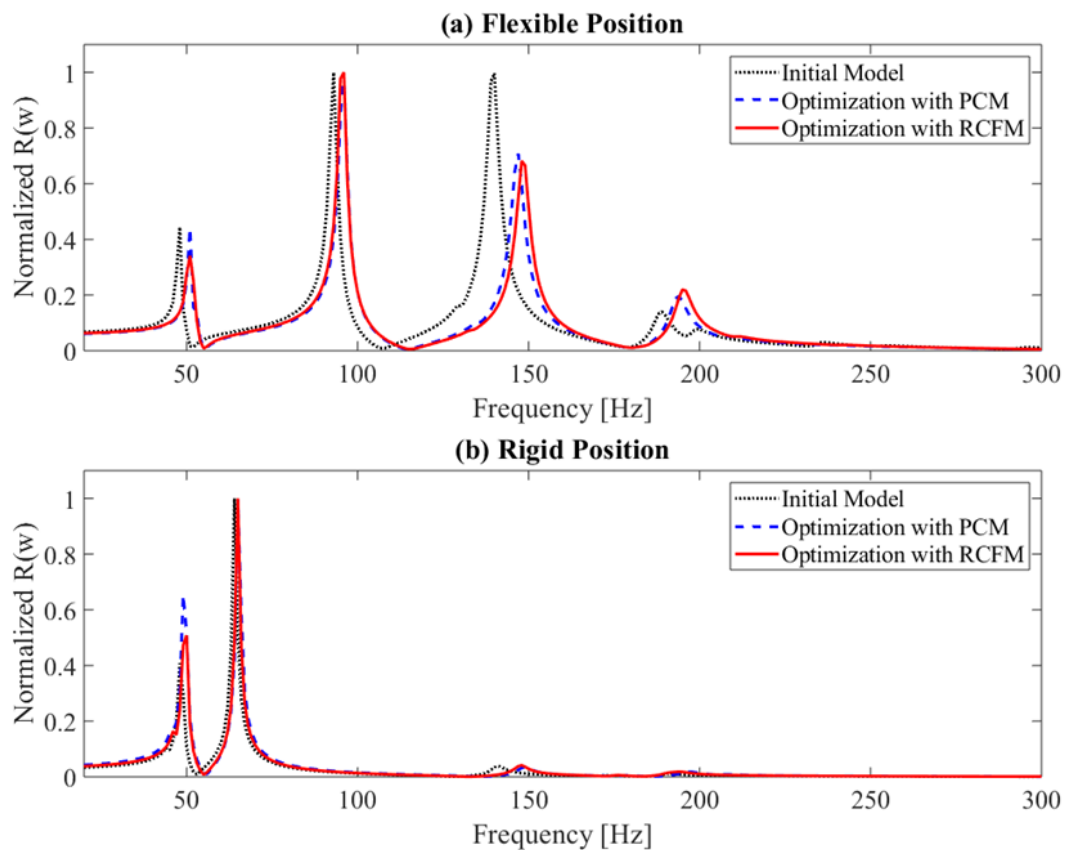


Fig. 1.15 Dynamic response of the optimized machine tool at: (a) the most flexible, (b) the stiffest position.

Based on our analysis, the most notable discrepancy between both the Penalty Method and RCFM outcomes can be observed in the fundamental modes of dynamic compliance for both positions. Specifically, the RCFM approach yielded 15%-25% lower amplitudes for both instances in comparison to both the Penalty Method. This observation is not unexpected, given that the fundamental modes are typically linked to assembly behavior. The reason for this difference is attributed to the RCFM's more realistic depiction of contact stiffness and precise force and strain energy transfer between the contacting components.

We conducted a study where we manufactured an optimized machine tool prototype based on a specific methodology. We then examined the prototype in terms of three efficiency parameters. By reducing its mass and using the same servo drivers, we were able to improve the physical capabilities of the machine. We measured the maximum velocity, acceleration, and jerk limits and found significant improvements in the physical capabilities of the machine tool structure. You can find more details about the improvements made to the machine tool structure in the provided resource [24].

1.12.2. Results of Topology Optimization with Thermo-mechanical RCFM

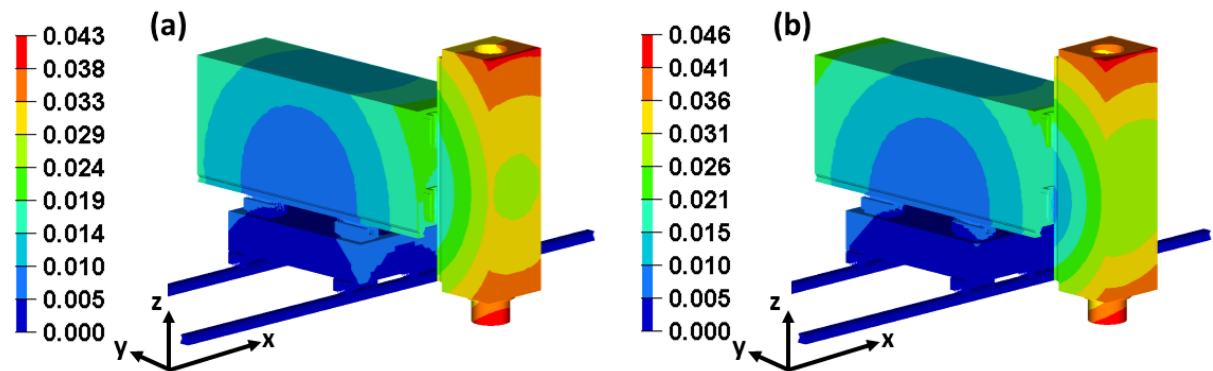


Fig. 1.16 Total deflection [mm] of the structure under (a) thermal loading (b) coupled loading.

Fig.16 illustrates the deflection predictions for the proposed thermo-mechanical contact method. To verify the FE predictions, laser sensors, and thermal cameras were used to measure thermal deflections under idle cutting conditions at 15 K rpm [27]. The elastic deflections of the spindle tip under loading were also measured by laser sensors in different directions [26]. The experiments showed that the predictions were in good agreement with the experimental results, where the difference was less than 10% for elastic and thermal loading conditions by employing the proposed thermo-mechanical contact method for the FE model. The thermal and static optimization results are represented in Figs. 17 and 18, respectively. Red regions indicate compulsory areas, while blue regions illustrate subtractable areas for the stiffened structure in the legends of Figs. 17 and 18 for the optimum mass distribution. One can observe the effect of spindle bearings on the contact areas of the components in Fig. 17. Realistic heat transfer was provided with the help of the proposed method. As a result, the total mass was reduced by 15 %, while the directional stiffness of the axes was maintained.

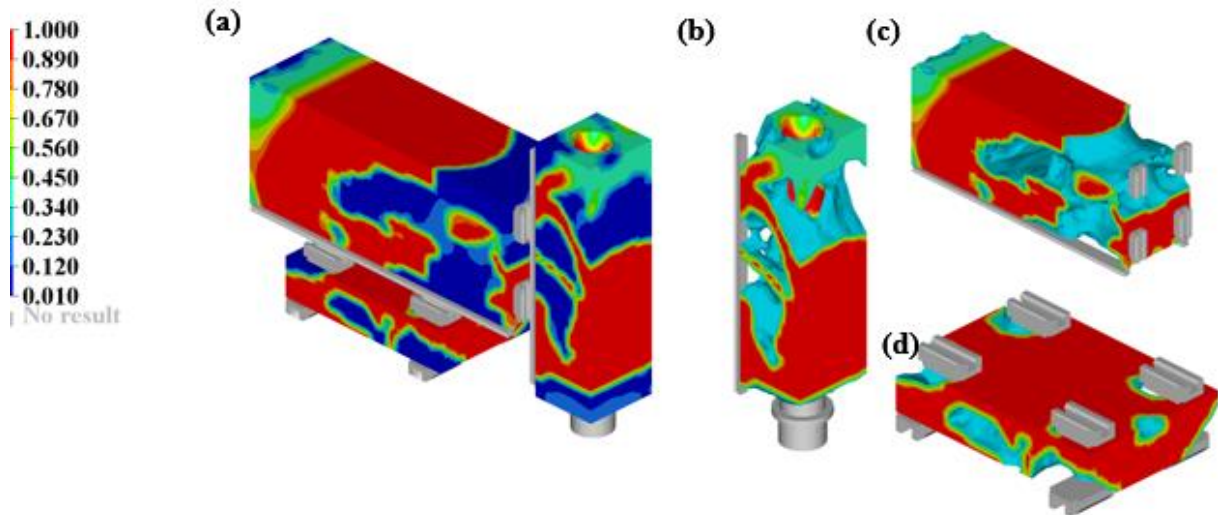


Fig. 1.17 The results of thermal top. opt. (a) the assembly (b) the spindle holder (c) the ram and (d) the sliding carriage

After conducting thermal optimization, we proceeded with static optimization on the same milling machine using coupled loading conditions (as shown in Fig. 18). During this process, we observed deflections caused by both thermal and static loading. To obtain accurate deflection and stiffness data, we implemented a contact method that proved to be effective in providing realistic results. The optimization process revealed that the effects of thermo-mechanical contact were particularly notable in the spindle holder and the ram. To achieve this, we subtracted the regions on these components at the position of the upper spindle bearings at the spindle head and ram. While the thermal optimization subtracted the related area at the ram, the static optimization subtracted the related area at the spindle holder, thanks to the proposed thermo-mechanical contact model. Consequently, we were able to reduce the total mass by 15%, while still maintaining directional stiffness behavior for both thermal and static loading cases.

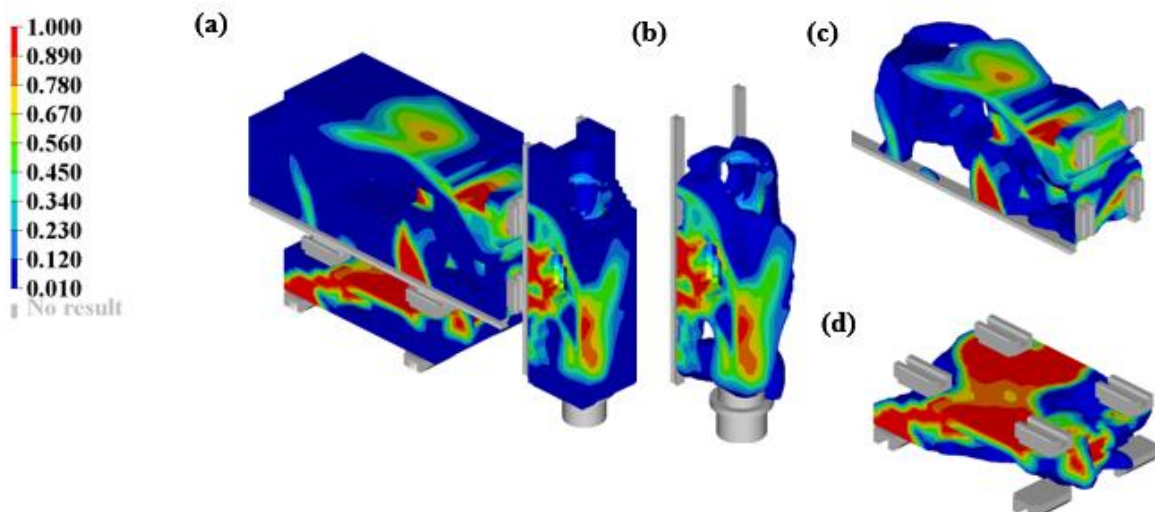


Fig. 1.18 The results of static top. opt. (a) the assembly (b) the spindle holder (c) the ram and (d) the sliding carriage

1.13. Conclusions

In this study, Signorini's Contact Problem has been introduced as a new aspect of Machine Tool Research. Additionally, the FE implementation of the Signorini problem has been presented, along with a detailed explanation of thermo-mechanical contact elements in FE. However, the study also sheds light on the problems with FE algorithms. Lastly, the topology optimization problem with contact constraints has been introduced as a potential solution to the aforementioned issues.

Our study in the machine tool field has yielded significant results. For the first time, we have addressed multi-component topology optimization problems for machine tools, with a focus on contact phenomena for the SIMP algorithm. We have also shown the effects of contact force instability due to FE algorithms on topology optimization problems. Our proposed RCFM method has been successfully applied to thermo-mechanical topology optimization problems. By employing this method, we have avoided inaccurate strain energy transfer and the tendency to calculate higher contact stiffness data than the real one. This is particularly important for machine tool design, as the entire stiffness of a machine tool depends strongly on the least stiff elements, which generally include many contact regions. Our approach has significantly reduced computational load and deviations between measurements and FEM predictions for the calculation of reaction forces and compliance values. We have demonstrated the effectiveness of our method by successfully implementing it for the topology optimization of a milling machine.

2. DESIGN AND ANALYSIS OF LARGE-SCALE MILLING MACHINES BY CONSIDERING MECHANICAL INTERFACES

2.1. Summary and Novelty

This study demonstrates the analyses and optimization of large-scale gantry and horizontal milling machines with experimental results on manufactured prototypes by considering the mechanical interfaces (with RCFM). The FE analysis results of the initial milling machine designs are shared with a detailed discussion, and the measurement results on structural dynamics are shared. Critical points in designing and optimizing large-scale machine tools are discussed. These discussions include :

- Comparison of structural behavior changes for similar structured but different sized gantry-type 5-axis CNC machine tools.
- Natural frequency optimization of machine tool and spindle critical speeds identification for horizontal milling machine.

Structural optimization was offered for improvements after determining the structurally critical parts for both gantry and tower-type milling machines. The extension of the RCFM method for Level-Set Topology Optimization (LSTO) is demonstrated on a gantry structure. Lastly, structural improvements are discussed according to determined critical points.

2.2. Introduction

Large-scale milling machines are frequently employed by automotive, aerospace, and die/mold industries due to their expandable machining span, significant structural rigidity properties, and motion precision and accuracy promise [30]. A classical large-scale milling machine's axis stroke is between 2500 and 3000 mm and can be produced by welding and casting techniques [31]. However, a super large-scale milling machine axis stroke can be extended to 7400 mm and must be constructed with advanced casting techniques. Advanced casting capability is crucial for creating a super large-scale milling machine with superior damping properties.

Gantry Type Large-Scale Milling Machines

A competitive heavy-duty 5-axis gantry milling machine can process workpieces that are ranged from 16 to 20 tones, with 8 to 10 μm axial precision at X and Y of machine coordinates. In contrast, these axes' positional accuracy ranges from 10 to 15 μm . Generally, fork-head spindle structures are employed for heavy-duty 5-axis gantry-type milling machines with 95 to 120 degrees rotation capacity at A-axis, while C-axis can rotate 360 degrees. The speed of fork-head spindles mounted on gantry-type 5-axis CNCs ranges from 5000 to 25000 rpm for heavy-duty machining applications. The Z column's axial and positional accuracy/precision can change between 3 and 5 μm .

When it comes to constructing large-scale gantry-type milling machines for heavy-duty machining applications, welded, or cast components are typically used [32, 33]. However, there is a growing trend towards using welded components due to their lower manufacturing costs compared to cast complex machine tool parts. Welding techniques also allow for the usage of carbon-fiber-based composites in machine tool structures which can be just as reliable as cast components. However, these composites do have anisotropic properties that cannot maintain

the required stiffness levels for long structural components and spindle structures of machine tools[34]. Welding thick metal components with techniques such as Gas Metal Arc Welding (GMAW), Manual Metal Arc Welding (MMAW), and Laser Arc-Hybrid Welding (LAHW) can cause issues such as distortion, porosity, and weak material properties [35]. As a result, large-scale 5-axis gantry-type machine tools produced with welding techniques typically have Y-axis strokes between 2500 and 3000mm as standard lengths.

To extend the stroke of the X and Y axes of large-scale milling machines, cast components with superior damping properties are required to maintain the desired stiffness properties. Structural design and optimization of large-scale gantry-type milling machines involve major parameters such as the structural properties of the gantry, which generally assembles with welding joints that can cause loss of stiffness. Therefore, research in the literature focuses on crossbeam optimization for gantry components to improve the stiffness behavior of heavy-duty machine tool structures[36,37]. Modelling mechanical interfaces in FE analyses is also critical during the simulation and structural optimization for even regular-size machine tools [24]. However, massive component sizes and weights make contacts more critical for large-scale machine tools. Thermal compensation techniques could also be more practical for large-scale machine tools. Furthermore, thermal design/optimization requires advanced techniques for thermal distortion detection and compensation, even for a medium 5-axis CNC machine[38]. Therefore, designs for preventing thermal distortions are more effective in large-scale milling machines.

2.3.Research Gap

The structural stiffness increase should be parallel or higher than the mass increase to preserve a standard structural behavior in large-scale milling machines. Therefore, designing and manufacturing large-scale machine tool structures requires careful structural stiffness and mass distribution planning to meet static and dynamic requirements. Regarding stiffness and mass distribution planning, finite element (FE) analysis and structural optimization tools are the most common tools for machine tool design. One of the most critical issues in machine tool simulations is modeling mechanical interfaces in an FE environment for the stiffness planning of a CNC structure. The machine tool contact interfaces can be represented using different methods in an FE model, which affects the assembly stiffness of CNC structures. In the literature, hybrid methods are used to improve contact interface modeling [1], and RCFM [24] is employed. Still, the following questions remained unclear during the design of large-scale milling machines:

- How do the bigger components affect the structural behavior of large-scale milling machines?
- Which FE analyses should be applied to large-scale milling machines between the design and manufacturing phases?
- What are the structurally critical points during the design of large-scale milling machines?
- How critical components in a large-scale milling machine can be decided, and what can be done for the final design iterations?
- Which structural improvements can be done before and after manufacturing large-scale milling machines?

In this study, the answers to these questions tried to be answered by sharing analysis and improvement processes of two large-scale sizes but the same structured 5-axis gantry and a horizontal milling machine. The extension of the RCFM method for Level-Set Topology Optimization (LSTO) [39] is also exemplified.

2.4.Design of Large Machine Tools

To extend the stroke of the axes of large-scale milling machines, cast components with superior damping properties are required to maintain the desired stiffness properties. The casting method benefited design strategies as follows: The mainframes are designed as cast mono-block parts, which makes this design unique compared to other CNC structures in the machine tool industry. The mono-block central bodies will imitate a single-volume structure when considering geometric and dynamic behaviors. The superiority of the cast materials over the welded ones is their ability to damp. The significant damping ability of gray iron is at least threefold in steel structures [40]. The X and Y axes' frames and machine base are made of GG25, and GG50 is employed to build the Z-axis. The base part of the milling machine is also cast as a mono-block piece which weighs 24 tons. Therefore, the first mode of the structure is expected to demonstrate a mode shape of a single-volume structure. The targeted features of the machine tool are shown in Fig.1.

The X-axis of the machine (gantry) is longer than the usual standards. Thus, cast components may not be enough to maintain the required stiffness. Therefore, the internal structure of the gantry is supported with unique ribbing elements. Additionally, pretensions are directed to the gantry surface during the casting process. Moreover, the rails of the linear guides are cast with these mono-block components to avoid structural deformations on the X and Y axes of the machine. The pretensions and cast railways are indicated in Fig.1b. Additionally, a rack and pinion mechanism-based linear motion system is employed instead of classical drive screw systems. This type of linear motion system exposes lesser efficiency losses.

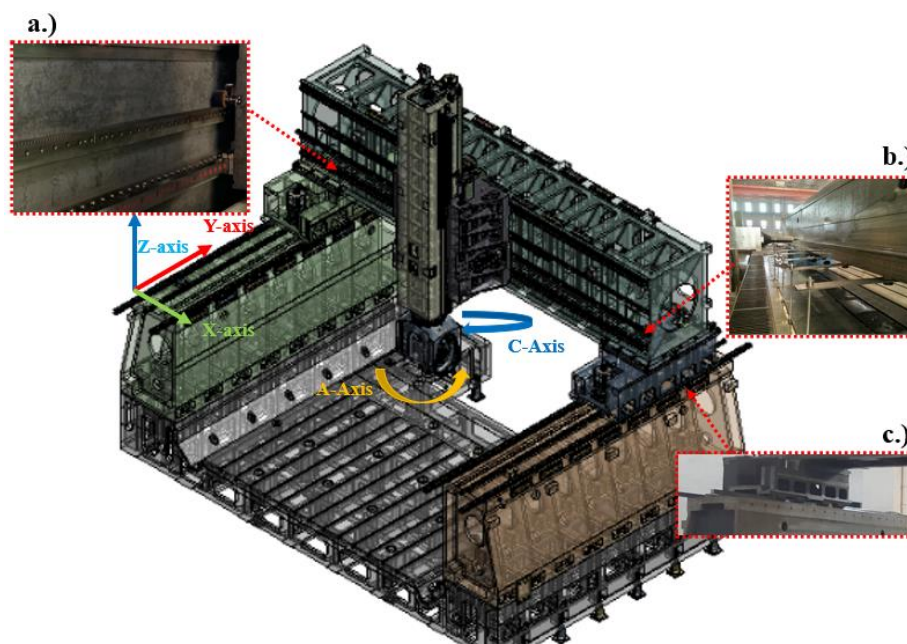


Fig. 2.1 Casting method benefited design strategies a.) The rack and pinion system used for linear motion system, b.) The pretensions on the gantry surface due to casting, and cast rails of linear guideways, c.) The pipeline locations for the cooling of main frame

Moreover, the structural configuration of the rack and pinion mechanism on the gantry provides additional support for the Z column, as shown in Fig.1a. As mentioned earlier, thermal distortion-preventing designs are more effective compared to thermal compensation techniques during the design stage of large-scale machine tools. Thus, as a cooling precaution, there are pipelines for water circulation under the slideways of the X and Y axes to keep the temperature change at a minimum. These pipes are inserted during the casting process. The pipeline locations for central frame cooling can be seen on the manufactured prototype in Fig.2a.

2.5.Large-Scale Gantry Type Machine Tools

A super large-scale 5-axis gantry type CNC structure can reach sizes from 11500 mm to 16000 mm at the Y-axis, and this construction can be between 6600 mm to 8500 mm at Z-axis. These size changes result in enormous mass changes between the CNC specs, even though the gantry (X-axis) remains its size. To exemplify, two different large-scale 5-axis gantry-type milling machines are compared in this study.

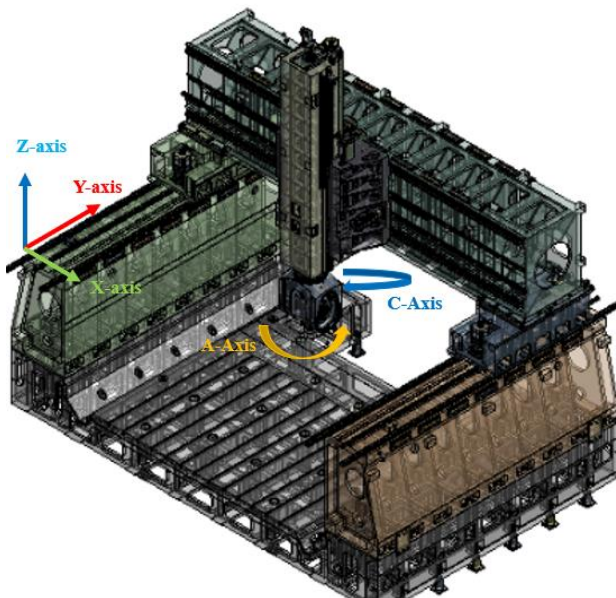


Fig. 2.2 CAD data of the subjected 5-axis CNC with general machine coordinates.

As large-scale gantry type milling machines, IGM FR 3500, IGM FR 3500XL are considered, and these machines share the exact gantry sizes (X-axis), while the other components have similar structures (Y and Z axes) but have different sizes. These machines are produced by Igrek Machine Tools. The classic model (IGM FR 3500) weighs 70 tons, the large one (IGM FR 3500XL) weighs 120 tons. The axial strokes of IGM FR series are given in Table 1 below.

Table 2.1 The axial strokes of IGM FR series.

Machine Type	X Stroke (mm)	Y Stroke (mm)	Z Stroke (mm)
IGM FR 3500	3500 mm	2500 mm	1400 mm
IGM FR 3500XL	3500 mm	6500mm	1400 mm

2.5.1. FE Analyses

This section answers the question, ‘How do the bigger components affect the structural behavior of a large-scale 5-axis gantry-type milling machine?’ IGM FR 3500 and IGM FR 3500XL are considered. The IGM FR 3500 weighs 70 tons, while the IGM FR 3500XL is 120 tons. They have similar dimensions on X and Z axes; the only difference is the Y-axis, as indicated in Table 1. Another question was, ‘Which FE analyses should be applied to large-scale milling machines between the design and manufacturing phases?’ Since the dimensions and masses of machine tools are considered a static deflection analysis for the least stiff position of the structure due to its weight, it is required to predict maximum deflections and take necessary actions during manufacturing and assembly. The second FE analysis should be a modal analysis to predict the dynamic behavior of the milling machine. As stated, mechanical interface modeling in an FE environment is critical for large-scale machine tools. The penalty algorithm (which exists in nearly every FE software) and RCFM will be employed together for mechanical interface modeling in FE for large-scale milling machines. The pure penalty algorithm (prone to assigning higher contact stiffness values) is employed with 0.2 relaxation tolerance on contact interfaces in the FE model for the main body connections. Since these parts are highly rigid, this contact algorithm is expected to give accurate predictions in FE analyses for contact regions of the machine base and mono-block parts. Linear guides, bearings, and drive screw connections are modelled with RCFM [].

First, the CAD and meshing details of IGM FR 3500 are shared, and then similar data is given for IGM FR 3500XL. Later, the FE results will be compared with the experimental ones.

IGM FR 3500 Data

The CAD model of the assembly is simplified and is composed of 377 parts in total. After Jacobian and skew ratio checks, 14117354 pyramid elements are employed for meshing with 2538140 nodes.

IGM FR 3500 XL Data

The CAD model of the assembly is simplified and composed of 1436 parts in total. Approximately 3.7 million hex mesh elements are employed Jacobian and skew ratio checks.

2.5.2. Deflection Analysis

The static FE analysis predicts displacements under gravity force since the CNC structure has extreme sizes. The gravitational force is applied at the - Z-axis direction of the machine tool coordinates. The structure is fixed from the pads under the machine base. The FE model is positioned at the least stiff position to detect the maximum deflection amount for IGM FR 3500. The total deflection of the CNC structure is shown in Fig.4, which is 0.164 mm. Fig.3 indicates the spindle-gantry connection is the weakest point of the structure. Therefore, structural optimization techniques should be employed on the Z-column, gantry, and between the connection of them to create a superior design.

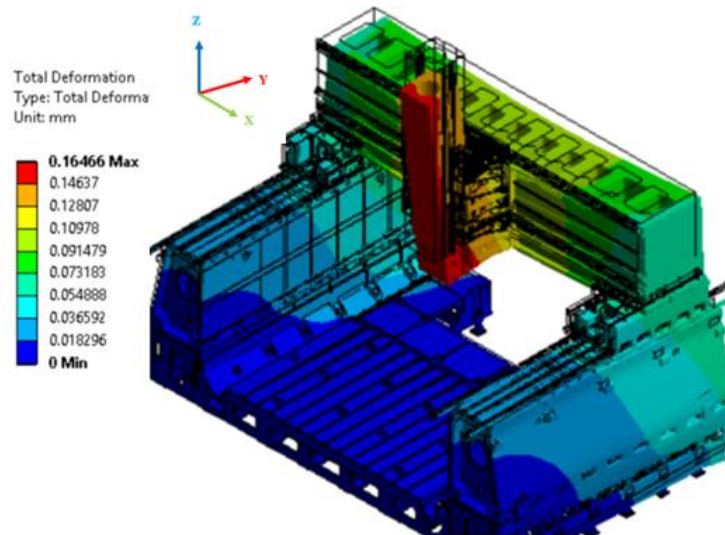


Fig. 2.3 The total static deformation of the CNC under gravitational force at the least stiff position.

However, the total deformation of the gantry structure is predicted to be 0.109 mm. In comparison, these deformations are detected as 0.002mm for X-axis, 0.03mm, and 0.09mm for Y and Z axes, respectively. These results can be interpreted as the rigidity effect of the cast mono-block base and mainframes on the gantry structure. Moreover, these results demonstrate that the X and Y axes' 10-micron accuracy/precision target is easily achievable by the machine tool, even at the most flexible position, with the implementation of a few compensation techniques. The directional deformations are illustrated in Fig.4.

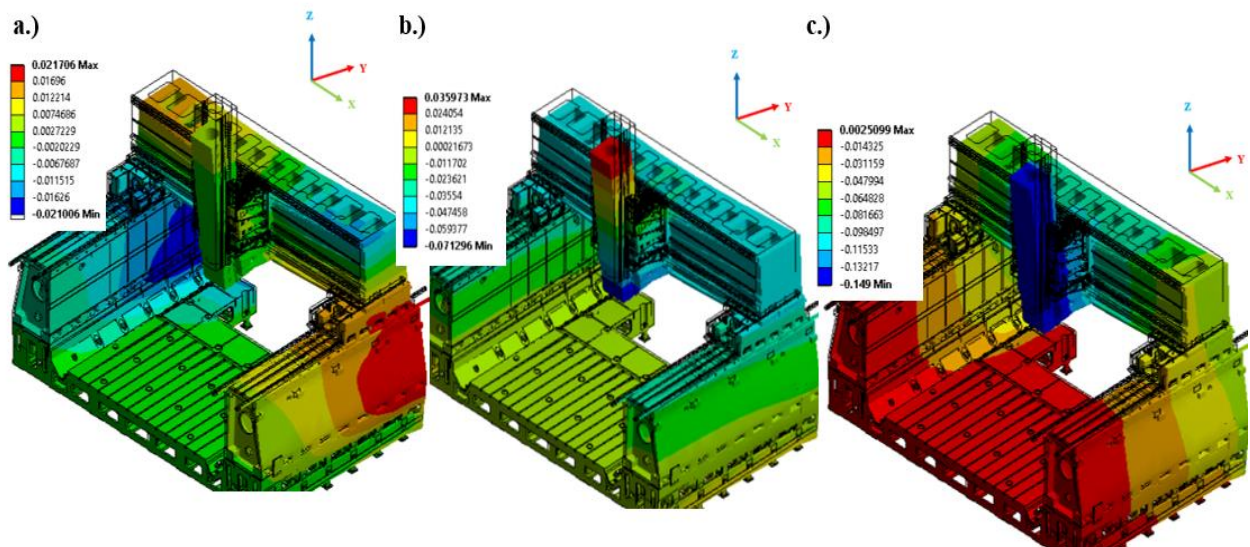


Fig. 2.4 The directional static deformation results of the CNC under gravitational force at the least stiff position. a) X-axis, b) Y-axis, c) Z-axis.

The maximum deformation is found as 0.002mm on X-axis, proving that the mono-block cast frames behave like a single volume. 0.07mm and 0.149mm deformation values are detected on Y and Z axes. This result again points out the weakest regions for the entire assembly. Furthermore, the deformations on Z-axis prove the relation between displacements of Y and Z axes. Thus, one can conclude that Y-axis deformations are related to the straightness errors on Z-axis from the similar deflection results.

Since the IGM FR 3500 XL has the exact dimensions at Z and X axes as IGM FR 3500, similar deflection amounts are observed, the maximum deflection is observed around the gantry region since the linear guides are relatively weak elements compared to other large cast blocks.

2.5.3. Modal Analysis

2.5.3.1. IGM FR 3500

Subsequently, a modal analysis is employed to find the natural frequencies of the IGM FR 3500. The results indicate a natural frequency range between 20 and 70 Hz, which is smaller compared to regular-sized machine tools, however, it is an expected result when the extreme sizes of the CNC structure are considered. The natural frequencies of the first 6 mode are tabulated in Table 2.

Table 2.2 The modal analysis results for the first 6 modes of IGM FR 3500.

<i>Mode Number</i>	<i>Frequency (Hz)</i>
<i>1st. Mode</i>	21.8 Hz
<i>2nd. Mode</i>	23.9 Hz
<i>3rd. Mode</i>	41.8 Hz
<i>4th. Mode</i>	43.8 Hz
<i>5th. Mode</i>	64.2 Hz
<i>6th. Mode</i>	69.3 Hz

The first three mode shapes are indicated in Fig.5, the 1st mode shape is 21.8 Hz, and makes a swinging motion along X-axis. The 2nd mode shape is 23.9 Hz, and it demonstrates a leaning motion along Y-axis. These two adjacent modes prove the cast mono-block structures behave like a single-volume structure. The 3rd mode is around 41.8 Hz and shows torsional features which are undesired for machine tool design. More powerful connections and structures are recommended for gantry and sliding tables.

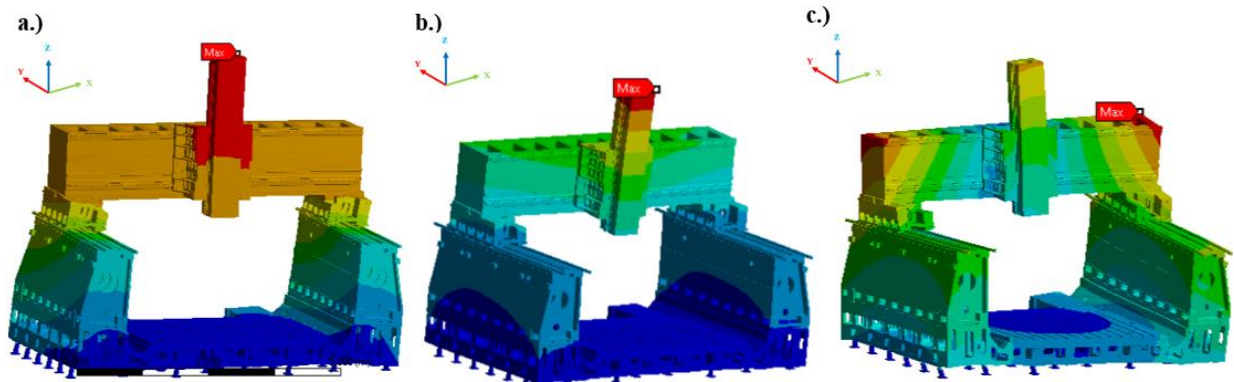


Fig. 2.5 The mode shapes from the FE analysis a) 1st Mode (21.8 Hz), b) 2nd Mode (23.9 Hz), c) 3rd Mode (41.8 Hz).

The remaining results of the modes is illustrated in Fig.6. The 4th mode shape is 43.8 Hz which caused from the gantry structure. The 5th and 6th modes are detected as 64.1 Hz and 69.3 Hz, respectively. These mode shapes are related with the Z column and gantry structures.

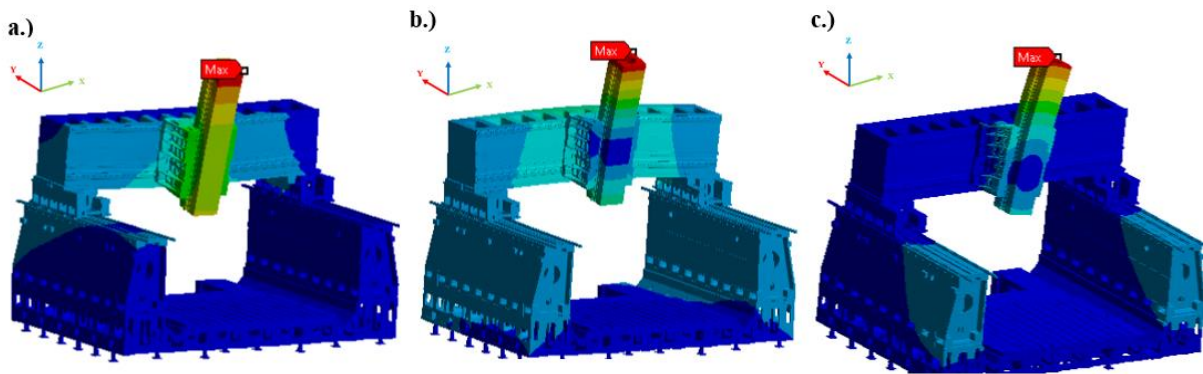


Fig. 2.6 The mode shapes from the FE analysis a) 4th Mode (43.8 Hz), b) 5th Mode (64.2 Hz), c) 6th Mode (69.3 Hz).

2.5.3.2. IGM FR 3500 XL

Subsequently, modal analysis is employed to find the structure's natural frequencies of IGM FR 3500 XL. The results indicate a natural frequency range between 36 and 80 Hz.

Table 2.3 The modal analysis results for the first 5 modes of IGM FR 3500 XL.

<i>Mode Number</i>	<i>Frequency (Hz)</i>
<i>1st. Mode</i>	36 Hz
<i>2nd. Mode</i>	42 Hz
<i>3rd. Mode</i>	50 Hz
<i>4th. Mode</i>	79 Hz
<i>5th. Mode</i>	80 Hz

The first two mode shapes are indicated in Fig.7. In the first mode, back and forth movement on the spindle, the gantry and body columns are observed at 36 Hz. This situation is also observed in static deflection analysis. The second mode value is 42 Hz, and its effect is seen as the swinging movement of the gantry and spindle structure together with the body columns.

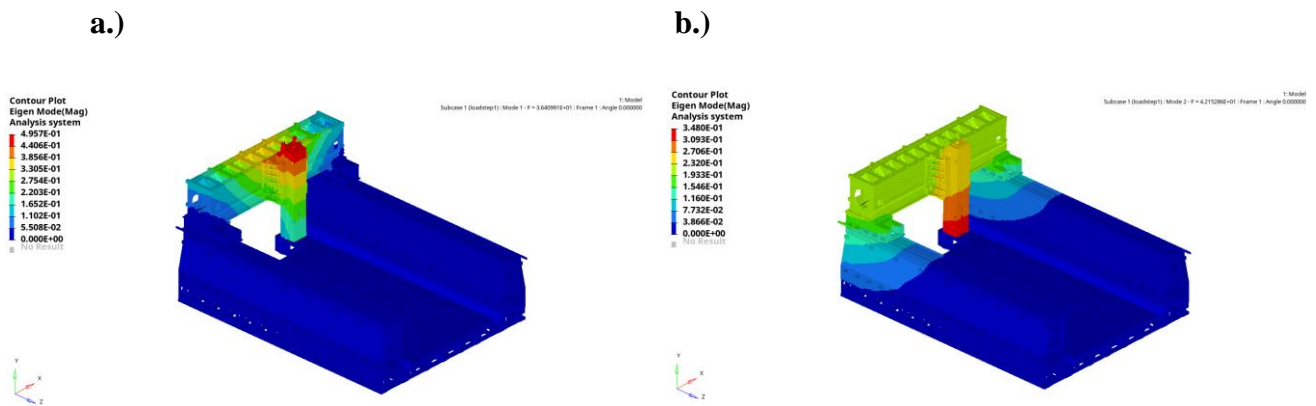


Fig. 2.7 The mode shapes from the FE analysis a) 1st Mode (36 Hz), b) 2nd Mode (42 Hz).

The last three mode shapes are indicated in Fig 8. The third mode is 50 Hz and is observed as the oscillating movement of the spindle structure on the gantry. The fourth mode value is 79 Hz, as illustrated in Figure 8. The body columns, gantry, and spindle act as one piece and make bending movement at the 4th mode. The fifth mode value is 80 Hz, and its effect is seen on the gantry.

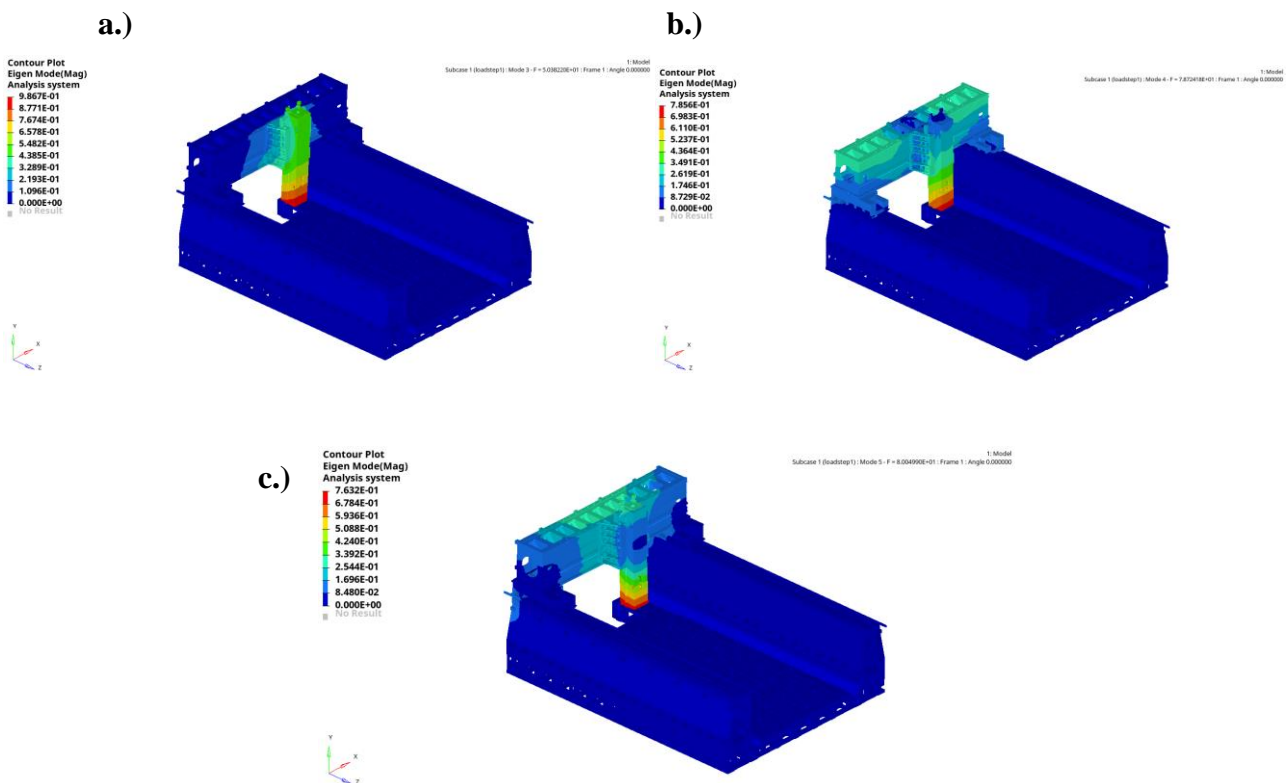


Fig. 2.8 The mode shapes from the FE analysis a) 3rd Mode (50 Hz), b) 4th Mode (79 Hz), c) 5th Mode (80 Hz).

The mode values obtained from the FE analysis results are given in Tables 2 and 3. The modes of the IGFR3500 XL were generally found in the 36-80 Hz range. For the IGFR 3500 machine, this range was found in the range of 21-69 Hz, and the results were also verified with experiments on the manufactured prototype, which will be shared later. Structurally, the IGFR3500 main body is monoblock, and the IGFR3500 XL has an extended main body structure, as indicated in Fig.9. The mechanical interface that connects the two main body profiles makes the modeling of the contact conditions in the FE extremely difficult. During the simulations, all surfaces that may be in contact with main body interfaces are assumed to be in contact. This situation represents the most rigid state encountered in the body structure. However, the rigidity of the structure can be variable depending on the clamping (or pulling) conditions of the main body interfaces.

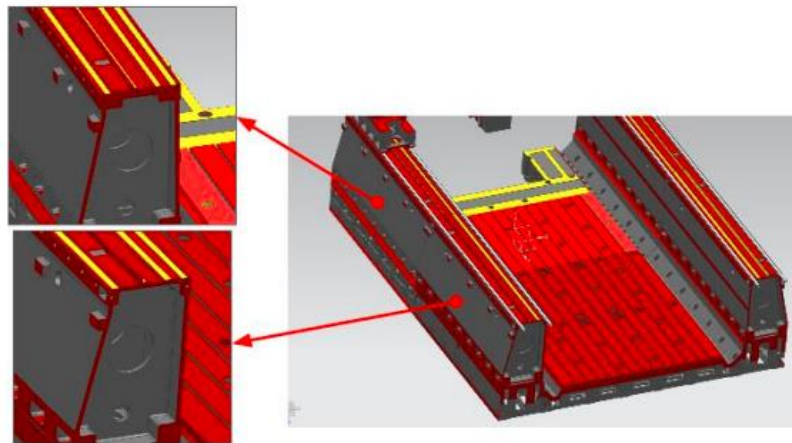


Fig. 2.9 IGFR3500 XL has an extended main body structure.

2.6.Experimental Results

2.6.1. IGM FR 3500 Modal Investigation

To provide a more comprehensive overview of the hammer test results, we have broken down this section into three subparts that examine the modal behavior outcomes when the machine tool is operating at its weakest position. By doing so, we can gain a more detailed understanding of how the machine tool performs under these extreme conditions.

a.)



b.)



c.)

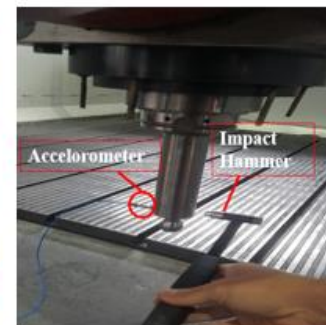


Fig. 2.10 The location and reference X-Y plane of the accelerometers, and the hammer tests at a.) the Main Bodies b.) the Gantry c.) the Spindle for IGM FR 3500.

i) Modal Investigation of the Machine Base and Main Frames:

Firstly, the impact and vibration data were collected from 24 distinct points with the impact hammer test in the direction where the body part is the most flexible (YY direction based on the machine axes) for the considered region. PCB 626B03 type accelerometer and PCB 086C05 oversized hammer were used in these measurements (See Fig.10a). The natural frequencies and dynamic parameters obtained from the modal tests are presented in Table 4 by comparing those of the FE analyses.

Table 2.4 The Comparison of results obtained from the FE and impact hammer tests for the body columns for IGM FR 3500.

Modes	Natural Frequencies obtained by the FEM (Hz)	The results obtained by the Hammer Test and FE analyses			
		Natural Frequency (Hz)	Modal Stiffness (N/m)	Damping Ratio (%)	Receptance of FRF ($\mu\text{m/N}$)
1st Bending Mode	21.8	18.4	3.6×10^8	2.1	0.022
1st Torsional Mode	41.8	48.8	4.8×10^9	0.9	0.011

As seen from Table 4, the natural frequencies calculated by FE analyses are close to the measured data of tests. As a result, the body components of the machine tool are produced at the predicted dynamic rigidity values.

ii) Modal Investigation of the Gantry:

Impact Hammer tests were also conducted on the gantry which correlates the motion between Y-axis and the Z column. In these measurements, PCB 626B03 type accelerometer and PCB 086C05 oversized hammer were used, and 24 different points were measured in total (See Fig.10b). The natural frequencies and dynamic parameters obtained from the modal tests are tabulated in Table 5 by comparing those of the FE analyses.

Table 2.5 The Comparison of results obtained from the FE and impact hammer tests for the gantry for IGM FR 3500.

Modes	Natural Frequencies obtained by the FEM (Hz)	The results obtained by the Hammer Test and FE analyses			
		Natural Frequency (Hz)	Modal Stiffness (N/m)	Damping Ratio (%)	Receptance of FRF ($\mu\text{m/N}$)

<i>1st Bending Mode</i>	43.8	50.1	2.46 x 10 ¹⁰	0.15	0.028
<i>1st Torsional Mode</i>	64.2	64.6	1.33 x 10 ¹⁰	1.30	0.005

As can be seen in Table 5, the 1st Bending Mode was calculated with a lower error rate compared to the 2nd Torsional Mode.

iii) Modal Investigation of the Z column:

The hammer tests were performed on the Z column, which carries the spindle. These tests employed PCB 353B33 type accelerometer and PCB 086C05 type impact hammer (Fig. 10c). Measurements were taken from 18 points in total. All measurements were repeated in the XX and YY directions.

Impact hammer test results can be seen in Table 6. The spindle has close natural frequencies compared to the machine tool structure in the X and Y directions. However, the most flexible mode of the spindle in the Y direction is two times weaker than the most flexible mode in the X direction. In other words, the spindle's dynamic stiffness decreases during the machine's Y-axis movements. Sometimes, there might be chatter about where rigid tools and tool holders are used. Especially considering the spindle's 1st and 2nd modes, there is a high probability for chatter at 1500 rpm and 6000 rpm.

Table 2.6 The most flexible modes of the Spindle and Z column measured by impact hammer tests for IGM FR 3500.

<i>Modes</i>		<i>The results obtained by the Hammer Tests</i>			
		<i>Natural Frequency (Hz)</i>	<i>Modal Stiffness (N/m)</i>	<i>Damping Ratio (%)</i>	<i>Receptance of FRF ($\mu\text{m/N}$)</i>
<i>XX direction</i>	<i>1st Bending Mode</i>	26.9	2.63 x 10 ⁷	4.92	0.392
	<i>2nd Bending Mode</i>	89.5	1.31 x 10 ⁸	3.92	0.115
	<i>3rd Bending Mode</i>	171.9	1.50 x 10 ⁸	3.42	0.122
<i>YY direction</i>	<i>1st Bending Mode</i>	23.7	2.44 x 10 ⁷	2.81	0.823
	<i>2nd Bending Mode</i>	106.5	8.58 x 10 ⁷	4.89	0.048

	3rd Bending Mode	190.9	4.98 x 10 ⁸	3.31	0.037
--	------------------------------------	-------	------------------------	------	-------

2.6.2. IGM FR 3500 XL Modal Investigation

The results of the modal analysis tests performed for the IGRF35-XL are presented. Modal analysis was carried out with the impact hammer test on the main body, gantry, and the Z column of the CNC machine tool. Results can be found below.

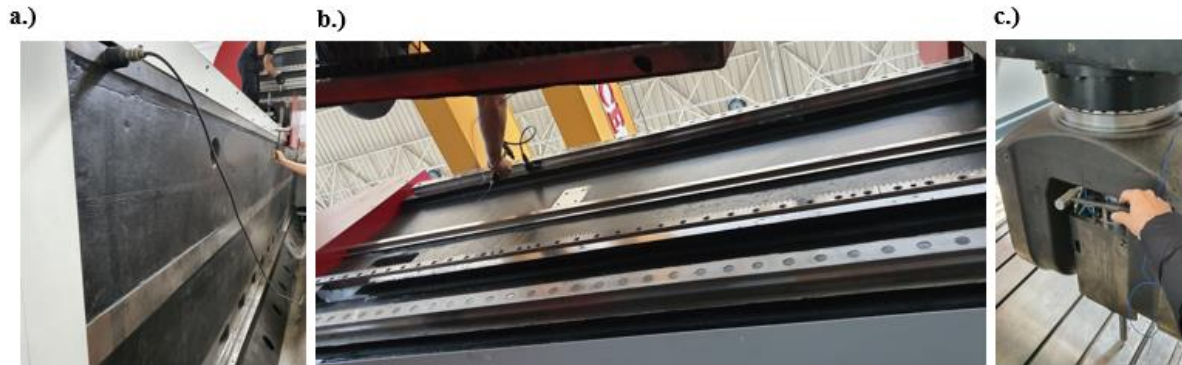


Fig. 2.11 The location and reference X-Y plane of the accelerometers, and the hammer tests at a.) the Main Bodies b.) the Gantry c.) the Spindle for IGM FR 3500 XL.

i.) Modal Investigation of the Machine Base and Main Frames:

Impact and vibration data were collected from 36 points with the impact hammer test in the direction where the body part is most flexible (YY direction based on machine tool direction). These measurements used the PCB 626B03 type accelerometer and PCB 086C05 large-size impact hammer. Data collection is provided with the NI 9235 USB data collection counter. The positions of the measurements taken for the reference point of the body column are shown in Figure 11a.

Table 2.7 The Comparison of results obtained from the FE and impact hammer tests for the body columns for IGM FR 3500 XL.

Modes	Natural Frequencies obtained by the FEM (Hz)	The results obtained by the Hammer Test and FE analyses			
		Natural Frequency (Hz)	Modal Stiffness (N/m)	Damping Ratio (%)	Receptance of FRF ($\mu\text{m}/\text{N}$)
Rigid Mode	36	28.7	2.9 x 10 ⁹	2.5	0.018
1st Bending Mode	42	42.7	3.9 x 10 ⁹	1.2	0.015
2nd Bending Mode	80	76.9	1.5 x 10 ⁹	4.6	0.0094
3rd Bending Mode	NA	119.6	6.2 x 10 ⁹	1.2	0.0099

Table 7 shows that the natural frequency's vibration mode, which is defined as the 1st Rigid Mode at 28.7 Hz, is in the form of lateral vibration. The first bending mode starts at 42.7 Hz, followed by the second bending mode at 76.9 Hz, and the third bending mode at 119.6 Hz, which were also measured and observed.

The rigid mode from experiments yields the 1st mode from FE analysis. The 2nd bending mode from experiments corresponds to the 2nd mode from FE analysis, and the 2nd bending from experiments is equivalent to the 5th mode from FE analysis according to results obtained by Table 7.

Comparing the dynamic values obtained with the previously produced IGM FR 3500, we observed an increase of around 10% in the body stiffness values. Moreover, when examining the Frequency Response Function values, we found an increase in stiffness, especially in torsion modes. In general, no abnormal dynamic flexibility was found in the machine's body.

ii.) Modal Investigation of the Gantry:

Impact Hammer tests were applied on the gantry, which carries the spindle and Z axis of the 5-axis milling machine, and on which the slides of the Y-axis movement are attached simultaneously (Figure 11b). A PCB 626B03 type accelerometer and PCB 086C05 large-size impact hammer were employed, and 24 points were measured. The positions of the measurement points can be seen in Table 8.

Table 2.8 The Comparison of results obtained from the FE and impact hammer tests for the gantry for IGM FR 3500 XL.

<i>Modes</i>	<i>Natural Frequencies obtained by the FEM (Hz)</i>	<i>The results obtained by the Hammer Test and FE analyses</i>			
		<i>Natural Frequency (Hz)</i>	<i>Modal Stiffness (N/m)</i>	<i>Damping Ratio (%)</i>	<i>Receptance of FRF ($\mu\text{m}/\text{N}$)</i>
<i>Rigid Mode</i>	50	55.7	1.1×10^9	4.8	0.011
<i>1st Bending Mode</i>	79	75.9	1.9×10^9	3.3	0.009
<i>2nd Torsional Mode</i>	NA	125.3	6.9×10^9	2.2	0.004

According to Table 8, it becomes evident that the initial vibration mode, which was measured at 55.7 Hz, pertains to the forward and backward swing of the Y column, and its connection points to the main body. This mode is thought to arise due to the body being in proximity to the 1st bending mode (Table 7), which is one of the primary vibration modes. Additionally, the modal analysis showed that the 1st Bend and 1st Torsion modes were detected at 75.9 Hz and 125.3 Hz, respectively.

Further analysis of the modal data revealed that the stiffness and Frequency Response Function values of the Y column were nearly identical to the dynamic values of the body. Furthermore,

it was observed that the results were quite similar to the measurements taken from the previous machine tool (IGM FR 3500).

The rigid mode from experiments yields the 3rd mode from FE analysis. The 2nd bending mode corresponds to the 4th mode from FE analysis, and the 2nd bending from experiments is equivalent to the 5th mode from FE analysis according to results. From the FE results and experiments, it is observed that the 2nd bending mode of the body columns is close to 1st bending mode of the gantry structure. Therefore, structural optimization is recommended for the gantry structure for natural frequency shifting.

iii.) Modal Investigation of the Z column:

Impact hammer test and modal analysis studies were carried out on the spindle and the column carrying the spindle. These tests used a PCB 353B33 type accelerometer and PCB 086C05 type impact hammer (Fig. 11c). In the measurements, an arbour is attached to the spindle end, and the z-axis is positioned at a distance of 250 mm from the arbour end to the table. Measurements were taken from 17 points in total. All measurements were repeated in directions corresponding to the X and Y axes of the machine.

Table 2.9 The most flexible modes of the Spindle and Z column measured by impact hammer tests for IGM FR 3500 XL.

<i>Modes</i>		<i>The results obtained by the Hammer Tests</i>			
		<i>Natural Frequency (Hz)</i>	<i>Modal Stiffness (N/m)</i>	<i>Damping Ratio (%)</i>	<i>Receptance of FRF ($\mu\text{m/N}$)</i>
<i>XX direction</i>	<i>Rigid Mode</i>	81.6	7.3×10^8	1.73	0.56
	<i>1st Bending Mode</i>	293.6	3.71×10^6	1.03	13.72
<i>YY direction</i>	<i>1st Torsional Mode</i>	273.5	4.35×10^6	1.69	2.32
	<i>1st Bending Mode</i>	333.6	1.12×10^7	2.23	7.69

The impact hammer test and modal analysis results can be seen in Table 9. First, the spindle has natural frequencies close to each other in the tilt mode, which is the most flexible mode in the X and Y directions of the machine. However, its most flexible mode in the Y direction is approximately 50% weaker than its most flexible mode in the X-axis. In other words, the dynamic rigidity of the spindle is somewhat lower in the Y-axis movements of the machine. In addition, there may be cases where chatter vibrations are caused by the spindle in operations where rigid tools and tool holders are used. However, this is not interpreted as a general inference. In such cases (especially considering the most flexible 1st and 2nd modes of the spindle), chatter vibration is likely to occur at speeds of 17500rpm and 20000rpm.

2.7. Topology Optimization

Based on the experimental results, it was found that when the structure size was increased, the main body frequencies shifted to higher modes for IGM FR 3500 XL. However, both the FE results and experiments showed that the 2nd bending mode of the main body was very close to the 1st bending mode of the gantry structure. Thus, to achieve natural frequency shifting, it was recommended to implement structural optimization for the gantry structure.

When it comes to structural optimization, it's important to accurately represent contact interfaces since they are a key factor in the optimization problem. One of the most popular methods for structural optimization is topology optimization, which is commonly used in machine tool research [41]. Topology optimization algorithms are typically divided into two categories: those that search for global structural compliance and those that are limited to local search based on heuristic techniques. Examples of topology optimization algorithms in the first category include SIMP and RAMP, which are used in many FE software programs such as ANSYS, Abaqus, and Hyperworks [42,43]. The second category includes algorithms like BESO and LSTO, which are also found in FE software like ANSYS [44]. LSTO is often used for topology optimization because it incorporates an implicit boundary representation that results in faster analysis than density-based methods. However, density-based techniques are typically used for structural optimization problems with contact constraints, despite their higher computational burden compared to LSTO [39].

2.7.1. Topology Optimization Problem

The topology optimization problem is created using the LSTO algorithm, with the objective function being to minimize compliance. The design domain chosen for this problem is the gantry structure, with the contacting surfaces excluded to keep the contact boundary forces constant. To ensure optimal results, three different constraints are set. The first constraint aims to reduce the mass by 50%, while the second constraint focuses on minimizing displacement values with an extra cutting condition. The third constraint involves mode shifting for at least 10%. The material used in this problem is the Titanium Ti6Al4V alloy, with the cutting conditions specified in [29]. The axial depth of the cut is 20mm, and the feed rate is 0.050mm/tooth. The cutting forces are obtained via CutPro software.

2.7.2. Topology Optimization Results

As we can see in Figure 12, the topologically optimized structure has been successfully achieved while reducing the mass by 50%. Figures 12a and 12b show the optimized gantry structure, while Figure 12c displays the initial design. All the given constraints have been met, making this a great accomplishment.

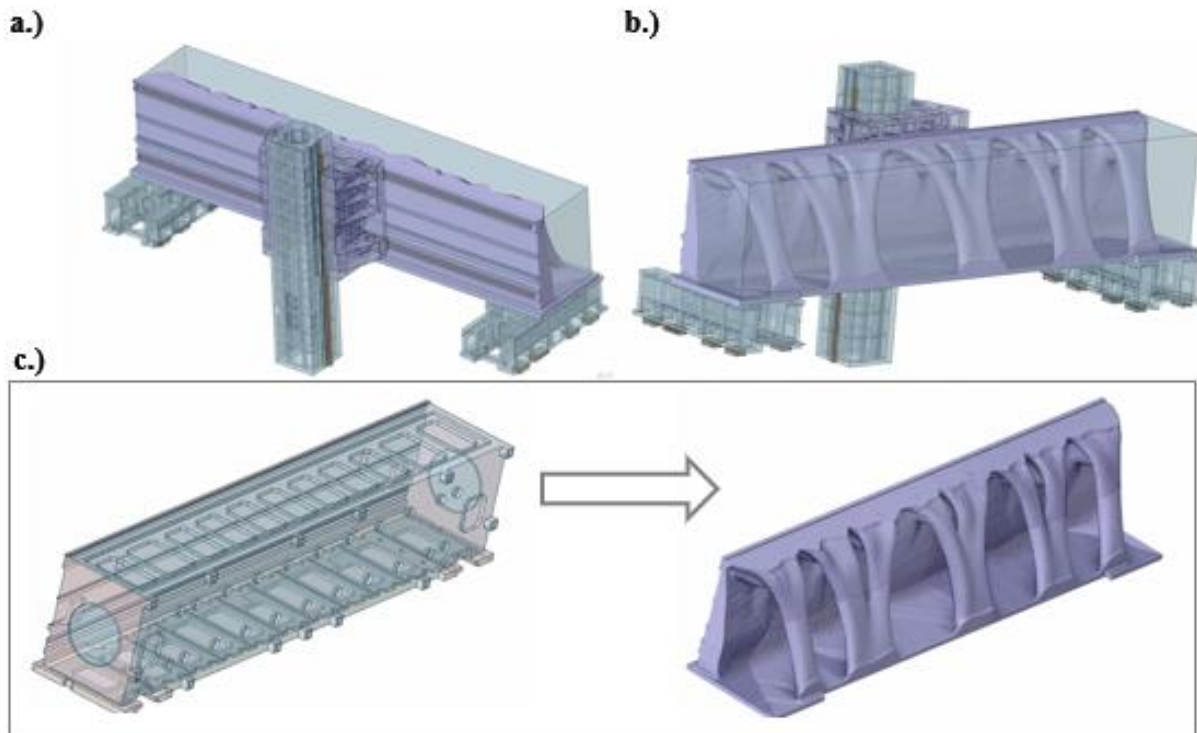


Fig. 2.12 a.) Front view of the optimized design, b.) Rear view of the optimized design c.) Initial and optimized design.

2.7.3. Modal Analysis Results

Here is Fig. 13, which shows the natural frequencies and mode shapes of the topologically optimized structure. The initial design of the gantry had natural frequencies of approximately 56 Hz, 76 Hz, and 125.3 Hz for the first three modes. However, these frequencies have been successfully shifted to approximately 132 Hz, 145 Hz, and 191 Hz.

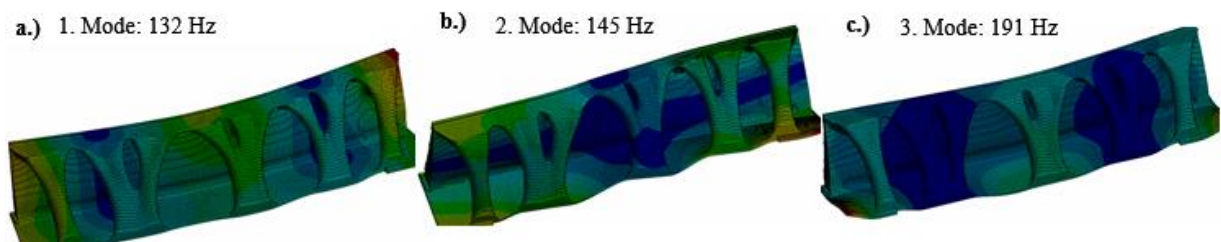


Fig. 2.13 a.) 1st Mode: 132 Hz, b.) 2nd Mode:145 Hz c.) 3rd Mode: 191Hz for the optimized gantry

A gantry-type machine tool with super-large sizes is analyzed and structurally optimized. The significance of cast components to enable structural rigidity during the manufacturing of these massive structures is highlighted via modal FE analyses and experiments. The effectiveness of the proposed optimization problem and method using the LSTO algorithm was evaluated by modal FE analysis.

2.8.Large-Scale Horizontal Milling Machine

2.8.1. FE Analyses

The original CAD data of the IGYF-150 horizontal milling machine is given below. The machine tool is structurally composed of two independent units. For this reason, all the analyzes were performed separately for two independent units. All parts of the design model need not be included in the initial calculations. For this reason, non-critical fasteners and spindle parts are not included in the structural analysis to reduce the computational load. In addition, all unnecessary holes in the analysis are closed and non-critical geometries are simplified to improve mesh quality. The initial and meshed versions of the CAD model are shown in Fig. 14.

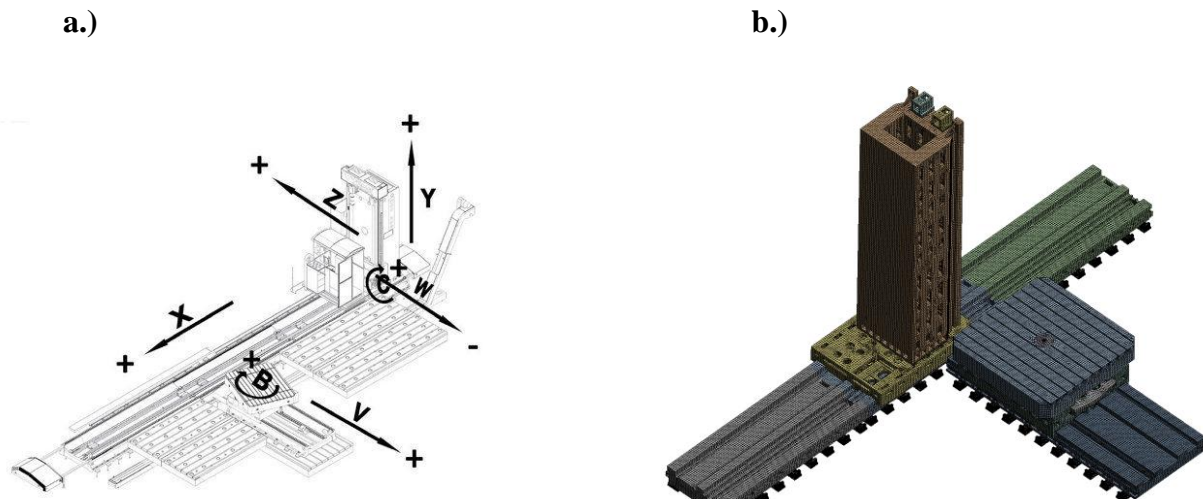


Fig. 2.14 a.) Original CAD Model b.) Simplified CAD Model for FE.

Brick mesh elements are used extensively in regions without thin walls. The quality of brick meshes was checked by looking at the Jacobian and skew ratios. In the assembly, the mesh dimensions for each part are adjusted by giving dimensions. The total number of meshes used for the simulation of the assembly of the spindle bearing tower is 957,097 and the number of elements is 252,888. A total of 1932 contact zones were determined. As stated, mechanical interface modeling in an FE environment is critical for large-scale machine tools. The penalty algorithm (which exists in nearly every FE software) and RCFM will be employed together for mechanical interface modeling in FE for large-scale milling machines. The pure penalty algorithm (prone to assign higher contact stiffness values) is employed with 0.2 relaxation tolerance on contact interfaces in the FE model.

2.8.2. Body Analyses

2.8.2.1. Deflection Analysis

Since IGYF-150 is very large in terms of dimensions, simulations were first made to calculate the amount of deflection of the machine tool under its weight to understand the behavior and weak points of the machine tool assembly.

i.) Tower Deflection Analysis

In this part of the study, the results of the deflection analysis that occurs when the Y-column (Tower part) has its weight (approximately 59.7 tons) are investigated. The electric motors and spindle assembly in the Y-column (Tower part) have been removed from the machine model to facilitate analysis. For this reason, the deflection on the Y-column (Tower part) and the tower guideways connected to the tower part will be slightly more than the simulation in reality. The analyzes were run in ANSYS. In this analysis, only the force is due to gravity, and no additional force is applied. The gravitational force is given in the -Y direction. The position where the machine tool can be the most flexible was selected to see the maximum deflection in the analysis.

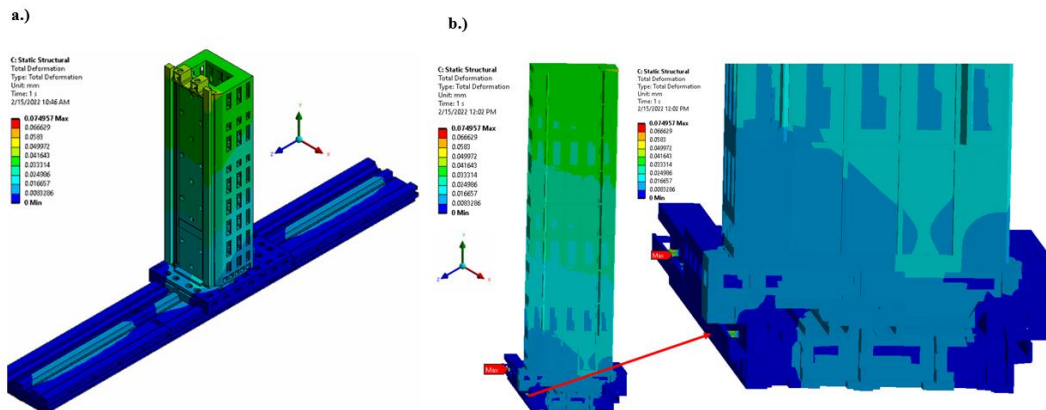


Fig. 2.15 a.) Deformation of the bench under its weight, b.) Local Deformation (Total)

In Fig. 15, the analysis result is given as the total deformation. The maximum total deflection was observed in the tower guideways at the bottom. The tower guideway system slides are not symmetrical. This causes high local deformation on the short side of the slide (Fig. 3b). The local deformation amount is approximately 74 μm . Apart from that, looking at the general results, the highest total deflection was observed as approximately 66 μm in the base foot of the tower guideway that carries the Y-column (Tower part). It is not much for a machine tool of this size, but it should be considered that this value can increase with the weight of the workpiece, spindle, and operating cabin.

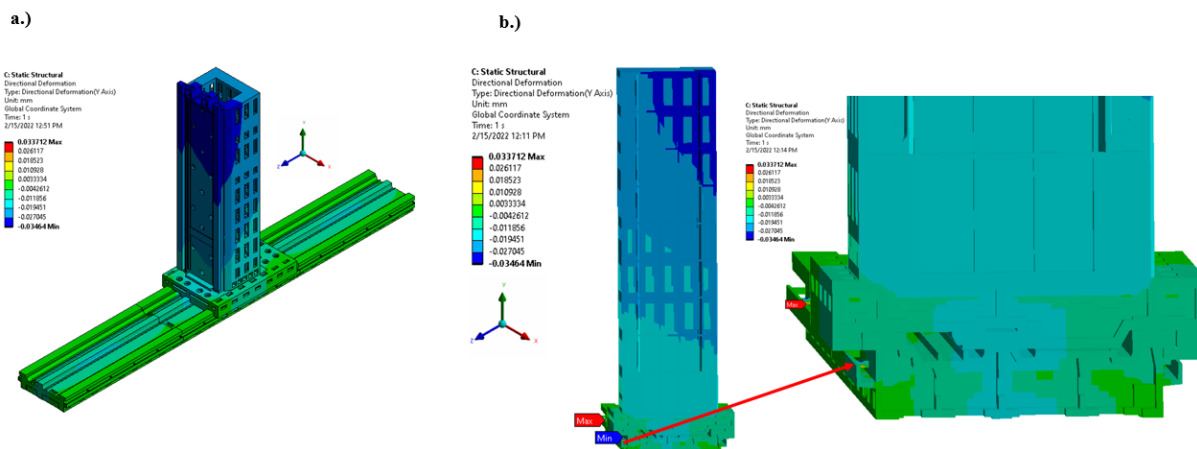


Fig. 2.16 a) Y-direction deformation of machine under its weight, b.) Local deformation (Y-direction).

The collapse of the bench in the Y direction due to its weight is shared in Fig. 16. Similar to the total deflection result, the maximum values were observed in the local deformation region shown in Fig. 16 b. The deformation values here are approximately 34 μm .

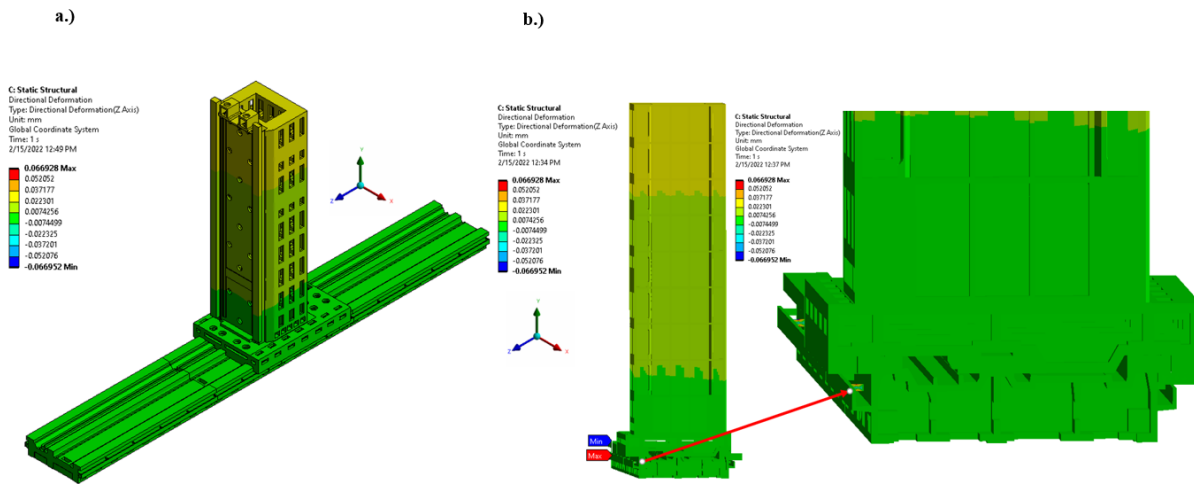


Fig. 2.17 a) Z-direction deformation of machine under its weight, b.) Local deformation (Z-direction)

The deflection of the machine tool in the Z direction due to its weight is shared in Fig. 17. The deflection in the Z direction is approximately 67 μm . At the top of the Y-column (Tower part), approximately 37 μm deflection was observed.

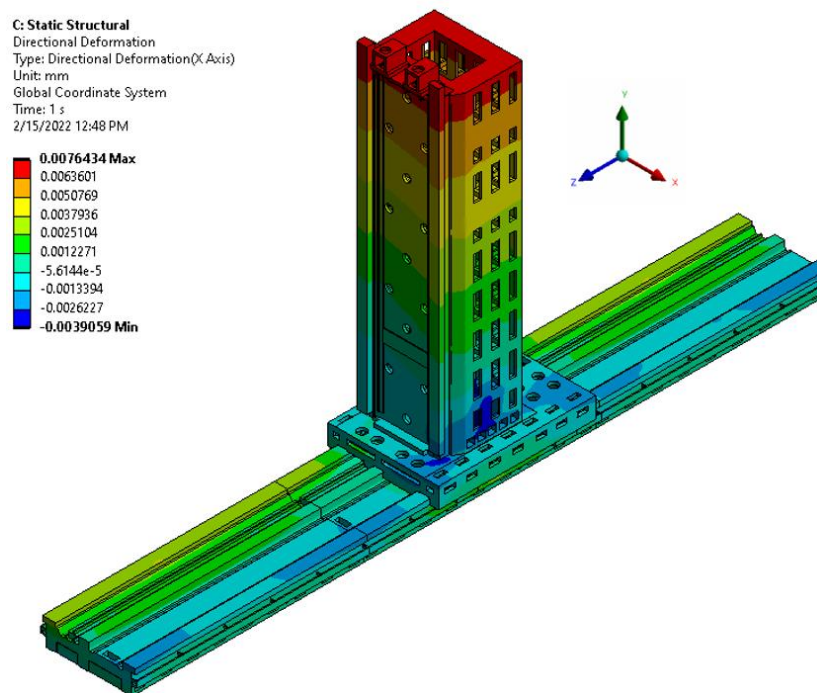


Fig. 2.18 X-direction deformation of machine under its weight

The X-direction deflection of the machine due to its weight is concentrated in the area above the 7 μm spindle carrier tower. In addition, the results of equivalent stress, equivalent total

strain, and shear stress for the YZ axis according to the Von-Mises criterion are also shared in Fig. 19.

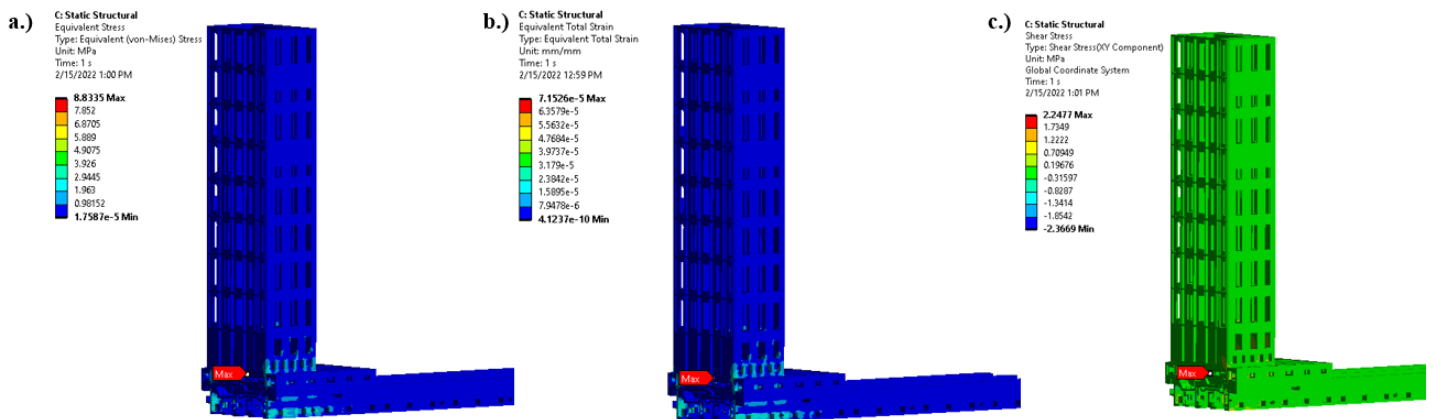


Fig. 2.19 a) Equivalent Stress under its weight, b.) Equivalent Strain, c.) Shear Stress for YZ Axis.

The stress and strain values due to the machine's weight were observed as a maximum when the Y-column (Tower part) met the tower guideway. This is an expected situation since the highest load comes to this portion. Again, the regions with the highest strain energy are in this part. Closing the holes at the bottom of the Y-column (Tower part) is a structure-strengthening suggestion. The strain energy distribution in these regions is shared in Fig. 20.

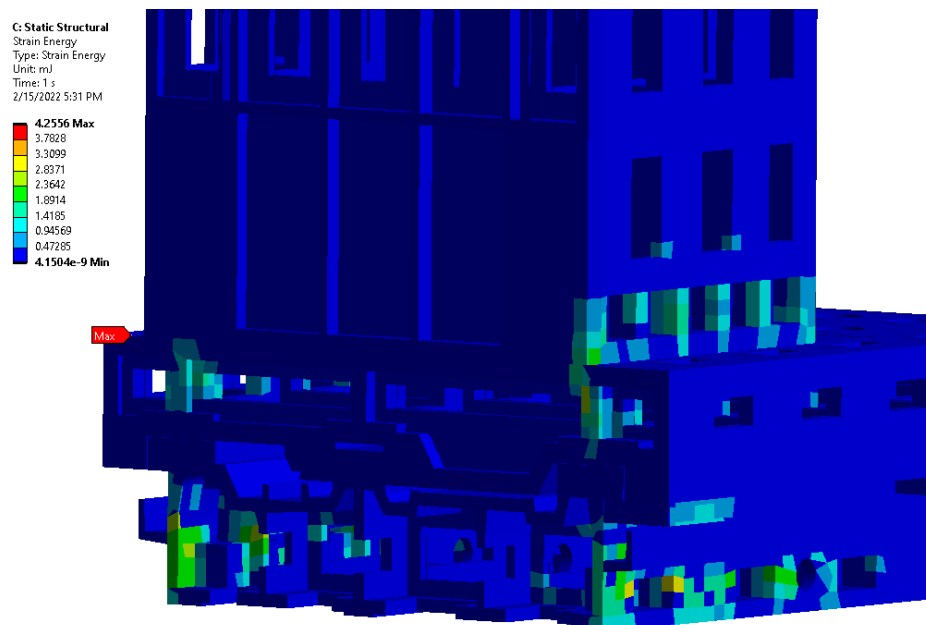


Fig. 2.20 Stain energy distribution under the machine weight.

ii.) *Worktable Deflection Analysis*

To see the maximum deflection in the analysis, the position where the machine can be flexible at the highest level was selected. Loads from the parts' gravitational force were inputted in the analyses. In Fig. 21, the analysis result is given as the total deformation. In Fig. 22, the

maximum deformation results based on direction are given. The analyses were run in ANSYS, and the results for the worktable of the IGYF-150 are separate from the tower part. The maximum deflection was observed in the rail system at the bottom. This situation is expected from a structural point of view. While the worktable weight is directed to the rails, the support elements at the bottom also support these regions. In this case, the middle part of the rail system (red part in Fig. 3) is the part where the most deflection is observed.

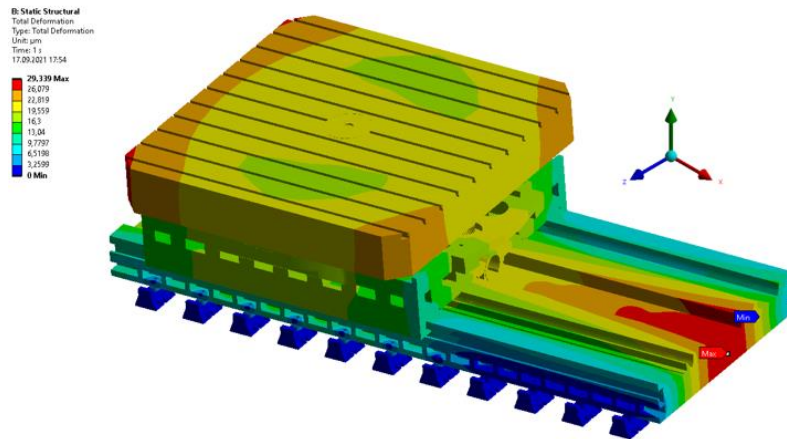


Fig. 2.21 Deformation of the worktable under its weight

In this analysis, only the force is due to gravity, and no additional force is applied. The force of gravity is given in the - Y direction. The calculated maximum slump is around 29 µm. It is not too much for a machine of this size, but it should be considered that this value may increase with the weight of the workpiece.

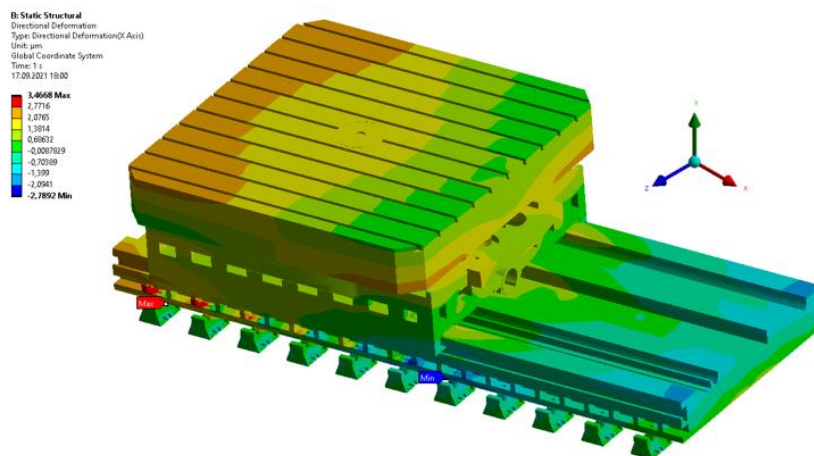


Fig. 2.22 X-direction deformation of the machine under its weight

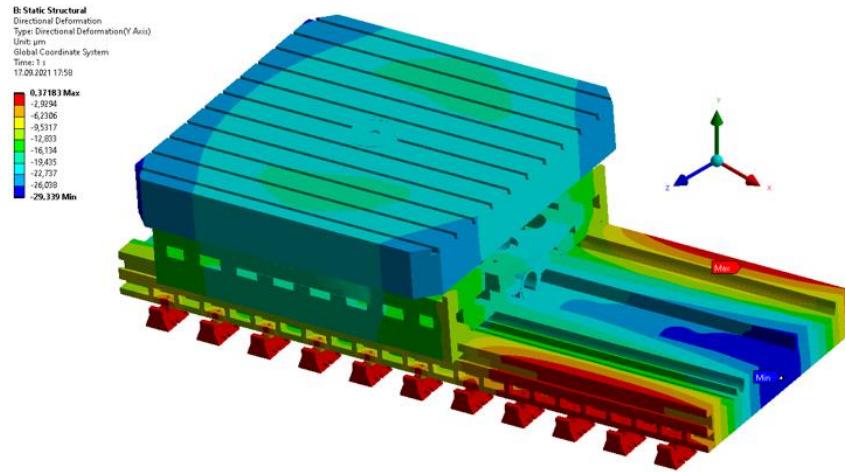


Fig. 2.23 Y-direction deformation of the machine under its weight

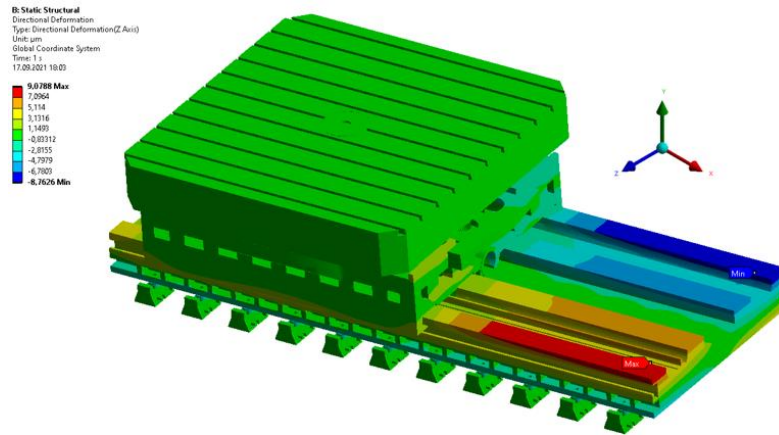


Fig. 2.24 Z-direction deformation of the machine under its weight

The deflection of the worktable in the X direction due to its weight is around 3.4 μm, and the assembly deflection is concentrated in the area where the foundation block is. The collapse of the bench in the Y-direction (at the same time, the direction of the gravitational force) due to its weight is around 29 μm, and the maximum deflection was observed in the rail system at the bottom. The fact that the maximum deflection appears in blue in the Y direction is that the deflection occurs in the opposite direction to the positive direction. Observation of the maximum deflection in the middle is expected due to the support of the ends of the foundation supports on both sides. The deflection in the Z axis was observed on the rails where the worktable contacted the rail system. It is approximately 9μm in both directions. Structurally, this deflection is an expected result.

2.8.2.2. Modal Analysis

A modal analysis was performed to contribute to the design process of the IGYF-150 horizontal milling machine, and the first six modes were found. Again, similar to static analysis, two different simulations were made for the analysis. The Y-column (Tower) analysis was completed in the first part, and the worktable analyses were made in the second part. The modes between 5 and 1000 Hz were scanned in two simulations by being supported from the machine tool base. The mode values obtained from the analysis results are given in Table 10. The modes of the IGYF-150 in the Y-column (Tower part) were generally found in the 14-88 Hz range.

For the independent section where the worktable of the IGYF-150 is located, it is in the range of 23 -129 Hz. The mode values of the worktable are also given in Table 10.

Table 2.10 Modal Analysis Results

<i>Modes</i>	<i>Tower Modes</i>	<i>Worktable Modes</i>
<i>1st. Mode</i>	14.9 Hz	23 Hz
<i>2nd. Mode</i>	16.9 Hz	80 Hz
<i>3rd. Mode</i>	48.4 Hz	106.6 Hz
<i>4th. Mode</i>	74.4 Hz	114.8 Hz
<i>5th. Mode</i>	78 Hz	126.7 Hz
<i>6th. Mode</i>	88.1 Hz	128.2 Hz

i.) Tower Modal Analysis

The first three modes of the Y-column (Tower part) are given in Fig.23. All modes are observed in the column. The first mode consists of bending the column forward and backward, and the frequency value is about 15 Hz. On the other hand, the second mode consists of bending the column structure to the right and left, and its frequency is approximately 17 Hz. The fact that the mode values are at these low values is expected since the structure is quite large and mainly consists of cast iron. However, this may cause problems while the spindle is working. These frequencies create the risk of resonance when the machine is working at 900 -1020 rpm. In addition, elements such as the operator cabin, spindle, and electric motors are not included in the FE analysis. Adding these to the actual operating condition will increase the system's weight, and hence the natural frequencies will be further reduced. In this case, resonances can also be experienced at speeds lower than 900 rpm. The third mode value is 48.4 Hz, which is the torsion mode of the column, and such torsion modes may pose a risk to the structure. Since this section includes the spindle, an interaction around 48 Hz can directly affect the processing quality. Again, this value corresponds to approximately 2094 rpm for the spindle. In addition, frequencies between 40-60 Hz are frequently observed in some electric motors (for example, the first mode for Siemens 1FT6086-8AF7x is 44.8 Hz). Care should be taken to avoid any conflicts around this mode.

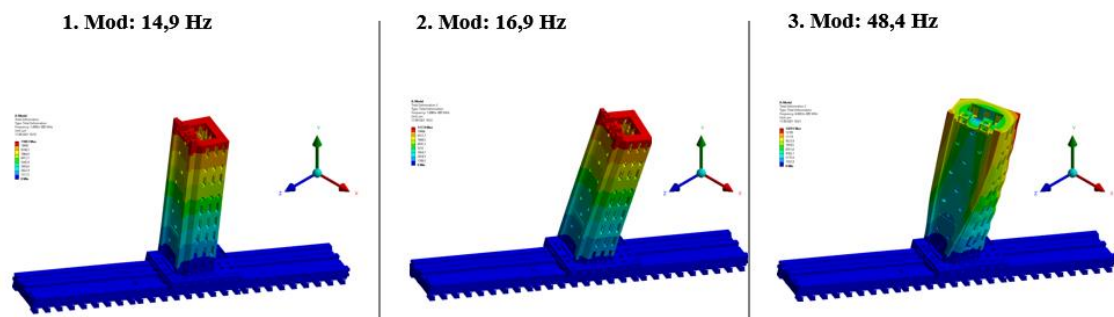


Fig. 2.25 Tower part a.) 1st Mode:14.9 Hz , b.) 2nd Mode: 16.9 Hz, c.) 3rd Mode: 48.4 Hz

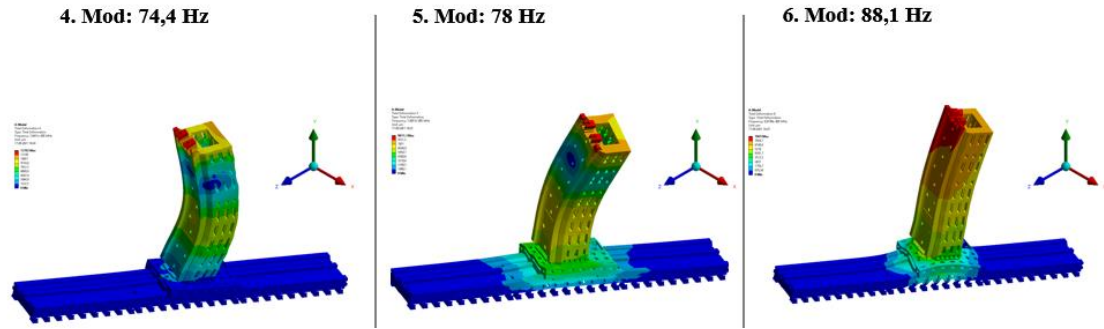


Fig. 2.26 Tower part a.) 4th Mode: 74.4 Hz , b.) 5th Mode: 78Hz, c.) 6th Mode: 88.1 Hz

The last three modes of the Y-column (Tower part) are given in Fig.24. The 4th mode is 74.4 Hz, and it bends back and forth to be a sine wave. This modal behavior is expected as the structure resembles a straight beam structure but can be important for machining quality as the spindle will be attached to this section. The 5th mode is 78 Hz and bends to the right and left as a sine wave. Finally, the 6th mode moves up and down in the vertical direction and is calculated as 88 Hz.

ii.) *Worktable Modal Analysis*

The first three modes of the independent section where the worktable is located are given in Fig. 25. The first mode in this section is 23 Hz, which includes the worktable flexing forwards and backward. The second mode is around 80 Hz, and the mode shape consists of the worktable stretching to the right in the left-hand direction. This mode is very close to the 5th mode of the tower part, and similar modes should be avoided. The third mode is calculated as approximately 107 Hz and is the torsion mode of the worktable. Torsion modes are structurally undesirable, and care must be taken when designing. Bending, pressing, and pulling movements are more acceptable for the structure.

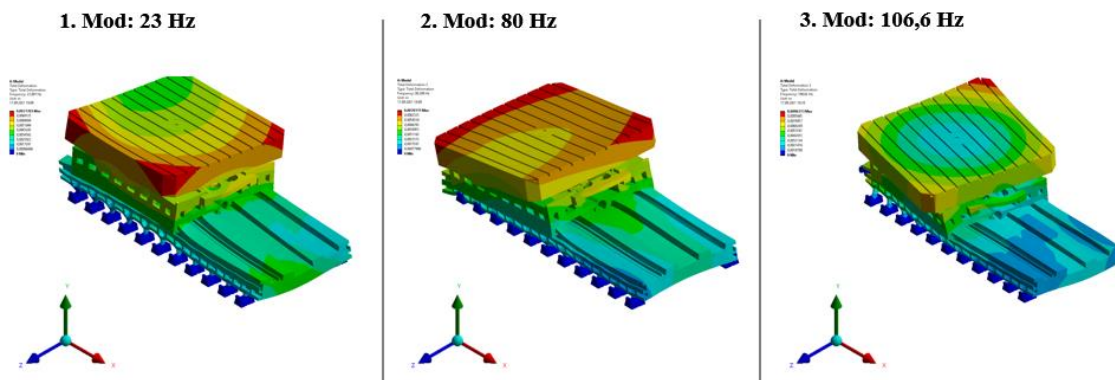


Fig. 2.27 Worktable part a.) 1st Mode: 23 Hz , b.) 2nd Mode: 80 Hz, c.) 3rd Mode: 106.6 Hz

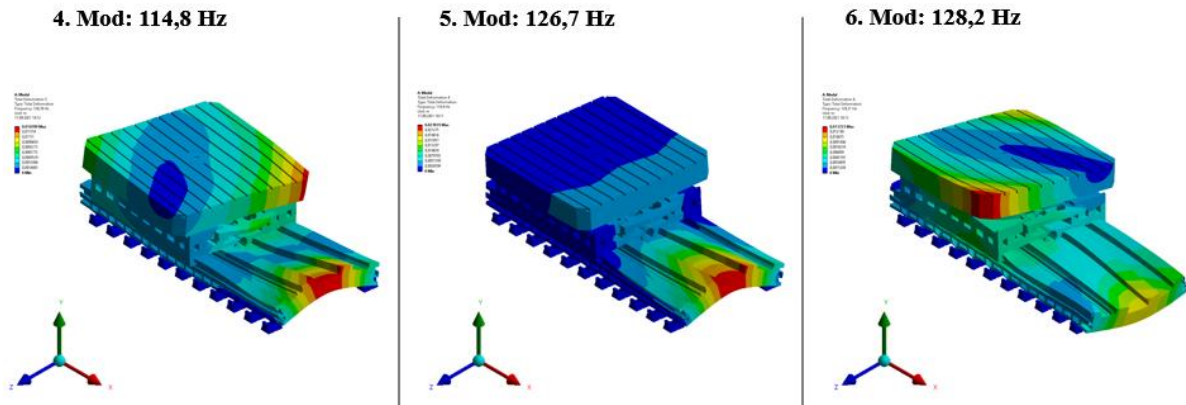


Fig. 2.28 Worktable part a.) 4th . Mode: 114.8 Hz , b.) 5th Mode: 126.7 Hz, c.) 6th Mode: 128.2 Hz

The last three modes of the independent section where the worktable is located are given in Fig. 26. The 4th mode of the system is 114.8 Hz, and the mode shape is predominantly observed in the rail carrier system below. It consists of the forward-backward stretching movement of the carrier system. The 5th mode of the system is 126.7 Hz, consisting of the rail carrier system flexing to the right and left. Finally, the 6th mode is 128.2 Hz, and the flexing movement of the rail carrier system and the worktable from the corners form the mode shape.

2.9. Topology Optimization

While creating the optimization problem, the boundary conditions are as follows: the tower part is supported from the bottom, and the point loads are placed in the system to create the maximum moment with a safety factor of 50% to represent the weight the spindle will create. A deflection constraint is applied to the optimized structure to limit the total maximum deformation at the tower part to 100 μm . In addition, another applied optimization condition is to reduce the mass by 45%. Finally, two target functions are given for optimization purposes. The first optimization goal is to produce the structure with minimum compliance (flexibility). The second goal is to maximize the first structural mode. Since the multi-objective optimization target was set simultaneously, the targets were weighted as 70% to 30%. There are several reasons why the second target might be set to a lesser value. First, since the structure is enormous, the mode value will increase due to mass decrease and increase in structural stiffness value due to the minimum compliance target. However, due to the gigantic dimensions of the structure, the first mode in the system (14.9 Hz) will not be possible to very advanced (such as 25 Hz) frequencies. Secondly, filters in this static optimization are much safer than dynamic optimization filters. The first mode of the worktable section, which is already much lighter, comes around 23 Hz. Finally, SIMP algorithms are prone to generate pseudo-mode due to the inadequacy of their filters in dynamic structural optimization. Optimization results for the tower part are shared in Fig.27.

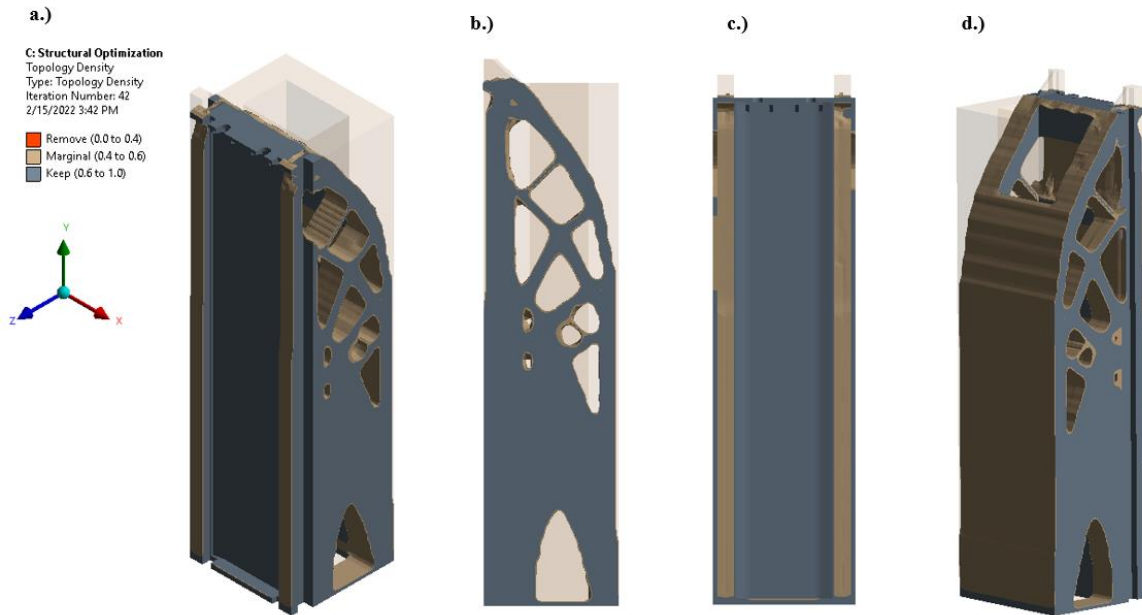


Fig. 2.29 Topology optimization a.) Isometric from the Front b.) Isometric from the left c.) From the front, d.) Isometric from the back.

According to the topology optimization results, the material was primarily removed from the upper rear part of the tower. Again, holes were opened in the upper parts to form cross beams. Such an optimized structure is similar to the optimization results of similar prismatic structures in the literature [45]. Another important observation is in the foot parts where the tower part is supported. According to the static analysis results, the stress and strain energy values were higher in these parts where this part walks on the rail than in other regions. The rectangular holes in the first design increased the regional stresses in these regions. Still, the regional stresses were minimized by making a sizeable arc-shaped unloading in these regions in an optimized way. Likewise, by increasing the amount of material from the upper part and keeping the material in the lower part constant, the center of gravity of the system was kept close to the carrier rail system, thereby facilitating the acceleration of the tower by creating less inertia and rotational moment in motion.

Table 2.11 Modal Analysis Results for Optimized Spindle Support Tower

<i>Modes</i>	<i>Initial Tower Modes</i>	<i>Optimized Tower Modes</i>
<i>1st. Mode</i>	14,9 Hz	17 Hz
<i>2nd. Mode</i>	16,9 Hz	21 Hz
<i>3rd. Mode</i>	48,4 Hz	50 Hz
<i>4th. Mode</i>	74,4 Hz	81,7 Hz
<i>5th. Mode</i>	78 Hz	80 Hz
<i>6th. Mode</i>	88,1 Hz	92 Hz

As a result of the topology optimization, the mass has been reduced by 45%, and the structural modes have been moved to further frequencies for spindle and tower assembly. Initial and

shifted modes are shared in Table 11. The optimized mode shapes are similar to the old ones, but the torsion mode in the 3rd Mode is blocked in the new optimized structure. Instead, a mode shape in the form of a sine wave is observed.

2.10. Critical Points and Conclusions

In this study, improvement processes of two different large-scale machine tool structures are presented. The critical points are determined based on the deflection and modal analyses presented. The machine tool contact interfaces the FE models used the penalty contact at the insignificant areas and the RCFM at structurally essential areas. The FE simulations are verified on the manufactured prototypes. The first presented example is a large-scale 5-axis gantry-type milling machine comparison that shares similar X and Z axes with different Y-axis sizes; the small one is 70 tones, while the more extensive is 120 tones. The second example is a horizontal milling machine composed of two independent subassemblies. The first part comprises a horizontal tower and a guideway for movement. This tower carries approximately 5.5 tons of weight due to the spindle and operation cabin. The tower itself is 23.6 tons, while the guideway is 59.7 tons. The second part comprises a worktable and railway system weighing around 15 tons. The specific observations from a comparison of large-scale 5-axis gantry-type milling machines are as follows:

- The natural frequencies of the primary dynamic modes of the body are close for IGM FR 3500 and IGM FR 3500 XL. This shows the consistency of the body manufacture in terms of repeatability.
- Compared to the IGM FR 3500 (70 tons), it has been observed that the rigidity of the IGM FR 3500 XL (120 tons) has increased by around 10%. The reason for this is the improvements made in the design.
- The dynamic behavior of the Y-axis column of the IGM FR 3500 XL is like that of the IGM FR 3500.
- The main body and gantry values are close to each other in terms of dynamic rigidity for IGM FR 3500 XL.
- It is suggested that topology optimization on the gantry for the IGM FR 3500 XL. In this way, dynamic rigidities will increase even more.

The specific observations from a comparison of large-scale horizontal milling machines are as follows:

- No significant structural problem has been encountered in the static analysis performed for the tower part. However, the distances of the slides on which the spindle carrier tower moves are not equal. Therefore, local deformation and stress zones were observed in the short-distance regions. These high deformation zones can be formed by increasing the wall thickness, or triangular ribs can be laid to reduce the local deformation.
- As a result of static analysis, stress local stress concentrations were observed in the feet of the tower and the structure connecting the tower with the guideways. Although the amount of stress in these regions is not critical, structural measures can be taken to improve the design.
- In the modal analysis, the modes of the spindle carrier tower were low due to the enormous structure, and the first mode value is expected to be lower than 15 Hz, as it will increase the mass of the system in elements such as the spindle, electric motor, operator cabin. Due to the low frequencies of the tower structure, the fact that the 3rd Mode is an open torsion

mode, and the dominant mode shapes are observed on this structure. It was suggested to be strengthened by adding cross-column-beam elements or the like or by subjecting it to topology optimization. Again, a structural optimization study was proposed to reduce the tower and to accelerate it more quickly due to its mobility.

- According to the topology optimization results, the optimization algorithm material has mainly been removed from the upper rear part of the tower. Likewise, by increasing the amount of unloading from the upper part and keeping the amount of material in the lower part constant, the center of gravity of the system was kept as close to the rail system as possible, thereby facilitating the acceleration of the tower by creating less inertia and rotational moment in motion.
- As a result of the topology optimization, the structural modes have been moved to approximately 13% forward frequencies for the tower assembly; for an optimized tower assembly, this means a 120-rpm shift between the spindle frequency and the structural frequency. (In this case, the danger of resonance may be experienced when the spindle is rotating at 1020 rpm, not at 900 rpm.) An ideal design would be made if this frequency value could be increased above the maximum speed of the spindle at 3000 rpm (25 Hz). However, this may require removing too much mass in structural optimization. For example, the first Mode of worktable with the much lighter assembly comes in around 23 Hz.
- Structural optimization's most significant achievement in dynamics has been to remove the torsion mode seen in Mode 3. While the Mode of the structure was moved from 48 Hz to 50 Hz, the mode shape changed from torsion to a bending-based shape.

The general conclusions from the FE simulations and experiments are shared below:

- The RCFM has proved its reliability for large-scale machine tools.
- The deflection and modal analysis results help to reveal the weakest points in a machine tool which are generally located near the mechanical interfaces that transmit and deliver the loads.
- Regarding stiffness and mass distribution to extend the machine sizes, careful planning and implementation are only possible with proper mechanical interface modeling.
- The weight deflection ranges are more significant than the regular-sized machine tool structures, while frequency ranges are lower than the regular-size machine tools.
- Monoblock main bodies and bases are reliable and have fewer static and dynamic behavior problems.
- The connection between the significant components- to extend machine size- determines the assembly stiffness and careful stiffness planning is required, as in the case of IGM FR 3500 XL. This means that more extensive components only sometimes result in a stiffer structure.
- Generally, large-scale machine tools are used for heavy-duty machining. Therefore, the accompanying spindles on these machines are high torque low-speed spindles. The operating frequencies of these spindles can overlap with structural frequencies, such as the situation that was possible for the horizontal milling machine. Therefore, structural optimization (topology optimization) is offered in such a situation since these machines are stiff enough.
- Another observation is that significant components can have close frequencies and similar modes, which can cause resonance during operation; again, for such a situation, structural

(topology) optimization is offered, as in the case of IGM FR 3500 XL. The extension of the RCFM method for Level-Set Topology Optimization (LSTO) is also exemplified during the topology optimization IGM FR 3500 XL.

- Lighter components bring physical capacity improvement and energy efficiency chance to machine tool axes, and large-scale components always have more room for this opportunity compared to smaller machine tools.

3. CONCEPTUAL DESIGN OF A HIGH-SPEED SPINDLE

3.1. Summary and Novelty

High-speed spindle design is challenging even for leading spindle producers since extreme speeds push all limits. The research and development process of high-speed spindles is based primarily on field and hands-on experience since the theoretical models become highly nonlinear and convoluted to study, bringing the additional cost to manufacturers. Since these spindles are complex but a must for cutting-edge products, these spindles are expensive and highly commercialized. Therefore, finding detailed technical details is hard, and design guidelines are not well-established in the literature. In this study, developing specifications, strategies and design layouts of a 40 000-rpm spindle are presented in detail. The presented spindle will be optimized and manufactured in the laboratory.

3.2. Introduction

High-speed spindle design is a complex task affected by many parameters, and there needs to be well-established literature since these machines are highly commercialized. The optimization of high-speed spindles requires careful selection and planning of cutting parameters, motor specifications, bearing, shaft design, cooling system, etc., together with predictive digital twins. The accuracy of these digital twins depends on the modeling details and iterations between the changing parameters, which affect each other. Another problem with spindle digital twins for design purposes is the automatization of parameters for design changes. Generally, one geometric change affects the entire structure, meaning a significant difference in the design and boundary conditions of digital models. To be able to create an automatized and parameterized spindle design platform, optimization parameters should be carefully selected, which in turn affects the entire design. Thus, establishing the links between the optimization parameters and the other structural parameters is essential. These relationships generally depend on the experience of spindle producers, and in the machine tool literature, only a few papers focus on this relationship [46-53]. In this study, a 40 000-rpm spindle aimed to be optimized and manufactured. To achieve this first conceptual design of the spindle, is presented by elaborating design strategies and design layouts. During the detailed design studies, different high-speed spindles are examined and simulated [49,51]. It is realized that the following issues are critical and require a lot of iteration between the parameters, making the given task challenging. The crucial ten tasks are as the following to initiate a conceptual spindle design.

1. Begin spindle design by selecting the tool holder and collet, and this will determine the maximum tool diameter and cutting demands.
2. Select the motor parameters: maximum/nominal speed and torque will be the leading parameters for shaft size/length and bearing selection.
3. Select the most challenging material condition the spindle can cut and determine the maximum cutting loads.
4. Determine the possible smallest bearing sizes and shaft dimensions from the maximum cutting loads.
5. After determining bearing size, check the maximum shaft length for twice the full spindle speed by considering critical speeds.
6. Select a drawbar for the specified spindle speed.

7. Select the bearing arrangement and lubrication type.
8. Determine the preload mechanisms for front and rear bearings.
9. Consider the lubrication system for bearings, electrical motors, and other machine elements (inputs and outputs).
10. Decide the bearing/ electrical motor cooling system on the housing.

The critical ten tasks are divided into two halves to ease the optimization studies. In the first part, the first five tasks are optimized. In the second part, the last five tasks are optimized. After determining bearing size, location, and minimum and maximum shaft ranges, the spindle design is launched.

The practical design concerns faced during the optimization and design process are mentioned in the following:

- The front bearings should be near the tooltip for better dynamic behavior. Thus, we must use the shortest compact sealing elements to set the shortest range for the front bearing from the spindle tip. Rigid preload is the application from the outer rings of front bearings, enabling the shortest distance.
- Constant preload should be applied to rear bearings to compensate for thermal growth.
- We first set similar radiuses for bearings and electric motors to ease cooling system manufacturing. However, FE analyses revealed that the thermal gradient exponentially increases when bearings and motors have similar radial dimensions. Therefore, employing smaller and radially shorter bearings with radially taller motor sizes eases heat dissipation. We observed that most high-speed bearing manufacturers have sectional local cooling systems instead of central ones.
- The shaft cooling system depends on the rear bearing size since the wall thickness is reduced with smaller bearing sizes.
- Since this is a high-speed spindle, smaller bearing and spindle component sizes are better for thermal management and dynamic balancing.
- Smaller component sizes cause complicated and hard to design and produce lubrication systems since:
 - We cannot use grease-based lubricants for high speeds. The air-oil system can be the most primitive system that we can employ. Using an air-oil system requires the design of nozzles and drainage chambers for spacers.
 - Labyrinth bearings and flinger/slingers must be employed to avoid leakage, and this system must have self-lubrication nozzles and drainage systems.
 - To compensate for possible thermal growth, a constant preload system at the rear bearings causes the design of sliding/mobile machine elements that share an interface with the outer rings of the rear bearings. Thus, the lubrication system of the rear bearings required additional care. The safest solution was to design lubrication channels on sliding/mobile machine elements to avoid component leakage.

3.3.Research Gap

Designing a high-speed spindle can be a challenging task, given the limited availability of design details since high-speed spindles are highly commercialized and design details are hard to reach . However, this study has presented a conceptual design for a high-speed spindle, along with technical information and strategies for manufacturing. The study also provides a step-by-step guide for designing and laying out a high-speed spindle, which can help optimize the

spindle's structure. Additionally, the study addresses practical design concerns related to high-speed spindles and outlines design parameters for optimization. Overall, this study is a valuable resource for anyone looking to design an effective high-speed spindle.

3.4.Fundamental Spindle Components

As listed in the introduction, spindle design should begin with selecting a tool holder and a collect size together with motor specifications, determining the drawbar size and cutting conditions. The drawbar size also depends on the shaft length, associated with maximum spindle speeds (critical speed constraints the maximum shaft length). The collect size defines the maximum tool size. The maximum tool size and spindle motor torque determine the maximum cutting conditions, allowing us to calculate cutting and magnetic forces due to the built-in electric motor. Predicting these forces helps us determine the minimum bearing sizes and spindle shaft dimensions. One can draft a spindle shaft after selecting and choosing these fundamental components. Therefore, the conceptualization of a high-speed spindle begins with the selection of the following parts:

Tool Holder and Collect Selection

When it comes to tool holders, there are two main categories: ones with steep tapers (like ISO, BT, and CAT) and ones with hollow cup tapers (like HSK). The BT and HSK types are often used with high-speed spindles. In HSK tool holders, the drawbar fingers are located inside the shank, while in BT tool holders, they wrap around the retention knob's exterior surface as it holds the tool holder in place in the spindle. However, with the increase in machining spindle speeds, steep tapers rotary tool holders like BT and CAT systems tend to lose accuracy due to higher centrifugal force when running at high RPMs. As a result, the HSK 25 E tool holder was selected and collected to reach 40,000 RPM. The maximum tool diameter for the selected holder and the collect is 13 mm.

Motor Selection

Through this research, it is discovered that to achieve high-speed spindles, electro-spindles with built-in electric motors are necessary. These electric motors are typically of the PM type and can either be IPM or SPM. The IPM type, specifically, is a type of motor that has a rotor embedded with permanent magnets. This design reduces the risk of a magnet being peeled off by centrifugal force and takes advantage of reluctance torque. Thus, it was determined that the IPM-type electric motor was the best choice to mitigate magnetic forces caused by the motor during spindle operation. The selected electric motor boasts impressive specifications, including a maximum speed of 40000 rpm, a torque of 3Nm, and a 540 V DC bus voltage.

Determination of Maximum Cutting Parameters

After determining the appropriate size of the cutting tools and the motor specifications, it is feasible to predict the magnitude of the cutting forces that will be exerted during a worst-case cutting scenario.

Bearing Selection

When designing a spindle, angular contact ball bearings are typically used for ultra-high-speed applications. These precision bearings allow for maximum speeds with floating bearing

configurations. Selecting the right bearings for a spindle design requires multiple iterations to ensure the best choice. For a spindle with a small tool holder and tool, a grinder-type spindle arrangement consisting of two tandem bearings at the ‘O’ configuration is often chosen. This arrangement ensures that the cutting and magnetic forces are applied to a beam with predetermined boundaries for the bearing locations. To determine the minimum bearing sizes, deflection and moment analysis from the bearing manufacturer catalogs were used. The analysis showed that the minimum front bearing size should be 40 mm, while the rear bearing should be 30 mm.

Drawbar Selection

When it comes to selecting a drawbar, there are a few crucial factors that need to be considered. Firstly, you will need to consider the tool holder and spindle speed, as these elements will determine the type and diameter of the drawbar that will be suitable for your specific needs. Additionally, it's important to make sure that you adjust the height of the drawbar based on the length of the spindle shaft in order to ensure optimal performance. The diameter of the drawbar will also be a key factor to consider, as it will define the inner profile of the spindle shaft. Finally, for ultra-high-speed spindles, it is highly recommended that you choose fully automatic drawbar sets to ensure the highest levels of safety and efficiency.

Shaft Design

After selecting the bearings, motor and drawbar, and tool holder, the fundamental shape of the spindle can be drafted. However, it's important to note that the static analysis only provides the minimum bearings limits. To determine the maximum limits for spindle shaft dimensions, it's crucial to find the critical speeds and optimize them accordingly. This will provide a reliable answer for the maximum dimensions of the spindle shaft.

3.5.Campbell Diagram Using FE Simulations

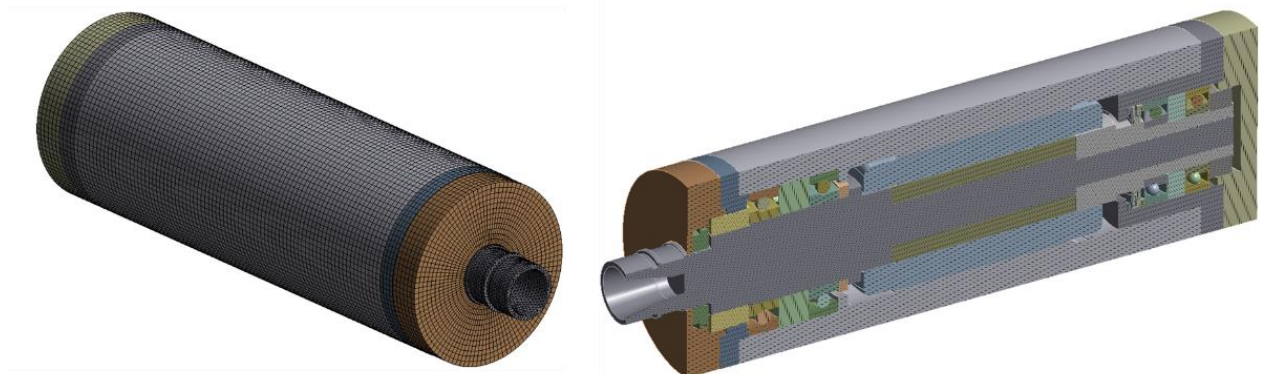


Fig. 3.1 The meshed CAD model of the test spindle.

When designing a spindle structure, it is crucial to account for the various rotating frequencies of the spindle shaft, including the inertial and gyroscopic moments, as well as whirl effects. At higher rotational speeds, it is essential to represent the inertia effects of the rotating parts accurately to predict the in-process behavior. One crucial aspect of the inertia effects is the gyroscopic moment introduced by the precession motion of the vibrating rotor as it spins. As the spin velocity (spindle speed) increases, the gyroscopic moment becomes critically

significant, and ignoring these effects at the design level can lead to bearing and support structure damage. To enhance the stability of a vibrating spindle shaft, it is essential to consider bearing stiffness and support structure flexibility and understand the resulting damping behavior.

In this study, we have constructed a comprehensive FE analysis to represent speed-dependent spindle dynamics. Fig. 1 depicts the representation of spindle dynamics. When one represents speed-dependent spindle dynamics for spindle structures, the considered structural elements can be narrowed down to the spindle shaft and the bearing elements since the other elements are standstill in operational conditions. We have extracted Campbell diagrams in ANSYS to predict and assess the modal frequencies during operation. The analysis frame can be selected as rotational or stationary. It is also possible to add speed-depended stiffness, gyroscopic and inertial effects. We have applied a parametric optimization study to determine the maximum shaft diameters, and a Campbell diagram of the test spindle was extracted in the FE model for our study. The constructed FE model involves the speed-dependent bearing stiffness and gyroscopic moment while excluding rotational damping. In a stationary reference frame, we are solving the following equation [54].

$$[M]\ddot{u} + ([C] + [G])\dot{u} + ([K] + [B])u = f \quad (1)$$

M, C & K are the standard mass, damping, and stiffness matrices. G & B represent the gyroscopic and the rotating damping effect. The spindle speed range for The Campbell diagram is from 0 to 100K rpm. The extracted modal frequencies are for 10 K rpm, 40K rpm, 80K rpm, and 100K rpm.

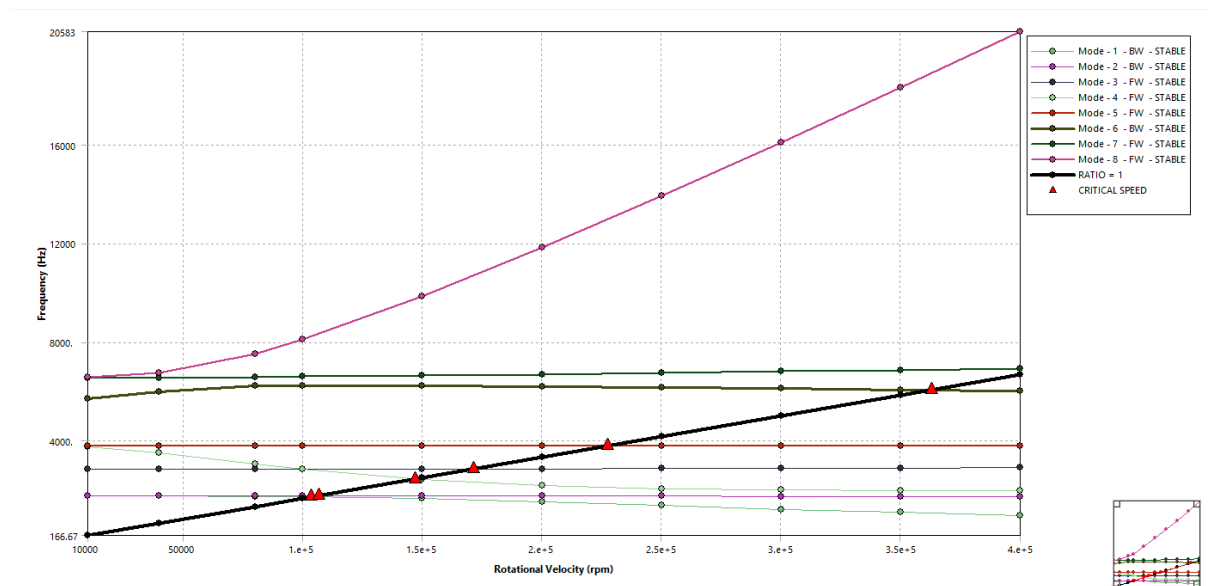


Fig. 3.2 The Campbell diagram for the test spindle

The spindle modes and their critical speeds are clearly indicated in Fig.2. The black line represents the slope of the critical speeds, while the other horizontal lines illustrate the modes in Fig. 2. In Table 1, the critical speeds and modes are presented. The first two modes show backward motion, while the 3rd to 5th modes illustrate a forward motion, and the 6th mode is again a backward motion. When the mode frequencies are analyzed for different speeds, the

1st mode is around 1772 Hz at 10K rpm and shifts to 1763 Hz at 40K rpm, while it reduces to 1744 at 80K rpm. A similar frequency reduction can be observed at 100K rpm for the 1st mode, approximately 1727 Hz. A similar frequency change trend is also seen for the 2nd mode while the 3rd mode frequency remains constant. These results indicate that the FE model captures the speed-dependent frequency accurately.

Table 3.1 The speed-dependent modes for the test spindle

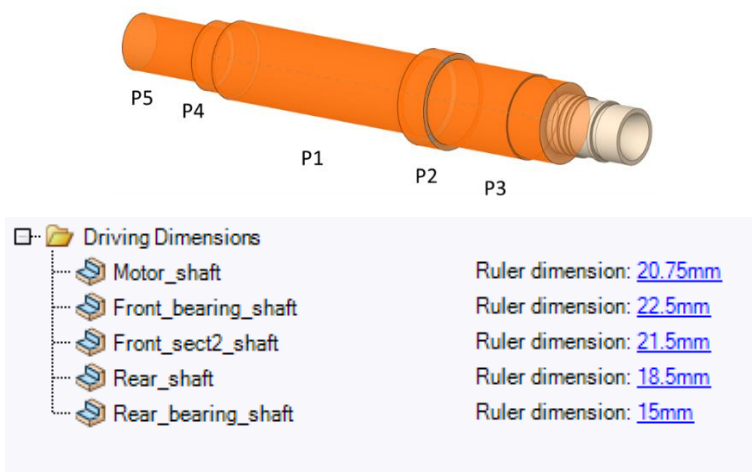
Mode	Whirl Direction	Mode Stability	Critical Speed	10000 rpm	40000 rpm	80000 rpm	1.e+005 rpm
1.	BW	STABLE	1.0344e+005 rpm	1771.6 Hz	1763.8 Hz	1744.2 Hz	1728.6 Hz
2.	BW	STABLE	1.0656e+005 rpm	1774.9 Hz	1777.2 Hz	1777.4 Hz	1776.6 Hz
3.	FW	STABLE	1.7156e+005 rpm	2848. Hz	2848.5 Hz	2850.3 Hz	2852.9 Hz
4.	FW	STABLE	1.4683e+005 rpm	3767.5 Hz	3519. Hz	3054. Hz	2838.1 Hz
5.	FW	STABLE	2.2748e+005 rpm	3791.3 Hz	3791.3 Hz	3791.3 Hz	3791.3 Hz
6.	BW	STABLE	3.6309e+005 rpm	5720.6 Hz	5998.8 Hz	6224.9 Hz	6245.7 Hz

To improve and optimize the spindle structure, critical speed optimization is necessary after modeling the speed-dependent spindle shaft modes. To achieve this, we set the critical speed for the first structural mode to be twice the maximum motor speed, which in our case is 100K rpm. We then constructed an optimization problem to determine the maximum possible rotor and bearing diameters for a critical speed of 100K rpm. However, we found that the upper bound for the rotor inner diameter shaft is limited according to the electric motor catalog. Our test spindle has an initial rotor inner diameter of 20.75mm, but we needed to enlarge it up to 40mm to select a proper electric motor. The optimization range for the rotor inner diameter was set between 15mm and 40mm. ANSYS automatically determined the other dimensions after we gave the rotor inner diameter. The parametrized shaft radiiuses are shown in Figure 16. To optimize the spindle structure, we used the Adaptive Single Objective Method as the optimization algorithm, which is a gradient-based solver.

3.5.1. Optimization Problem Statement:

Objective: 1st. Mode of the critical speed 100 000 RPM

Geometric Constraints:



Name	Lower Bound	Upper Bound	
P1 - Motor_shaft (mm)	15	40	
P2 - Front_bearing_shaft (mm)	20.25	24.75	
P3 - Front_sect2_shaft (mm)	19.35	23.65	
P4 - Rear_shaft (mm)	16.65	20.35	
P5 - Rear_bearing_shaft (mm)	13.5	16.5	

Fig. 3.3 The parametrized shaft radiuses and the optimization problem

3.5.2. Optimization Results for Mode of the critical speed 100 000 RPM

The optimization results are shared in Fig.4. As you can see, the parametric optimization study searched for 100 design points, also shown in Fig.4. Interestingly, the results indicate that with a 27mm rotor inner radius, we can use a 40 mm diameter sized front bearing and 30 mm rear bearing. However, when we reduce the rotor diameter to 25 mm, we can increase the rear bearing diameters to 40 mm. These findings will be incredibly useful in the rotor and bearing selection process for the thermal part.

	Candidate Point 1	Candidate Point 2	Candidate Point 3
P1 - Motor_shaft (mm)	27.033	28.278	17.121
P2 - Front_bearing_shaft (mm)	23.813	21.979	22.635
P3 - Front_sect2_shaft (mm)	21.542	20.435	22.655
P4 - Rear_shaft (mm)	16.911	17.69	17.556
P5 - Rear_bearing_shaft (mm)	15.594	13.576	15.101
P10 - Mode-1 (rev min ⁻¹)	★ ★ ★ 99987	★ ★ ★ 1.0011E+05	★ ★ ★ 1.0011E+05

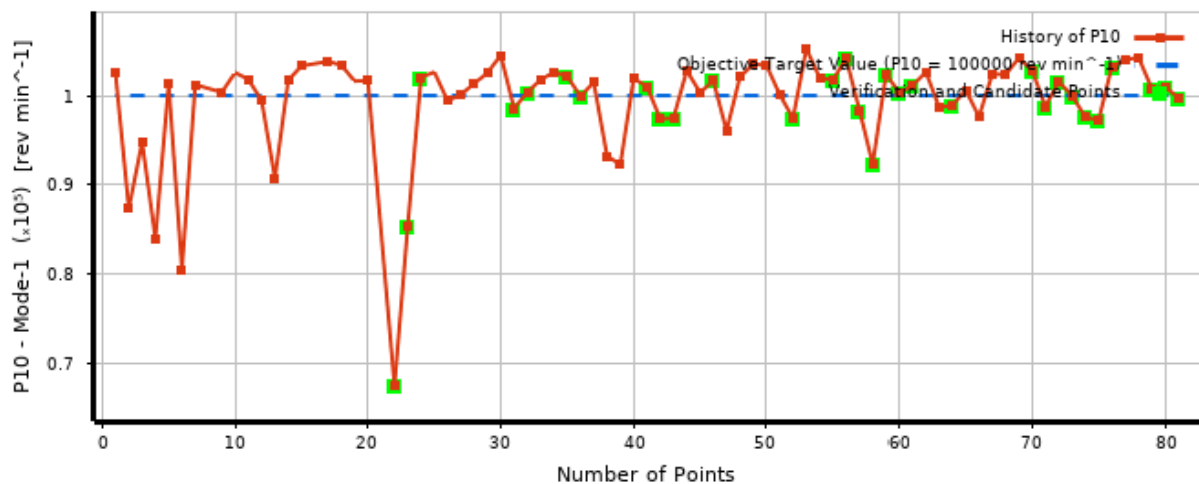


Fig. 3.4 The optimized shaft radiuses for 100 K rpm critical speed

3.6. Auxiliary Spindle Components

After conducting extensive research, it has been found that high-speed spindles require specialized components that can withstand challenging dynamic and thermal boundary conditions. Traditional spindle elements like locknuts and classical seal systems are not suitable for these spindles, and as a result, stepped sleeves, labyrinth seals, flinger/slingers, and constant

preload mechanisms are used to enhance the design and achieve a robust high-speed spindle. It is important to note that due to the high cost of researching these spindles, auxiliary spindle components are not studied extensively, but the results of FE and optimization simulations have provided valuable insights into the critical points that must be considered when designing high-speed spindles.

Bearing Spacers

To ensure that the rotating elements and cooling system have an extended life, it is important to employ appropriate lubrication for the bearings and other shaft components. To achieve this goal, spacers are used between bearings to provide lubricants and drainage passages. At high speeds, conventional oil lubrication may not meet the system's requirements. Therefore, oil-air lubrication will be used for this spindle. The front and back bearing sets share the same input and output for lubrication and are connected via lubricating channels in their spacers. The dimensions of the channel and spacer are determined according to the manufacturer's recommendations.

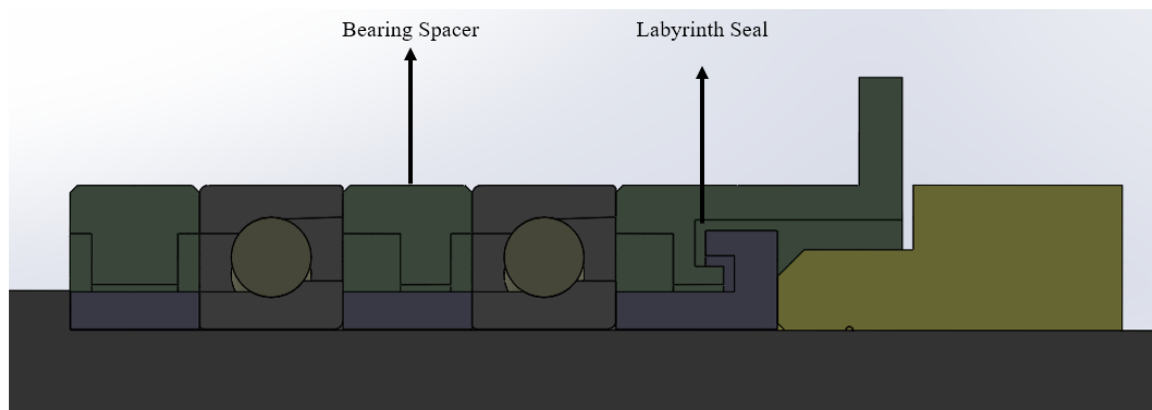


Fig. 3.5 Bearing Spacers

Stepped Sleeves:

Stepped sleeves are specialized components designed to enhance the stiffness of the shaft. These sleeves have two inner diameter sections, separated by a step, and they are an interference fit on the shaft, instead of locking nuts that are screwed on the shaft. This can increase the axial load-bearing capacity of the shaft without creating as many alignment problems as possible. The stepped sleeves:

- Serve as locknuts for bearings.
- Increases the dynamic and static rigidity (especially at the rear bearing side with mode splitting)
- Potential to be used as sealing components-Higher flange dimensions increase the forced convection of the shaft and ease heat dissipation.

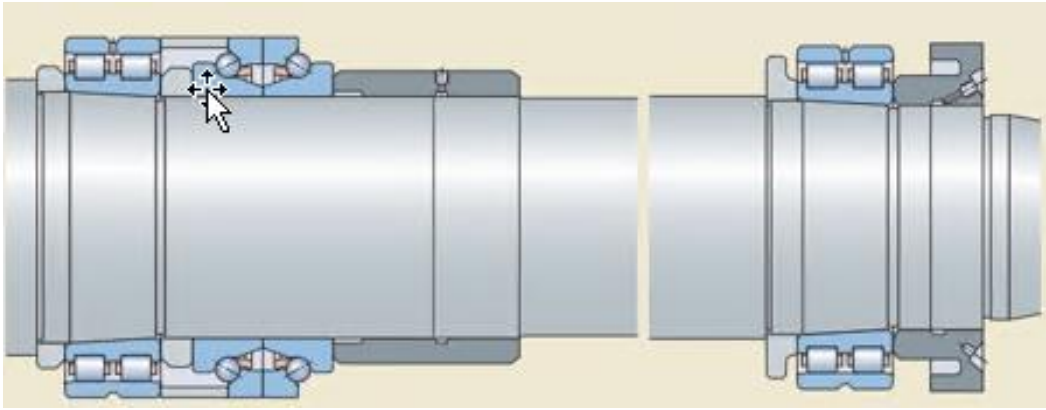


Fig. 3.6 Plain and flange type of stepped sleeves to lock bearings.

Labyrinth Seals

When operating at high speeds with pressurized lubrication, it is crucial to ensure proper sealing. Seals must be applied to bearing assemblies and preload assemblies to prevent any leaks or damage. The labyrinth channels are meticulously designed, considering both thermal and dynamic considerations. By doing so, we can ensure optimal performance and longevity of the machinery.

- It avoids solid and liquid particle splash and contamination as a seal.
- Composed of rotor and stator parts.
- The rotor part increases forced convection and eases heat dissipation.
- Generally, the stator of labyrinth bearings also serves as a preload device. Such a device provides two advantages:
- Provides the shortest front bearing location to the tooltip and reduces possible thermal distortions for preload application.

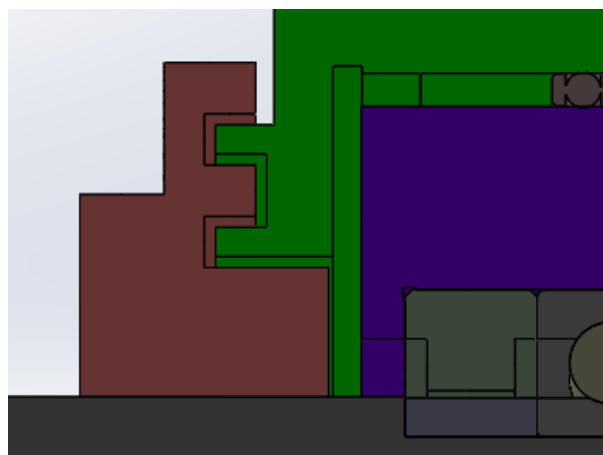


Fig. 3.7 Labyrinth Seal Design for Rear Bearing

Flinger/Slingers:

When working in tight spaces, it's important to prevent dirt or oil from contaminating the bearings. This is where a finger comes in handy - it creates a centrifugal force that helps keep everything clean and running smoothly. Use it before installing labyrinth seals to ensure that your bearing lubricant stays sealed and protected.

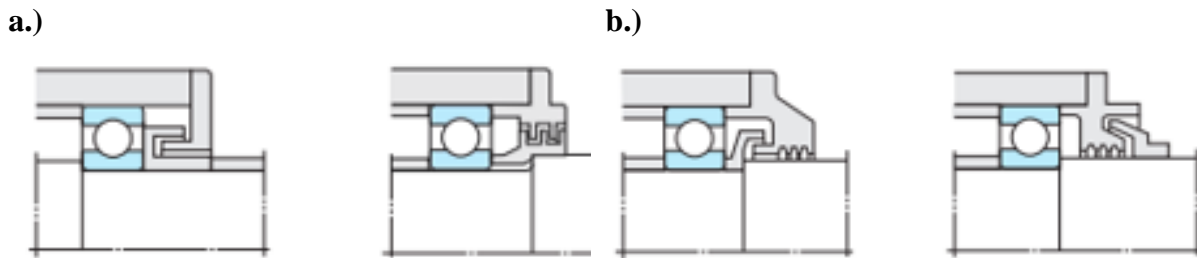


Fig. 3.8 a.) Axial and radial labyrinth seals, b.) flingers to avoid lubricant leakage and dirt contamination.

In this study, the conceptualized and designed spindle called MRL-40K. The front bearing size is 45mm while the rear bearing size is 35mm, which was selected based on static and dynamic analysis. In Fig. 9, you can see the design layout for MRL-40K. This layout provides a compact design for MRL-40K stepped sleeves, which act as rotors of labyrinth seals, especially on the electric motor side. The first sleeve fixes the inner rings of the front bearings while also acting as a heat shield to prevent heat from the motor. It also avoids particle leakage and contamination between the front bearings and electric motors. Similarly, the second stepped sleeve shields heat from the motor and rear bearings and is used as a labyrinth rotor. The third stepped sleeve is placed between the rear bearings and encoder to fix the inner rear bearing rings. The size of this stepped sleeve is crucial for spindle dynamics compared to the first two stepped sleeves since it creates a tail length effect.

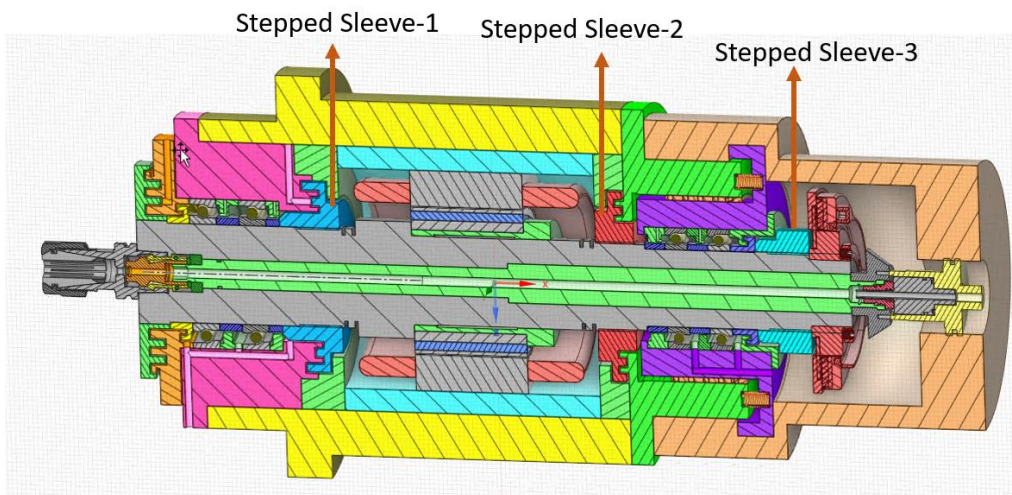


Fig. 3.9 The multi-functional stepped sleeves designed for the MRL-40K.

When it comes to the MRL-40K, labyrinth seal applications are crucial to prevent leakage and dirt contamination. These seals must be adjusted and optimized based on their specific functions. For example, the first labyrinth seal is responsible for keeping dirt from the outside

of the bearing. To achieve this, the seal needs to be as short as possible so that the front bearings can be located near the tooltip. To accomplish this, we utilized a radial labyrinth seal, which is commonly used in high-speed applications.

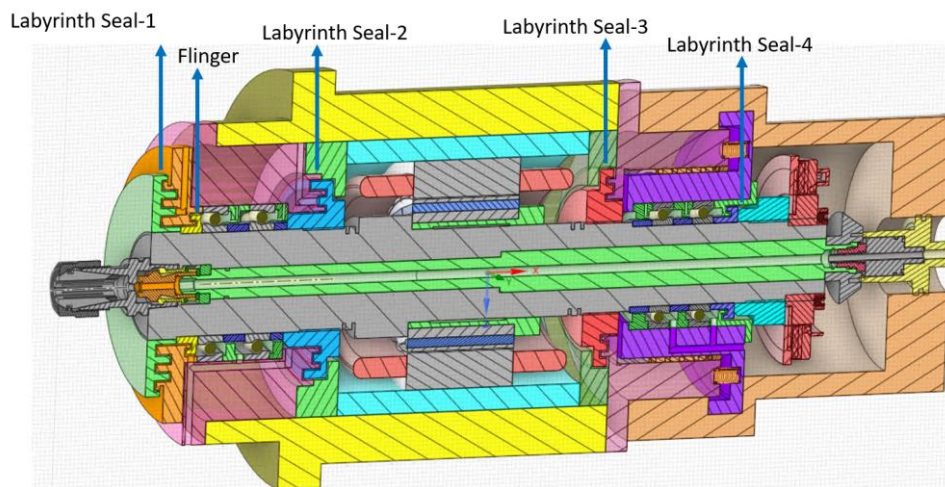


Fig. 3.10 10 The multi-functional labyrinth seals designed for the MRL-40K.

The design of the stator in the first labyrinth seal is such that it not only provides a pressure application area for preload, but it also fixes the outer rings of the front bearings. Flinger-1, which is placed between the first labyrinth seal and front bearings, serves the purpose of preventing any bearing oil leakage outside. The second and third labyrinth seals have been designed with three components, which not only provide a compact space but also increase the functionality. These labyrinth seals are aimed at preventing any bearing oil leakage from the bearings to the electric motor. Finally, the fourth labyrinth seal is designed to prevent oil leakage from the rear bearings to the encoder.

Constant preload mechanisms:

The rear bearing assembly is built to have a floating bearing system, which provides several advantages to the spindle assembly. One of these advantages is that the bearings are kept at a constant preload, even at high rotational speeds, which improves thermal performance. Additionally, the spindle dynamics are more stable and predictable with this setup. To achieve this mechanism, a floating bearing bush is incorporated into the assembly, allowing the rear bearing to move axially. When the spindle heats up and expands during operation, the inner races of the bearings move along with the expansion of the shaft while the outer races remain in line with the spindle housing due to the rollers in the bushing. This ensures that the bearings remain at a constant preload.

- Spring preload, called constant or compliant preload, uses a spring pack arrangement to apply bearing preload.
- Spring preload has the advantage of maintaining a relatively constant bearing preload and compensating for thermal growth and, to some extent, centrifugal forces. Spring preload is commonly found in high-speed spindles.

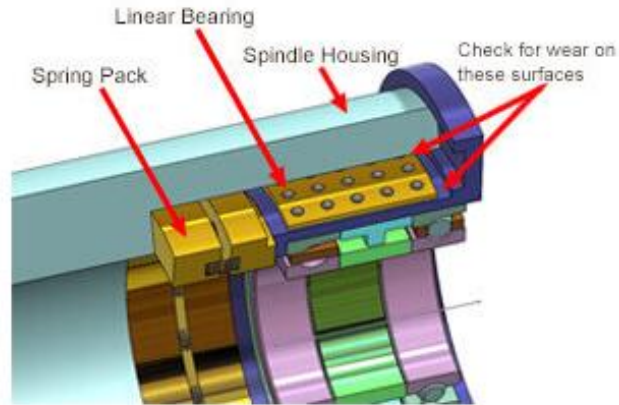


Fig. 3.11 Constant preload mechanism example

During the design phase, we aimed to create a short shaft system for better dynamic behavior and to avoid critical speeds. To compensate for thermal growth and centrifugal forces, we wanted to use a constant preload mechanism. However, we realized that placing the mechanism close to the electric motor could cause excessive thermal distortions and a longer shaft size. So, we decided to relocate the spring pack to the backside of the rear bearings for more space and to avoid thermal distortions. This new design also allows for compensation of misalignment and allows the spindle to run smoothly and quickly. You can see the new compact design in Fig. 12.

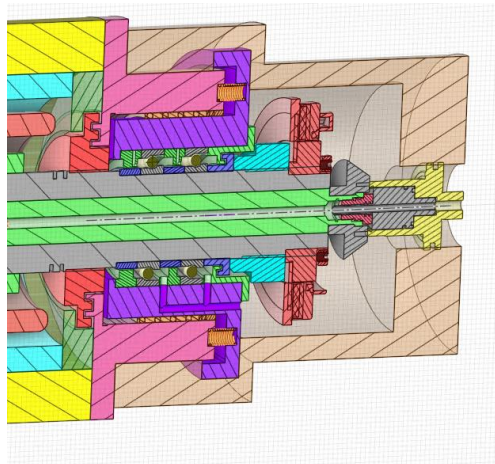


Fig. 3.12 The designed compact constant preload mechanism for the MRL-40K

3.7.Lubrication and Drainage System

As we discussed previously, we considered various lubrication systems for achieving 40,000 rpm in this study. Since we lacked expertise in this area, we consulted experts during the design phase. Based on their recommendations, we decided to go with an oil-air lubrication system. Although more advanced systems like jet oil lubrication exist, they are usually expensive and complex to implement. As this is a test spindle, we will not be recirculating the oil, which would require additional oil pumps and reservoir systems. Instead, we will be using spacers to provide an oil-air mix for the bearings in the chosen lubrication system. We designed auxiliary

spindle components according to the standard dimensions of miniature ready-to-use oil-nozzle systems, which are typically 3mm.

Moreover, to avoid capillary effects, we set the drainage passages of bearing oil to 4 mm. Our research indicates that drainage passages smaller than 2mm may be prone to showing capillary effects. You can see a detailed representation of our selected lubrication system in Figure 13.

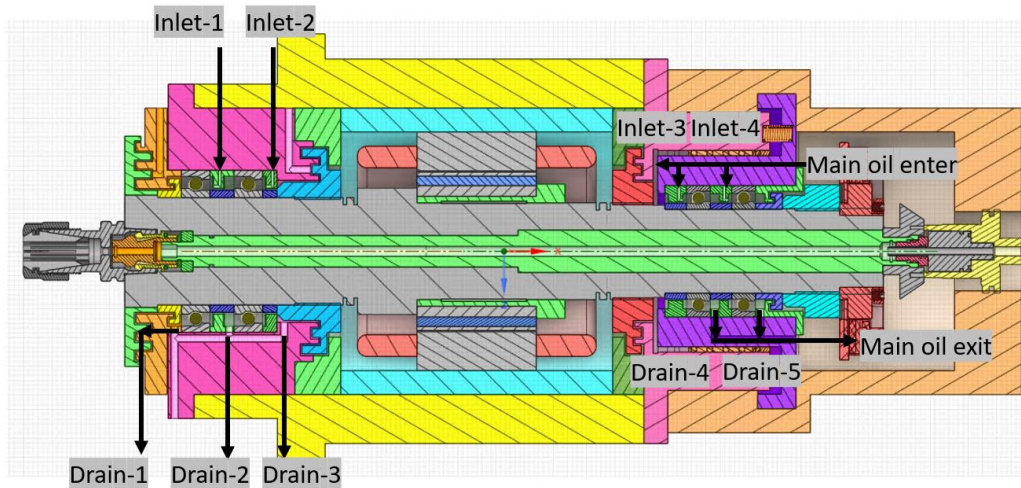


Fig. 3.13 The designed lubrication and drainage system for the MRL-40K

We were faced with the challenge of designing sliding/mobile machine elements that shared an interface with the outer rings of the rear bearings, as shown in Fig.13. To compensate for possible thermal growth, we used a constant preload system at the rear bearings. However, we found that placing the rear bearing lubrication system on inactive components could cause oil leaks. To avoid this issue, we designed lubrication channels on the sliding/mobile machine elements, specifically Inlet 3& 4 and Drain 4 & 5. This was the safest solution to ensure that there were no leakages among the components.

3.8. Final Spindle Design and Manufacturing Details

3.8.1. The Shaft Design

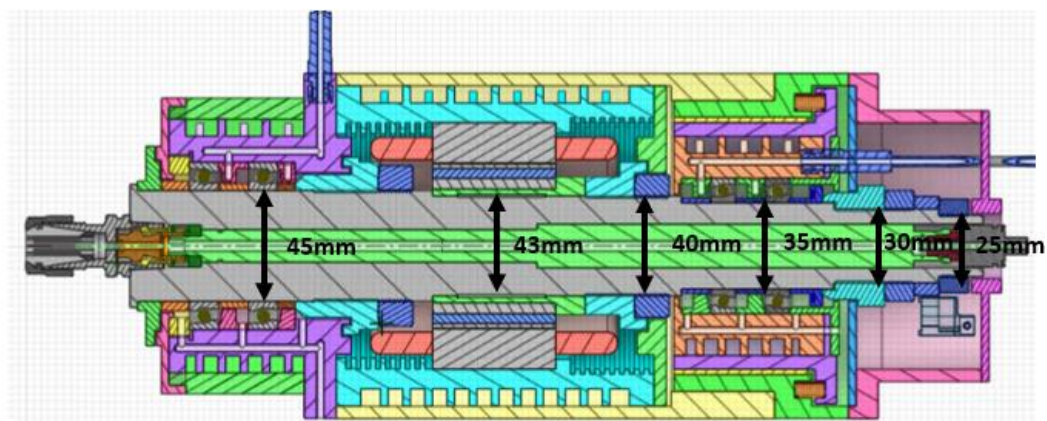


Fig. 3.14 The shaft diameters for the final design

The Shaft Diameters

The total shaft length is 346.25 mm for the final design approved for manufacturing. The front bearing shaft diameter is 45 mm, while the rear bearings measure 35 mm. The electric motor sleeves have a diameter of 43 mm, while the stepped sleeve and locknut pair measure 40 mm. The shaft diameter for the rear bearing fixing and encoder is 30 mm, and the tail length diameter is selected as 25 mm. The rear bearing diameter for the base test spindle is 30 mm, but with the optimized design, the rear bearings have been enlarged by 5 mm and finalized as 35 mm.

The Bearing Locations

Based on dynamic studies, it was found that the front bearings should be placed near the spindle tip to achieve better dynamic behavior. As a result, we opted to use the shortest compact sealing elements to establish the shortest possible distance between the front bearing set and the spindle tip. Currently, the front bearing set is situated 24mm away from the spindle tip, which is 32.8mm for the base spindle. It's worth noting that the front bearing width is 12mm, which is 25% smaller than the base spindle bearings (16mm). The long spacer length is 12mm, which is the same size as the bearing, while the short spacer length is 7mm. In comparison to the base spindle, the front bearing set is 43mm long, whereas the diameter is 53mm. The front bearing arrangement that was chosen is a fixed position arrangement. The front bearing is positioned using a spacer and shoulder on the shaft from the front side, while the rear side is fixed using a stepped sleeve and a 45mm locknut on the shaft.

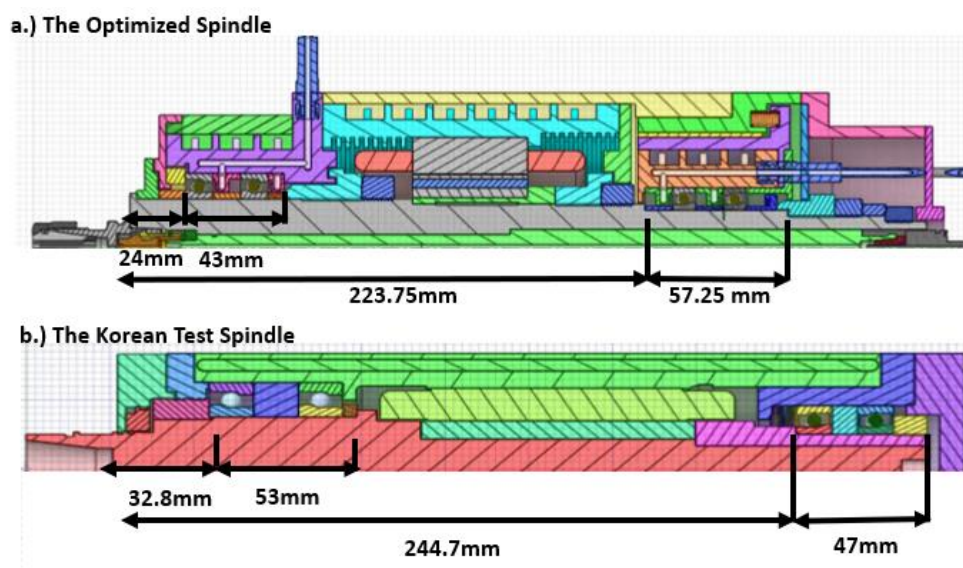


Fig. 3.15 The bearing location on the shaft for the final design

Based on the specifications in Fig. 15, it appears that the rear bearing set location for the new design is 223.75 mm away from the spindle tip. This is slightly different than the base spindle, which has a rear bearing set location of 244.7 mm. To optimize the test spindle, three spacers were added, each with larger bearing diameters than the base spindle. This resulted in a rear bearing fixed length of 57.25 mm and a rear bearing set length of 47 mm with one spacer in the base spindle. The back bearing arrangement is a floating bearing arrangement, with the bearings fixed on the shaft. On the front side of the rear bearing, there is a spacer and shaft

shoulder, while the other side has a spacer and locking sleeve with gradual diameters of 35 mm and 30 mm. To ensure positional accuracy, a 30mm locknut has been enabled.

Motor Location and Dimensions

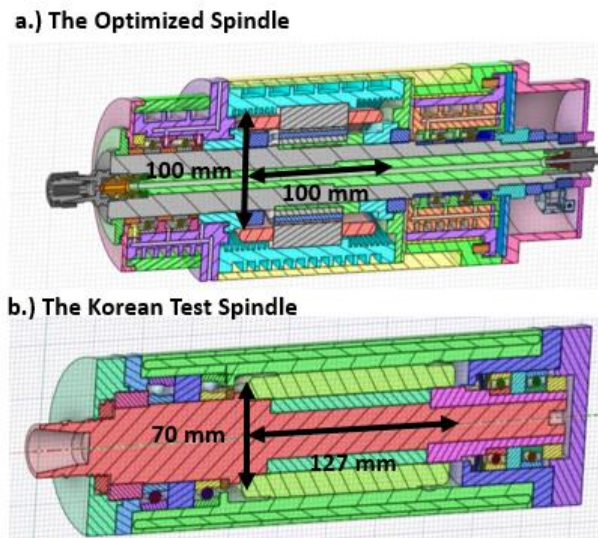


Fig. 3.16 The motor location and dimension comparison

Based on Fig.16, it seems that the chosen 40,000 rpm motor is a bit smaller than the base spindle in terms of length and wider by 30mm. The torque for both spindles' electric motors is the same, which is 3Nm. The rotor diameter of the motor is 46mm, the same as the front bearing diameter, and it is positioned 122.75mm away from the spindle tip. The rotor wall thickness is 20.3mm and 50mm in length, while the stator's external diameter is 100mm. In Fig.16b, you can see a comparison between the electric motor diameters of the new and base spindles.

The electric motor will be connected to the shaft with a motor sleeve, like the base spindle. This motor sleeve will feature an oil pressing area that is 1.25mm in thickness, specially designed for dismantling the motor from the shaft. The overall oil area is 1.25mm x 35.5mm between the shaft and the motor sleeve. Fig. 17 illustrates the gap between the shaft and motor sleeve, which is crucial for oil-pressurized dismantling of the electric motor.

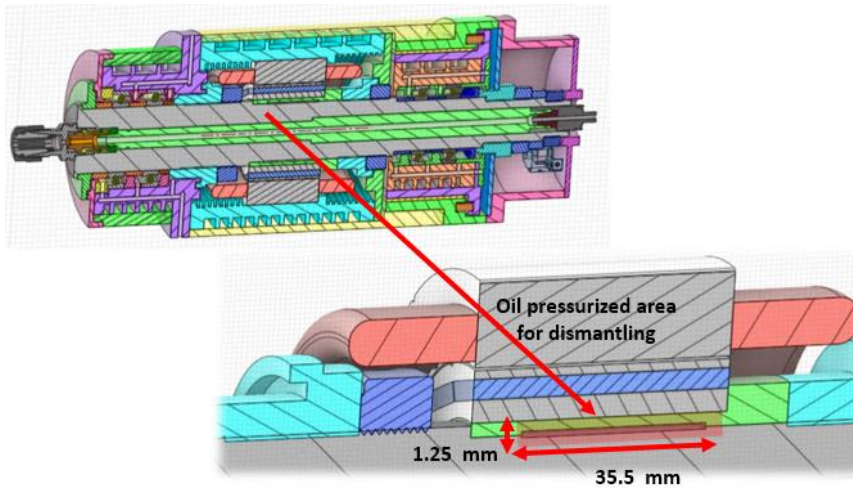


Fig. 3.17 The oil pressurized area for motor dismantling.

Encoder Selection

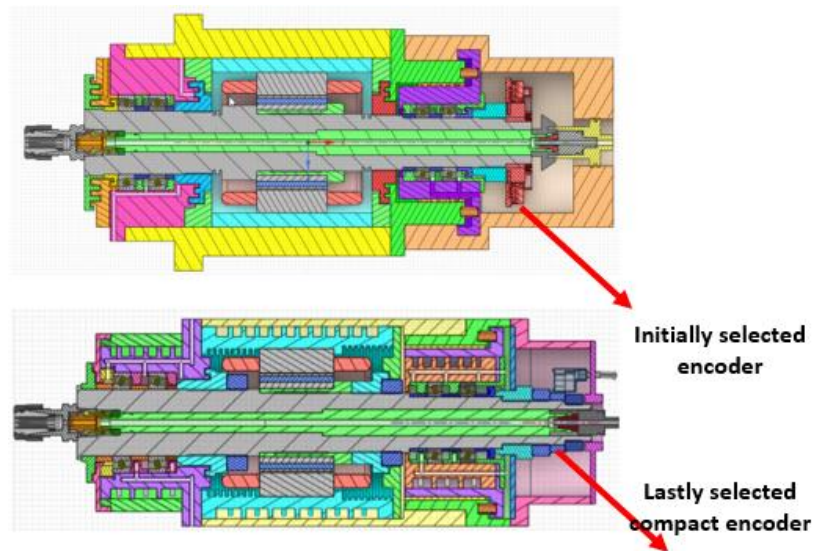


Fig. 3.18 The comparison of the initially selected and lastly chosen encoders.

Hollow shaft encoders are the most suitable encoders that can withstand harsh operating conditions. Therefore, the new spindle design selects a hollow shaft-type encoder with a 30 mm diameter. Initially, a 50 000 rpm Heidenhain encoder was selected for the shaft [55], but since it has a notable volume, this selection needed to be revised for manufacturing. So, we decided to search for compact alternatives for the spindle. We found a compact encoder design special for spindle structures from SpinCo encoder, which is a side brand of Renishaw [56]. The comparison of the initially selected and the last chosen compact encoders is illustrated in Fig. 18. As shown in Fig. 18, and the first encoder has larger outer diameters than the previously decided encoder.

Balance Rings

When it comes to rotating elements, proper mass balancing is essential for smooth and trouble-free operation. This is particularly true for high-speed spindles, where balancing quality plays a crucial role in spindle dynamics. To ensure optimal balance, many manufacturers use balance rings on spindle shafts, which must be press-fit at the front and rear tips of the spindle. In fact, the use of balance rings is quite common among advanced high-speed spindle manufacturers, as evidenced by the examples shown in Fig.19. So, if you want to keep your spindle running smoothly and reliably, be sure to pay close attention to balancing quality and consider using balance rings as needed.

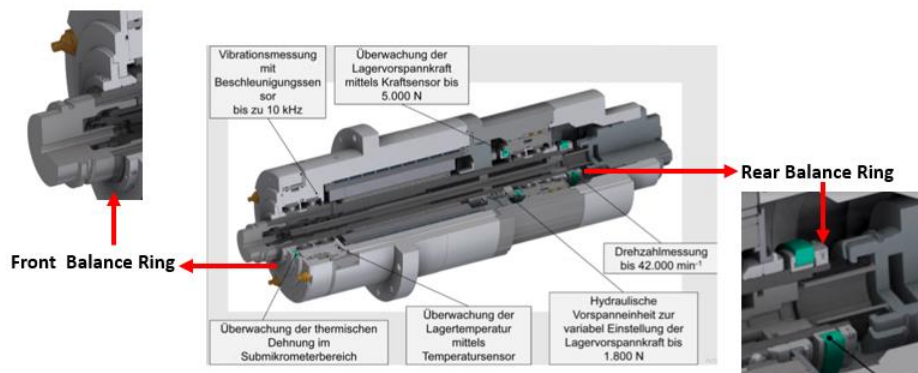


Fig. 3.19 The balance ring example from an industrialized 42 000 rpm spindle [57]

The balance rings are located at the front and rear spindle tips for the new spindle. These rings are highlighted in Fig.20. The front balance ring also supports external preload adjustment for the front bearing set, while the rear balance ring is employed for the encoder fixing.

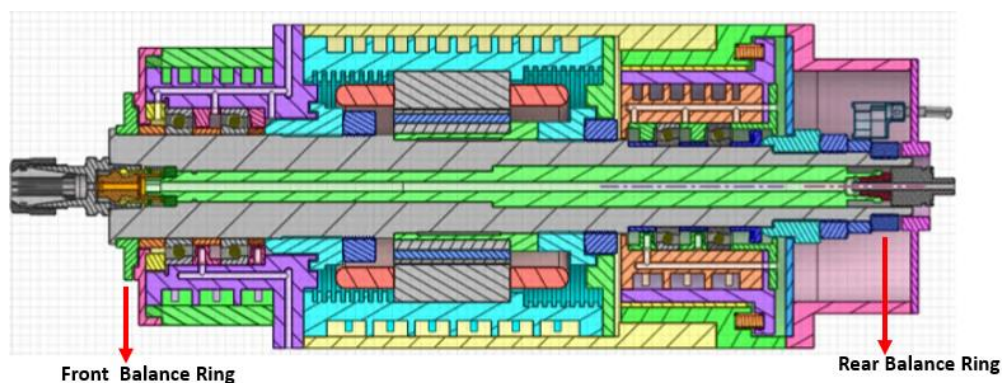


Fig. 3.20 The balance rings for the new spindle (40 000 rpm)

3.8.2. Housing Design

Housing Design for the Front Bearings with Fixed Bearing Arrangement

When assembling the spindle design, it's important to note that the front bearing inner rings are fixed from the shaft side. The shaft itself can move together with the inner bearing rings, but the outer bearing rings have interference tolerance with the housing side. This means that the housing is considered a stationary and non-moving part of the spindle assembly. To achieve a

fixed bearing arrangement for the front bearings, also known as a rigid preload arrangement, the outer bearing rings are set using yellow and purple parts. These parts are indicated in Fig. 21 and the yellow piece is assembled into the purple part with M 1.5 threads to make assembly of the spindle structure easier.

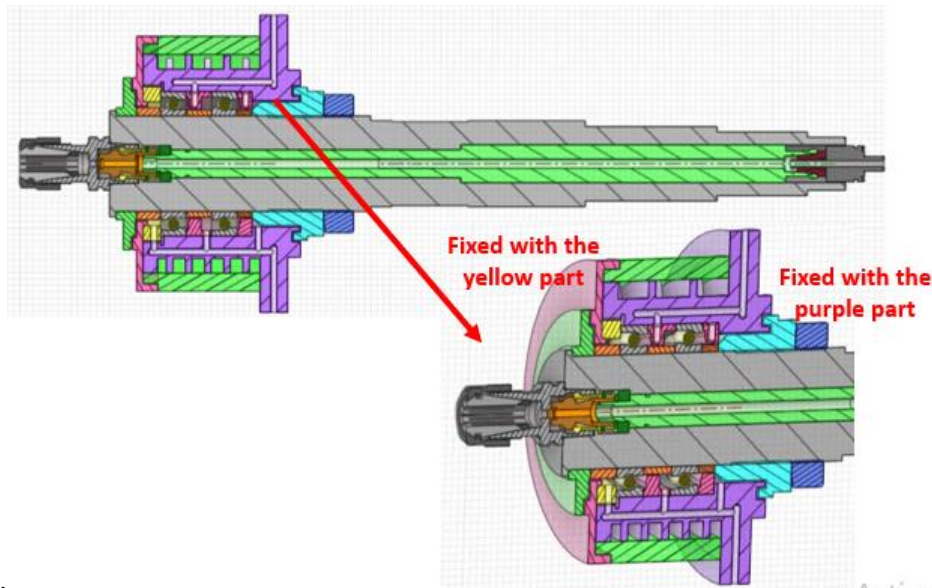


Fig. 3.21 The housing design for the front bearings

Housing Design for the Rear Bearings with Floating Bearing Arrangement

When setting the rear bearing inner rings on the shaft, it's important to note that they can slightly slide on the shaft for preload adjustment. For high-speed applications, bearing preload is crucial, and a constant preload mechanism is typically preferred. This type of mechanism requires a floating bearing arrangement for the outer bearing rings from the housing side. In this arrangement, the outer rings are supported in the radial direction only and are free to slide in the axial direction. After factory or assembly preload application, the axial play of outer rear bearings relates to a soft spring. If there is an external preload, the soft spring will squeeze until a threshold value, and the axial play of outer bearing rings will remain the same with the help of sliding ball bushing. Thermal growth due to spindle operation will increase preload at the front bearings, which will squeeze the soft spring. The rear bearings' preload will try to increase their contact angles by causing the outer rear bearings to move backward, which shares the same direction as spring loading due to the front bearing thermally induced preload increase. Thus, to maintain the rear bearings' contact angle at the initial position, the spindle shaft will also move backward with the help of the floating bearing and ball bushing mechanism. As a result, the rear bearings will preserve their initial preload, while the front bearing will be preloaded more due to thermal changes. For a better understanding of the housing design for the floating bearing arrangement, you can refer to Fig.22 with the help of ball bushing.

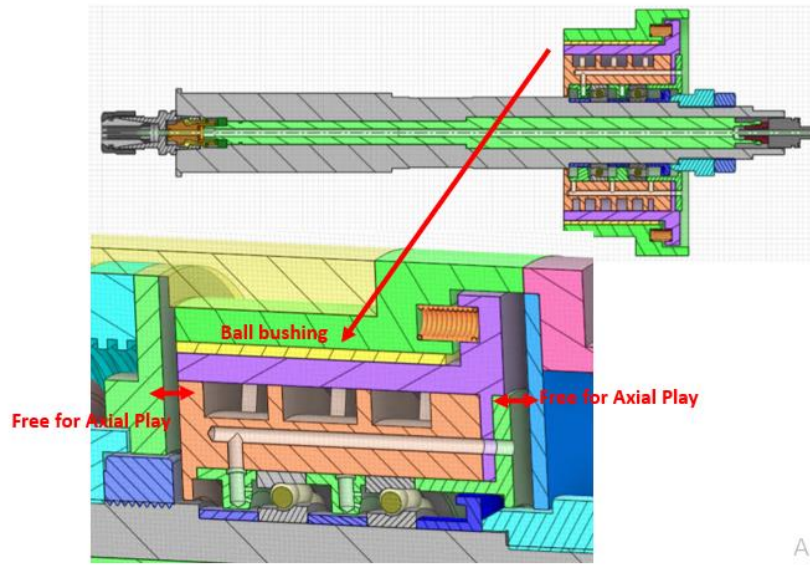


Fig. 3.22 The housing design for the rear bearings

Cooling Regions for The Housing Design

Based on the FE results, it was found that the thermal gradient increases exponentially when the bearings and motor have similar radial dimensions. To counteract this, it is recommended to use smaller and radially shorter bearings with radially taller motor sizes, which will help to ease heat dissipation. Many high-speed spindle manufacturers use sectional local cooling systems instead of central ones. This means that radially different cooling areas are designed for front and rear bearing and motor cooling. The local cooling regions that were determined are shared in Fig.23.

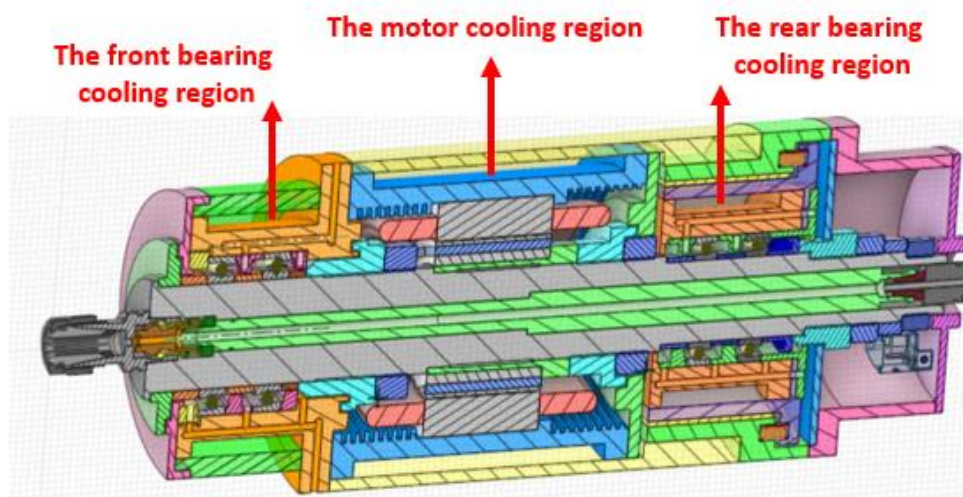


Fig. 3.23 The cooling region areas for the spindle housing

According to the specifications, the front cooling region has a length of 48.25 mm, and the cooling fluid depth can be increased to 7 mm. Additionally, the motor cooling region measures 109 mm in length, with a liquid depth that can also reach up to 7 mm. Lastly, the rear cooling

area has a width of 46 mm and a depth of 7 mm. If you need further details, you can refer to Fig.24 for the shared cooling region dimensions.

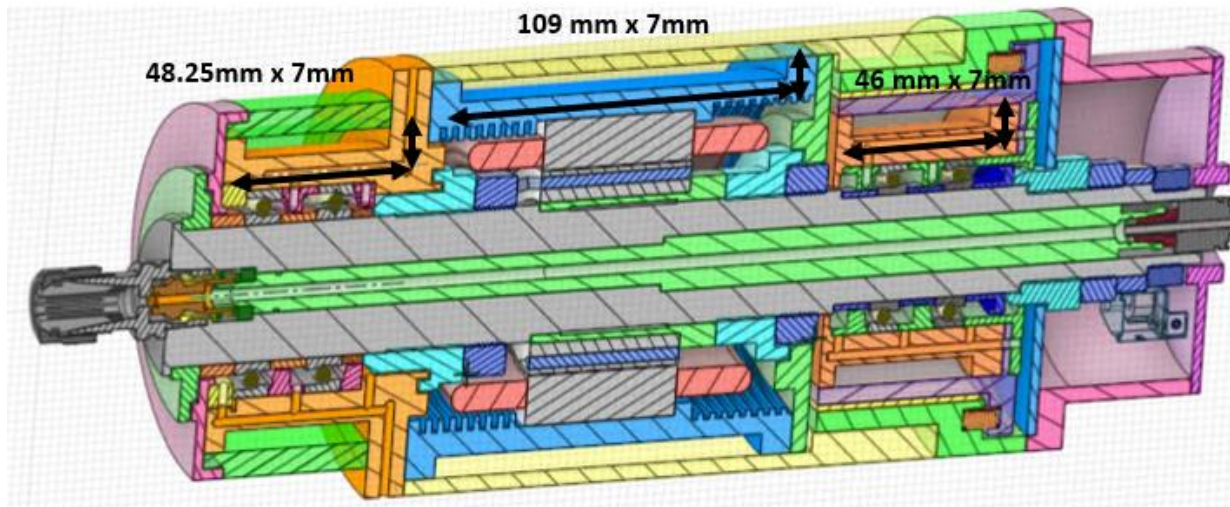


Fig. 3.24 The cooling region dimensions for the spindle housing.

We have observed a similar cooling region design on Fisher spindles that operate at high speeds and torque and have shaft cooling features. We optimized the shaft hole to enhance shaft cooling and requested an additional budget for a rotary union. However, due to budget constraints and our request being rejected, the shaft cooling feature had to be canceled from the final design. A picture of the cooling region design on Fisher spindles is shared in Fig.25.

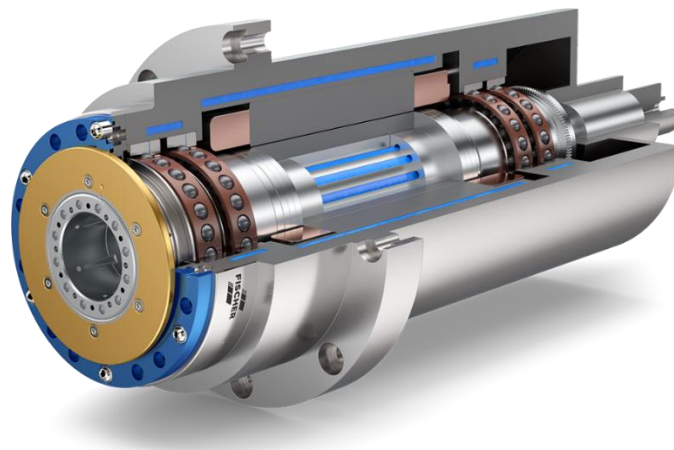


Fig. 3.25 The cooling regions for a High-speed and torque Fisher Spindle [58]

3.8.3. Preloading Mechanism Design

Since the highest spindle speed will be 40 000 rpm and the electric motor torque is 3 Nm, we needed to decide on a trade-off between the dynamic and thermal behaviors. Increasing the number of bearings would increase dynamic rigidity but deteriorate the thermal behavior. Thus, we decided to use the minimum number of bearings with the most rigid bearing configuration. In the literature, Shin et al. proved that the 'O' configuration is the most rigid bearing

arrangement regarding dynamic rigidity [51]. Thus, we selected the bearing configuration by employing two tandem bearings at the front and two at the rear side of the shaft. In general, high-speed spindle application employs rigid preload mechanisms for the front bearing and constant preload mechanisms for the rear bearings. The rigid preload mechanism provides dynamic and static rigidity to the system. The constant preload provides an accurate operation for high speed and thermal compensation while providing relatively low rigidity compared to rigid preload configuration. The bearing factory/assembly preload should be the same for the bearing set that composes the 'X' or 'O' configuration. The total preload value is shared according to configuration and bearing numbers. The preload distribution for high-speed spindles for the 'O' configuration with different bearing numbers is shared in Fig.26.

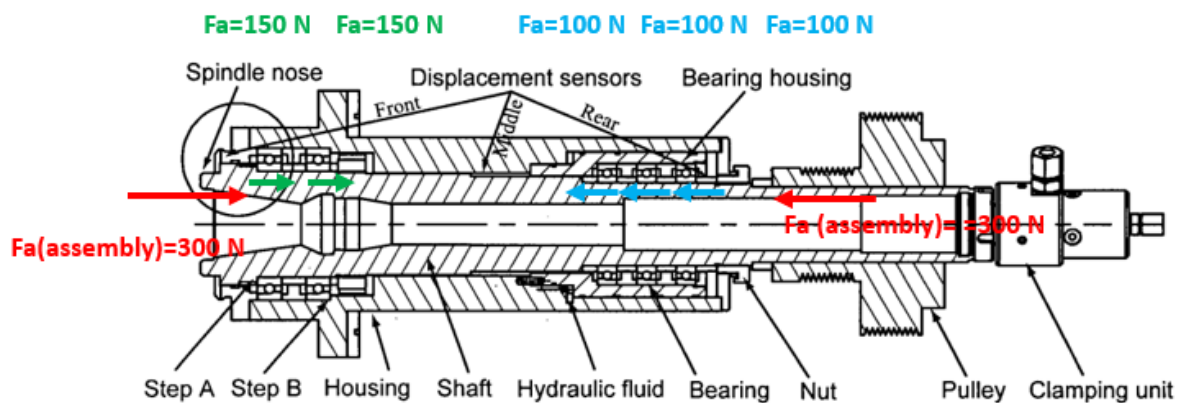


Fig. 3.26 The preload distribution for ‘O’ configuration with different bearing numbers [59]

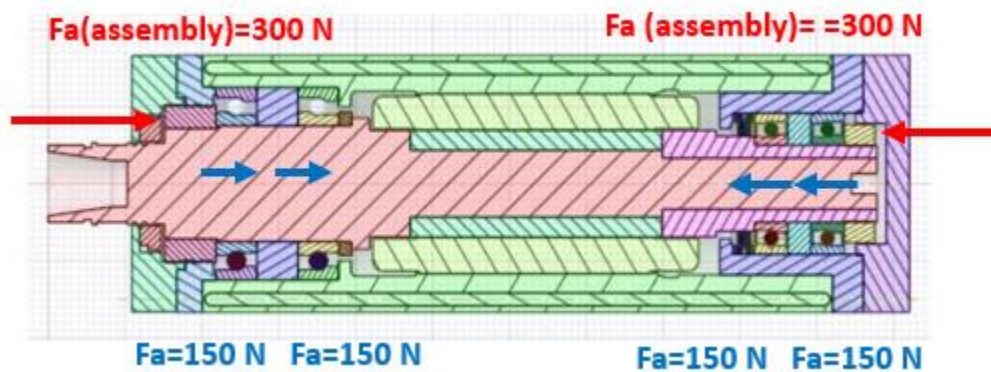


Fig. 3.27 The preload distribution for ‘O’ configuration with same bearing numbers

Factory/Assembly Preloading Adjustment

As we continue to delve into the intricacies of bearing pairs, we must consider the factory preload value. This value is determined by minimizing the total axial displacement for either the same size or different bearing pairs for tandem front and rear bearing sets. We will provide more information on how this calculation is made in upcoming sections. Previously, we discussed that front bearings have a rigid preload with a fixed bearing arrangement, while rear bearings have a constant preload with a floating bearing arrangement. Both arrangements were secured onto the shaft. In the final spindle design, the rear sleeve and locknut serve as tools for

factory preload adjustment for both front and rear bearings. These components are illustrated in Figure 28.

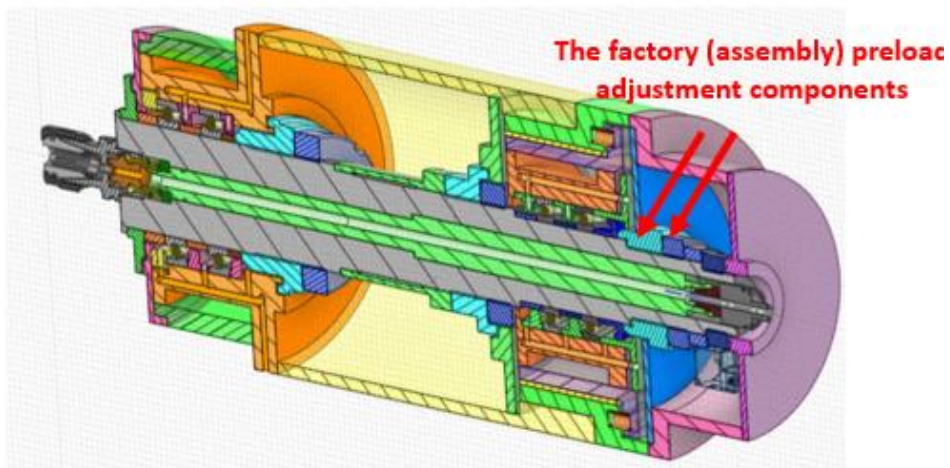


Fig. 3.28 The factory preload adjustment components

External Preloading Adjustment

After applying factory (or assembly) preload, an additional external preload from the spindle tip side can be used for the new spindle design. According to the final spindle design, an arbitrary external preload will affect the front bearings. In contrast, the rear bearings will preserve the preload value only caused by factory (or assembly) preloading. The external preloading adjustment is shared in Fig. 29.

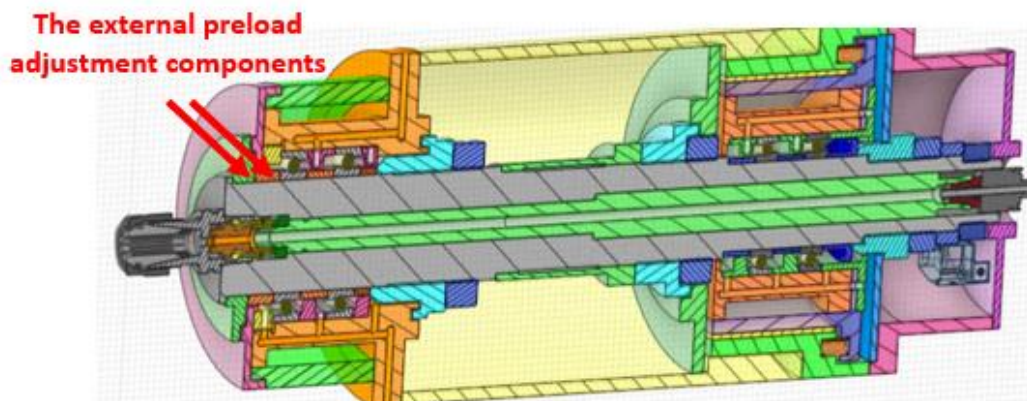


Fig. 3.29 The external preload adjustment components

3.8.4. Bearing Preload Selection and First Optimization

When it comes to spindles, it's important to keep in mind that bearing preloads plays a crucial role in determining their dynamic behavior. This is because they add stiffness and damping to the structure, which can affect not only dynamics but also thermal performance. Bearings produce heat and cause thermal expansion, as well as influence additional damping in high-

temperature areas. To achieve the desired dynamic and thermal performance goals, a multi-objective preload optimization scheme has been developed. This includes low peak FRF, high natural frequencies, and low peak temperatures. In addition, the selection of bearing preload mechanism and preload types are also important factors to consider when designing spindles.

In the earlier parts, we discussed the constant preload mechanism that was chosen for this spindle. The main reason for optimizing this mechanism is to minimize thermally induced preload. High-speed operation generates heat that causes thermal expansion of bearing components, leading to an increase in preload. The constant preload mechanism uses a soft spring that absorbs bearing ring expansion in the axial direction, maintaining the bearing contact angle and internal force unchanged. Additionally, this mechanism isolates the rear bearing set against external forces, which can significantly change the spindle's preload and alter its performance mid-operation. This arrangement has practical benefits as the system rigidity is more sensitive to changes in the front bearing preload, which can prove essential in designing chatter-free spindles.

Bearing Preload vs. Axial Displacement

Calculating the correct axial displacement for each spindle bearing is crucial for achieving accurate preloads during assembly. This is done by applying the bearing preload through displacement of one bearing race with an axial force, while keeping the other race stationary. This displacement causes the internal clearances of the bearing to close, resulting in higher contact stresses at the ball-raceway contact zone.

It is important to note that the axial load vs. axial displacement relationship for angular contact ball bearings is non-linear due to the Hertzian contact at the ball-raceway interface, which is generally defined as a point-loading phenomenon [59].

$$\delta \sim Q^{2/3} \quad (2)$$

where δ is the displacement and Q is the contact load. This relationship is adopted by bearing manufacturers and extended to the form [25]:

$$\delta_a = c F_a^{2/3} \quad (3)$$

where δ_a refers to the bearing axial displacement,

F_a is the bearing axial load,

c is the multiplicative inverse of the bearing axial rigidity.

The axial rigidity value is an important factor to consider when designing preloading assemblies for bearings. This value is reported by bearing manufacturers for different preloads and is influenced by factors such as the bearing geometry and the number of rolling elements. To plot the axial load-displacement curve for bearings, a code was developed based on this equation. The resulting curve provides valuable information for the design process. For example, a sample displacement curve for the bearing with plate number 1, which is used in Partner 2's spindle design, is shown in Fig. 30. This curve was plotted using the preload and corresponding axial rigidity values provided in the bearing catalog. Since the catalog only provides discrete data points, MATLAB's interpolation scheme was used to draw the complete

curve. The resulting curve closely follows the expected trend defined by the Hertzian point-contact relationship and is like the curves reported by bearing manufacturers.

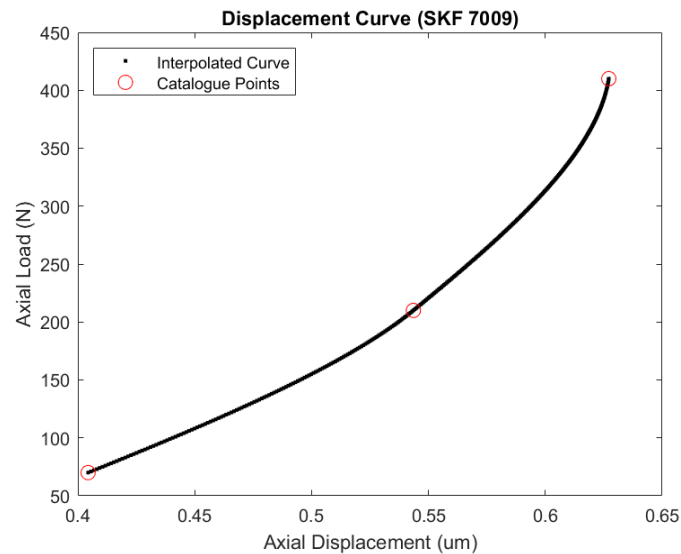


Fig. 3.30 Displacement Curve for Single Angular Contact Ball Bearing

When dealing with a spindle-bearing assembly that contains multiple bearings in various configurations, it's important to note that a single load-displacement curve for a single-row bearing won't suffice when determining the preload for the entirety of the shaft-bearing assembly. It's important to consider the size and direction of each bearing to understand how the bearing preload differs for individual bearings with the same amount of shaft displacement. To ensure each bearing is preloaded to its determined value, a step-by-step procedure is followed, including the calculation and method for preload as discussed in the following section.

Procedure for Preloading Bearings

The constant preload mechanism begins by rigidly preloading the front and rear bearing set to a certain value. Then, the spring preload is applied.

Step 1: Rigid/Position Preload

To properly preload the bearings, the first step takes place during the assembly of the spindle. This involves mounting the bearings onto the shaft in the correct configuration, without any external forces acting on them. It's important to note that the spring preloading assembly is not involved at this point. The inner rings of both bearing sets and the outer rings of the front bearing set are locked to the shaft and housing using stepped sleeves and shoulders. This ensures that the inner rings move axially with the shaft. The preload, which determines the extent of motion of the inner rings, is set by the gap designed between the bearing inner rings. Our design uses spacers of different widths between each bearing set to achieve this gap. Once all components are in place, a lock nut at the rear end is used to rigidly preload the bearings. As the nut is tightened, the shaft moves towards its back end, closing the gaps and ensuring the bearings are fully preloaded.

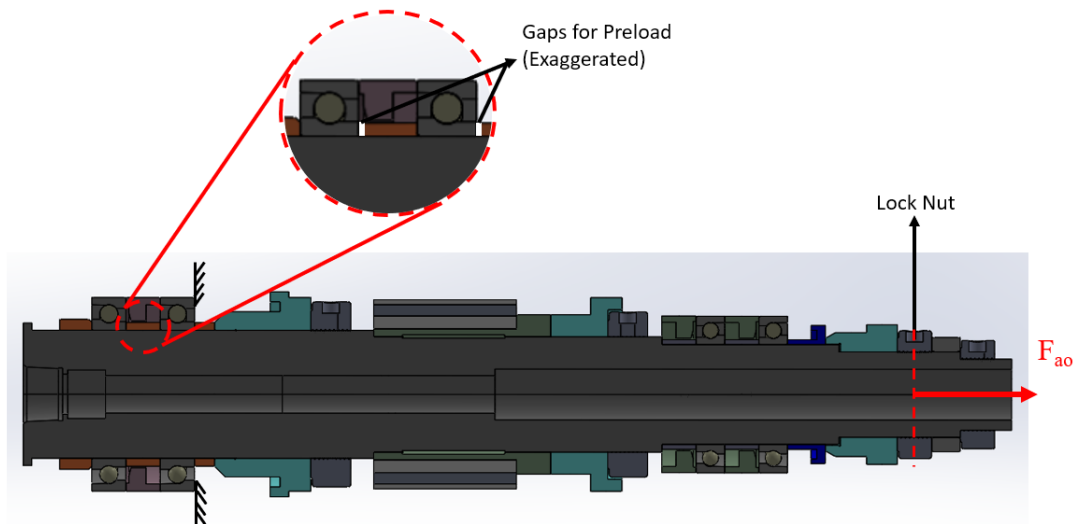


Fig. 3.31 Factory/Mounting Preload

The illustration in Fig 32 is analogous to a shaft-bearing system with back-to-back bearings. A-side represents the front bearing set, while B-side represents the rear bearing set. F_{a0} can be regarded as the rigid preloading force applied by the lock nut. δ_{a0A} and δ_{a0B} differ in spacer widths and outer rings at the front and rear bearing respectively. These are essential parameters from the design perspective.

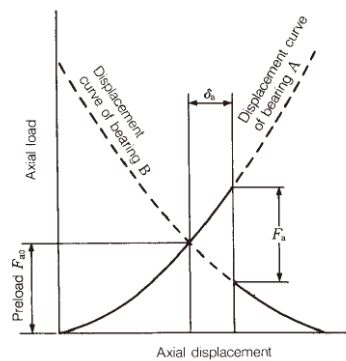
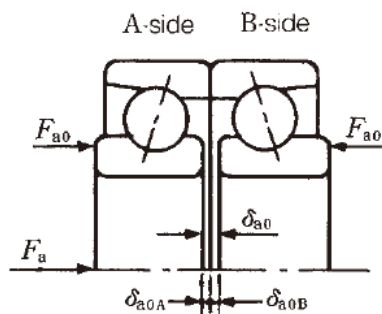


Fig. 3.32 Rigid Preloading in Back-to-Back (DB) Arrangement [60,61]

We have found that in our spindle design, the front and rear bearings require different sizes to induce the same preload force in both sets. This is necessary to achieve a self-balanced assembly. As a result, the values for δ_{a0A} and δ_{a0B} will not be equal. Additionally, because the front and rear bearing sets are arranged in tandem and assembled in groups of two each, the bearing curve equation becomes more complex.

$$\delta_a = 2c F_a^{2/3} \quad (4)$$

According to the instructions, it seems that the axial force required to displace the tandem bearing set is twice as much as the force required to displace a single bearing by the same amount. Using the code for bearing curves, we can plot the force-displacement curves of both the front and rear bearing sets for the chosen SKF bearings. Fig.33 shows the curves for both groups and the possible preload range. This range is defined by the minimum and maximum preload values that both sets can share. By selecting the preload from this chart, we can determine the correct values for δ_{aoA} and δ_{aoB} , which can be read from the respective plots of each bearing set. For instance, for the lowest possible preload of 140 N, δ_{aoA} and δ_{aoB} are 0.4044 μm and 0.47102 μm , respectively. It is worth noting that the preload values are determined for the duplex bearing set, which means that it is divided equally over individual bearings. Thus, 140 N indicates that each bearing receives 70 N, which must be displaced by δ_{aoA} or δ_{aoB} to achieve it. Also, it should be noted that these displacement values are not precise, as stated by the bearing manufacturers. They provide a general guideline for bearing displacements, and minor deviations are expected and will be adjusted by the manufacturing team during assembly. This step is also known as mounting preload and factory preload.

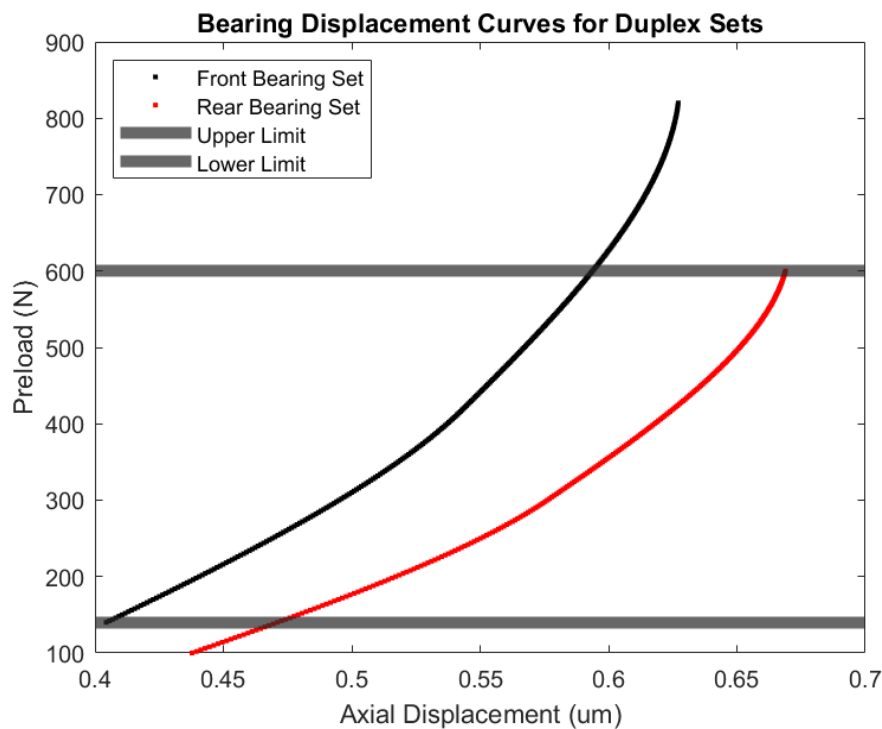


Fig. 3.33 Displacement Curves for Selected Front and Rear Bearing Sets

Step 2: Spring Preload

Once the correct preloads have been achieved through axial displacement, the spring preload is applied. This is done by assembling the spring preloading unit, which includes the soft spring and the floating mechanism for the rear bearing outer rings. This setup enables the outer rings of the rear bearings to move freely in the axial direction while keeping the inner rings fixed to the shaft. The soft spring has a much lower stiffness value than the bearing stiffness and is

designed to make the shaft-bearing system immune to thermal expansions and high-speed effects, as previously mentioned.

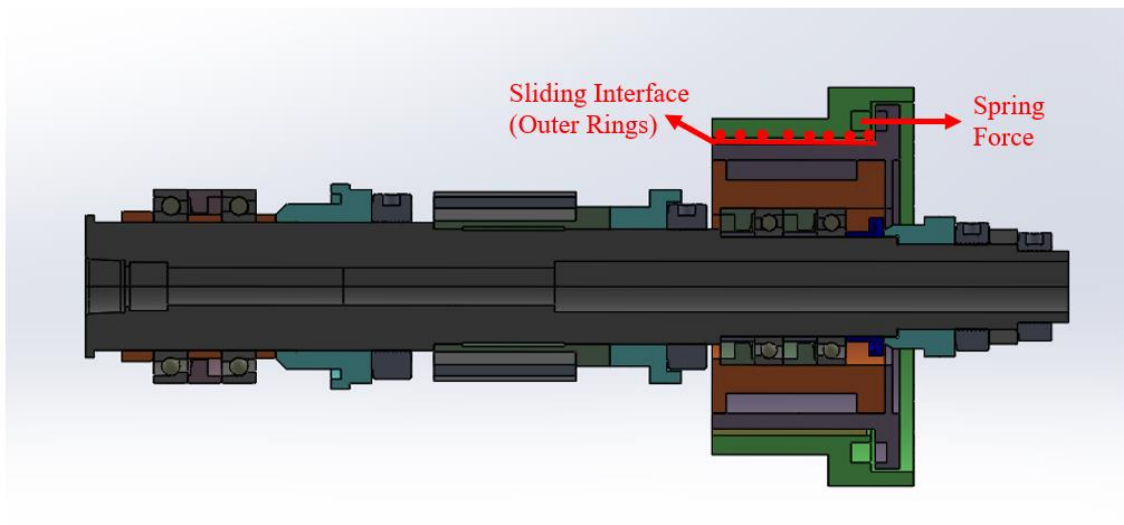


Fig. 3.34 Application of Spring Force

Step 3: External Preload

Finally, the front-side lock nut may apply additional preload to the system based on the functional requirements. All additional preload is devoted solely to the front bearing set as the rear bearing set is ‘floating.’

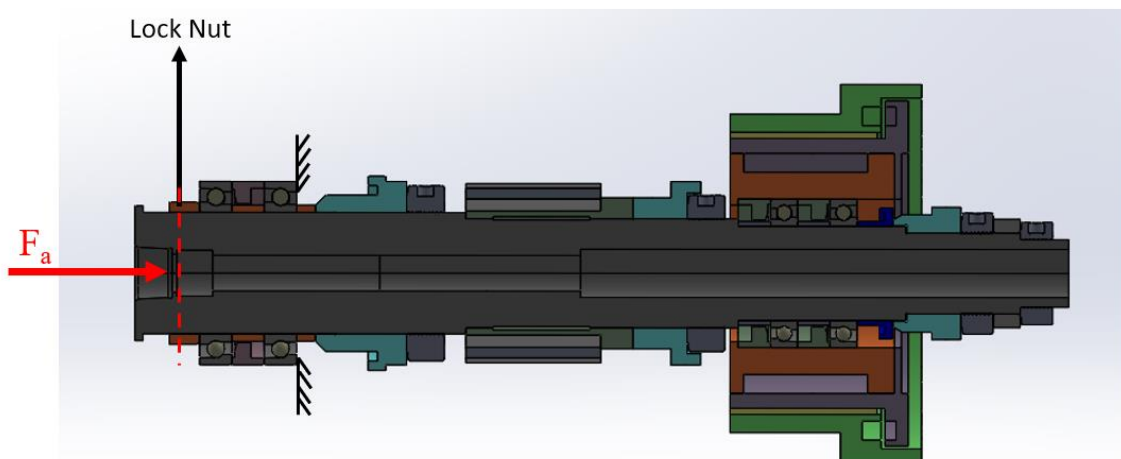


Fig. 3.35 Application of Additional Axial Preload

Fig 36, which is sourced from [61, 62], provides a clear illustration of the system's behavior at this point. The normal displacement curve, also known as bearing A, represents the front bearing set. Meanwhile, the flat line is indicative of the rear bearing set. What's interesting to

note is that the front bearing set maintains its preload regardless of the axial displacement. This is quite impressive. Additionally, any axial load above the mounting preload (F_{a0}) is situated in the region above the flat line, which is represented by the solid black curve.

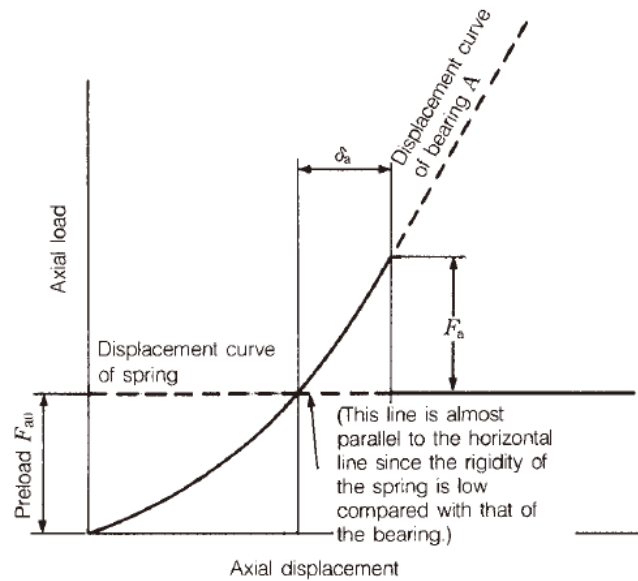


Fig. 3.36 Bearing Curves for Constant Preload Mechanism [61]

To ensure optimal performance for high-speed spindles, it is generally preferred to have a low preload value. This is because higher operating speeds can lead to excessive heat generation in the bearings, which can cause damage and reduce efficiency. However, to meet dynamic requirements and achieve higher stiffness, a higher preload value may be necessary. This creates an optimization problem with box constraints for the preload variables that are determined using the calculations mentioned above.

One exciting development in this field is the distinction between factory preload and external preload. With this knowledge, it is possible to set less conservative box constraints for the front bearing set, allowing for preloads above the mounting preload value. This was not previously applied to the optimization scheme, but it can help to achieve even better performance. However, it is important to note that the rear bearing set is strictly limited to the chosen mounting/factory preload value to ensure safe and reliable operation.

3.8.4.1. Case Study: Dynamic Optimization

In this case study, we explore the benefits of adopting updated box constraints in a revised dynamic FRF optimization problem. By using new box constraints that correspond to selected SKF super-precision bearings and the final spindle geometry, we can improve dynamic performance while achieving a lower optimized preload value than the base spindle. To accomplish this, we treat the front bearing preload as a variable, while defining the rear bearing preload as a constraint dependent on the front bearing preload. Additionally, we must set an upper limit for the factory preload, which in this simulation has been set to 150 N, roughly equal to the medium preload class developed by SKF. Ultimately, our goal is to demonstrate

that the combination of updated design and bearing selection, along with knowledge of the constant preload mechanism, can lead to improved performance in high-speed applications.

Min J(X): Max (Peak FRF Amplitude)

Max J(X): Natural Frequency of Max FRF Peak

s.t $50 < X(1)$: Front Bearing Preload < 331

X(2) = Rear Bearing Preload

if $X(1) < 150$

$X(2) = X(1)$

else

$X(2) = 150$

Table 3.2 FRF Optimization Results for Selected Bearings and Final Design

Property	Previous Value	Updated Value	Improvement
Preload	158 N	125 N	26.4%
Peak FRF Magnitude	1.12×10^{-7} m/N	1.02×10^{-7} m/N	9.8%
Peak FRF Mode Frequency	1203 Hz	2140 Hz	77.9%

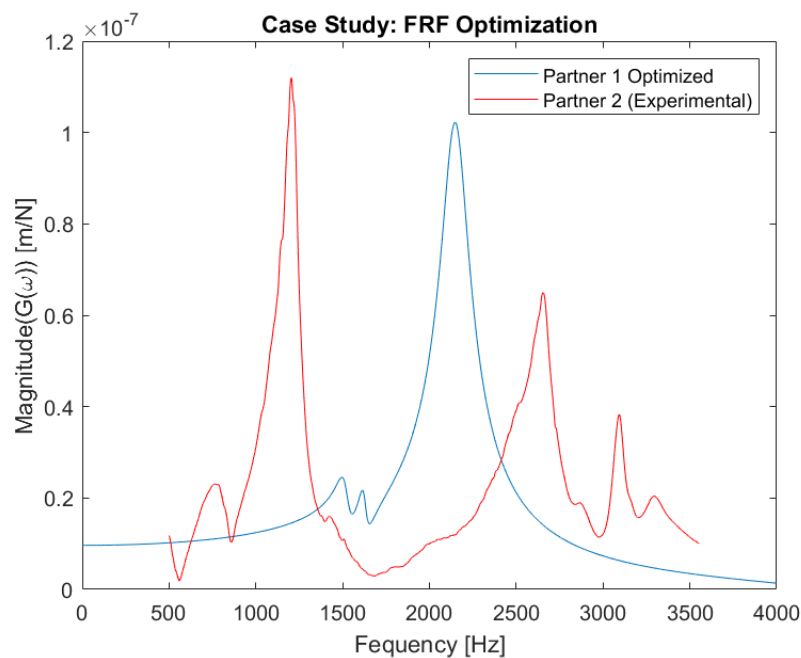


Fig. 3.37 FRF Comparison for MRL spindle with the base spindle

Based on the findings presented in Fig. 37 and Table 2, our new spindle design outperforms in all three key areas than the base spindle. We achieved this by incorporating high-precision SKF

bearings which are specifically designed for high-speed operation and have greater stiffness. Our preload value of 125N is lower than the base spindle's optimized value of 158N, resulting in lower heat generation and longer bearing life.

The FRF modal frequency is another area where our new design excels, thanks to the compact structure of the shaft and higher bearing stiffness. This has resulted in the dominant mode being shifted well away from the operational frequency range of 0-660 Hz, further improving the overall performance of our spindle design.

3.8.5. Cooling System Design Alternatives

Cooling Sleeve Internal Surface Design Alternatives

In the literature, there have been many different channel designs studied. These studies have concluded that the cooling channel geometry doesn't significantly affect heat transfer. However, it's been found that zigzag or tube-type designs can cause sharp pressure losses, which means a more extensive chiller system for these spindles. It's been noted that the helix-type design has the best properties concerning pressure drop and creating a surface area for heat transfer. When looking at well-established high-speed spindle manufacturers like DMG Mori, Kessler, Fisher, and Kitamura, it's been observed that all cooling channels were helix-based shapes. These helix-like shapes can be grouped as Helix Channel Design, Parallel Channel Design, and Quasi-Parallel Channel Design [63, 64]. For instance, Kitamura uses a helix shape design, while DMG Mori and Kessler use a quasi-parallel channel design with some heat transfer increasing design considerations. DMG Mori also uses a rough surface to improve the heat transfer area, while Kessler uses a fin-like structure for a quasi-parallel cooling channel design. You can see the design considerations shared in Fig.38.

a.) DMG Spindle with very high surface roughness



a.) Kessler Spindle with fin structures



Fig. 3.38 Cooling channel designs from different spindle manufacturers [65, 66].

Helix Cooling Channel Design

A helix cooling channel design alternative is applied to the final design for the maximum possible cooling sleeve dimensions. You can see the helix cooling channel in Fig.39. Based on the simulation results, the helix cooling sleeve seems to have a higher pressure drop than other design alternatives, but it offers very competitive heat transfer[. However, it's worth noting that including surface roughness in the calculations reduces the efficiency of the helix cooling system[64,67].

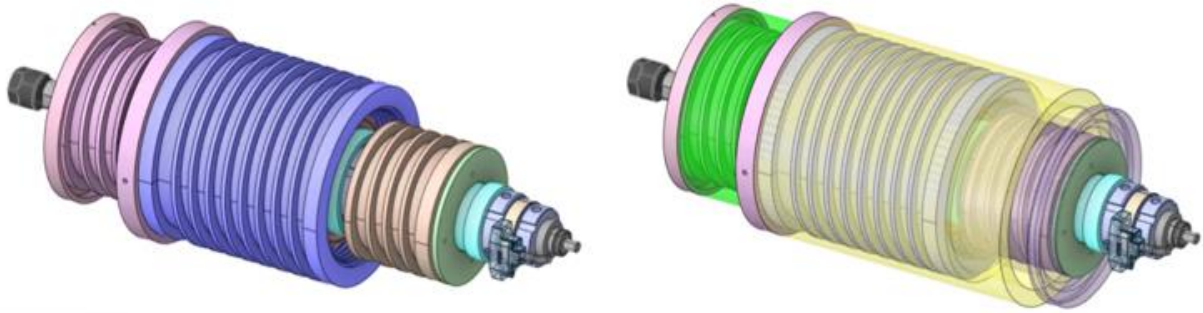


Fig. 3.39 Helix cooling channel designs

Parallel Channel Design

The parallel cooling design can be seen on Kessler and Kitamura spindles. These cooling channels have two fluid ways to feed simultaneously, and therefore, they require more significant chiller pressure than helix design. Thus, this cooling sleeve design is more convenient for high-torque and larger spindles. The parallel channel design is shared in Fig.40 for the final spindle design.



Fig. 3.40 Parallel cooling channel designs

Quasi-Parallel Channel Design

In the spindle industry, quasi-parallel channel designs are commonly used [67]. These designs have a more straightforward manufacturability compared to the helix cooling channel, resulting in lower pressure drops despite having two fluid ways [64]. Unlike parallel cooling channels, the fluid regions are not separated, and different liquid areas can easily mix. As a result, the pressure drop is reduced compared to parallel cooling channel designs. Another advantage of this quasi-parallel channel design is that the efficiency can be significantly improved with a high surface roughness. The best heat dissipation result is achieved with surface roughness values between 120 μm and 200 μm [63]. To see how this design is implemented, refer to Fig.41 which showcases the final spindle design.

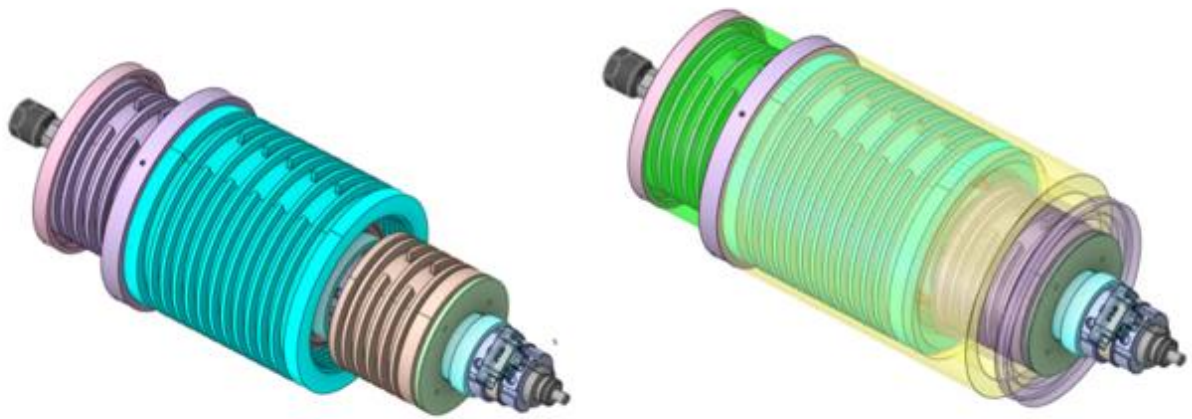


Fig. 3.41 Parallel cooling channel designs

Cooling Sleeve External Surface Design

Fin Type Design

The design of the cooling sleeve external surface for the electric motor has been a topic of interest in recent years[63]. A long winding length of 50mm for one side and the relatively thick distance between the stator and windings make it necessary to maximize the surface area for efficient cooling. To achieve this, 3D printable lattice structures were initially considered. However, a study in the literature proved that classical fin structures are more successful due to the chimney effect for heat dissipation [68]. Based on this study, classical fin structures were implemented between the cooling sleeve's external surface and motor windings. Calculations for fin efficiency showed that a minimum of 1.8mm length is required for natural convection-based cooling [69]. The fin width and height were set at 2mm by 2mm for the rear side of the motor, while the front fin's width is 2mm, and the length is 4.5mm at the area. The final design of the fin structures is shared in Fig.42.

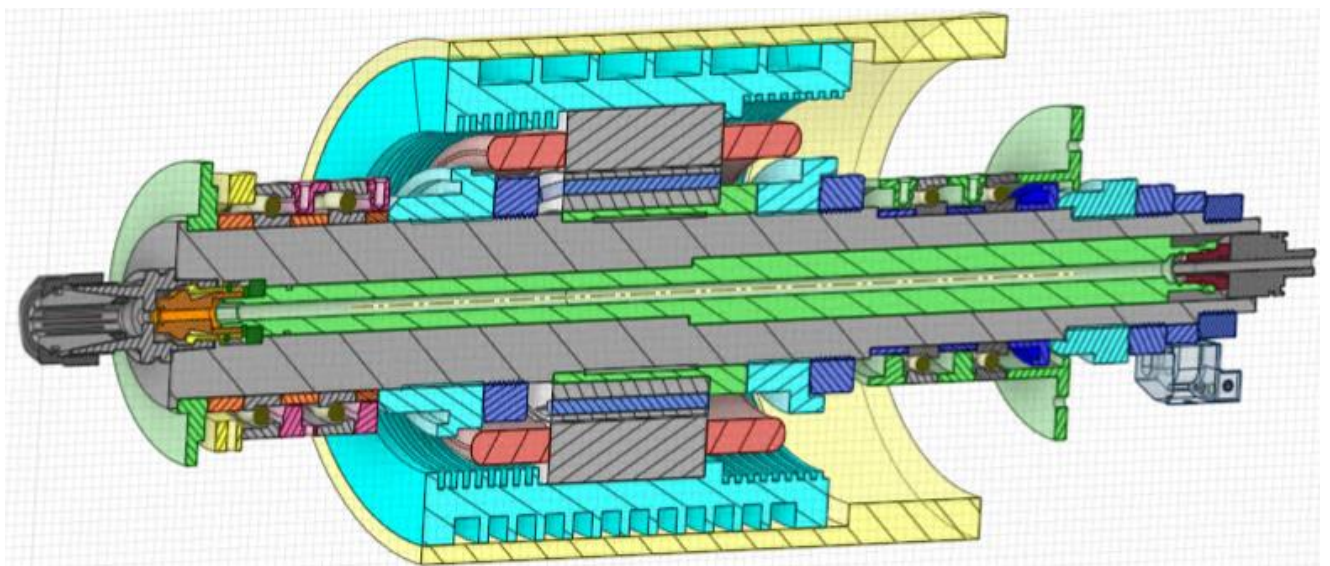


Fig. 3.42 The fin structure of the final cooling sleeve design

Pneumatic Inlets and Outlets Natural Convection Enhancements

We have found that the most efficient way to improve the fins with forced convection is to open the pneumatic inlets from the rear sides perpendicular to the rotor part [69]. By doing so, the pneumatic channels are aligned with the rotor and the most heat in the motor area is produced. The stationary air will be pressurized with the help of the pneumatic inlets, while the natural convection heat dissipation mechanism is converted to a forced natural convection mechanism [70]. We have also found that the pneumatic channels for forced natural convection shifts are given in Fig.43.

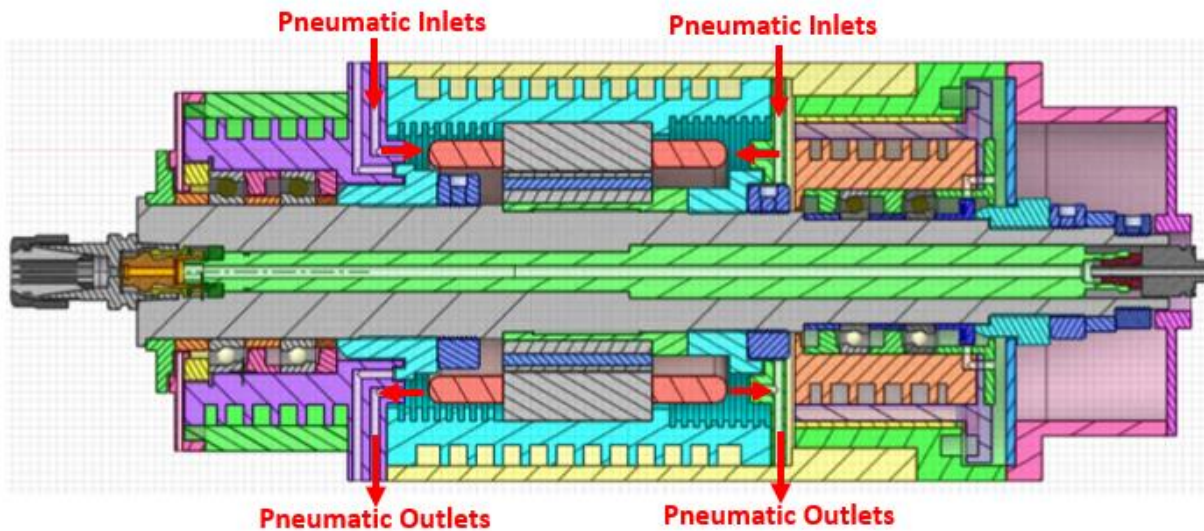


Fig. 3.43 The pneumatic inlets and outlets natural convection enhancement

3.8.6. Bearing Lubrication System

The selection of the bearing lubrication type will play a vital role in the spindle operation. Since the desired spindle speed is in the range of high-speed spindles, one cannot use grease-based lubricants for high speeds. The air-oil system can be the most primitive for a high-speed system. Using an air-oil system requires the design of nozzles and drainage chambers for spacers. SKF does not provide any information about oil nozzles and drainage chambers. The spacer oil-air nozzle information is taken from Koyo and NSK bearing catalogs [61,71]. There are two oil-air nozzles on a spacer. The first oil air nozzle is optimized for a 15-degree contact angle from the ball-bearing base points. The second oil-air nozzle targets the cage-ball bearing space. The oil-air nozzle diameter is 0.8 mm. The bearing lubrication inlets require M8 female thread opening with a 6-mm hose which has a 2.8-mm hole for the lubricant.

As shown in Fig. 44, labyrinth bearings and flinger/slingers must be employed to avoid leakage, and this system must have self-lubrication nozzles and drainage systems.

To compensate for possible thermal growth, a constant preload system at the rear bearings causes the design of sliding/mobile machine elements that share an interface with the outer rings of the rear bearings. Thus, the lubrication system of the rear bearings requires additional care. The safest solution is to design lubrication channels on sliding/mobile machine elements to avoid leakage among the component, as illustrated in Fig.45

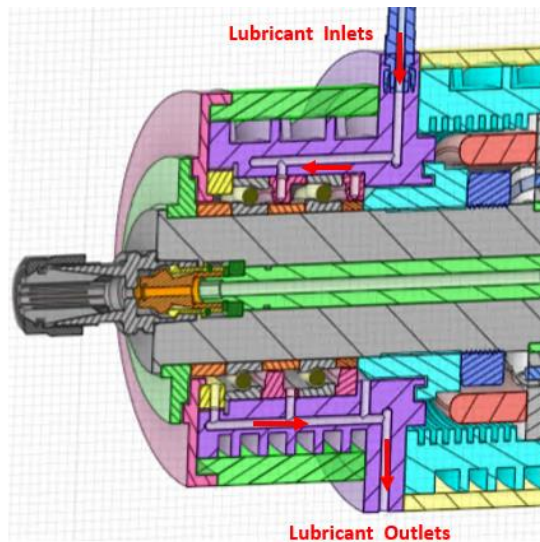


Fig. 3.44 The hydraulic inlets and outlets for the front bearing lubrication system

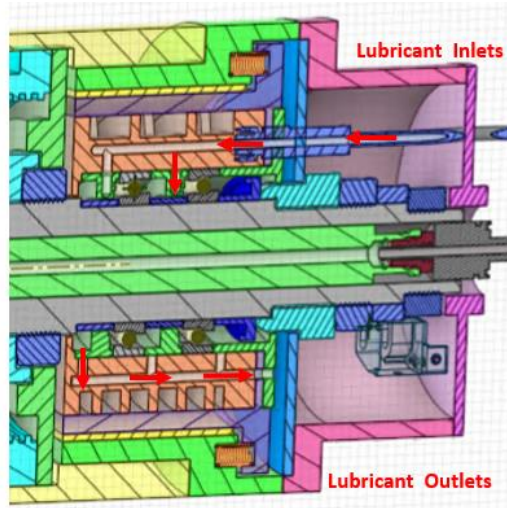


Fig. 3.45 The hydraulic inlets and outlets for the rear bearing lubrication system.

3.8.7. *Labyrinth Seals and Stepped Sleeve Designs*

3.8.7.1. Stepped Sleeves for Locking

In the design of certain mechanical systems, stepped sleeves are utilized as locknuts for bearings to enhance dynamic and static rigidity. Additionally, these sleeves can also be employed as sealing components for small spindles. Flange dimensions that are higher are known to facilitate the forced convection of the shaft and aid in heat dissipation. Within the final design phase, two stepped sleeves were utilized as locknuts for precision and accuracy. The first of these sleeves is responsible for fixing the front bearing, while the second sits closer to the motor and determines its location. You can see these stepped sleeves indicated in Fig. 46.

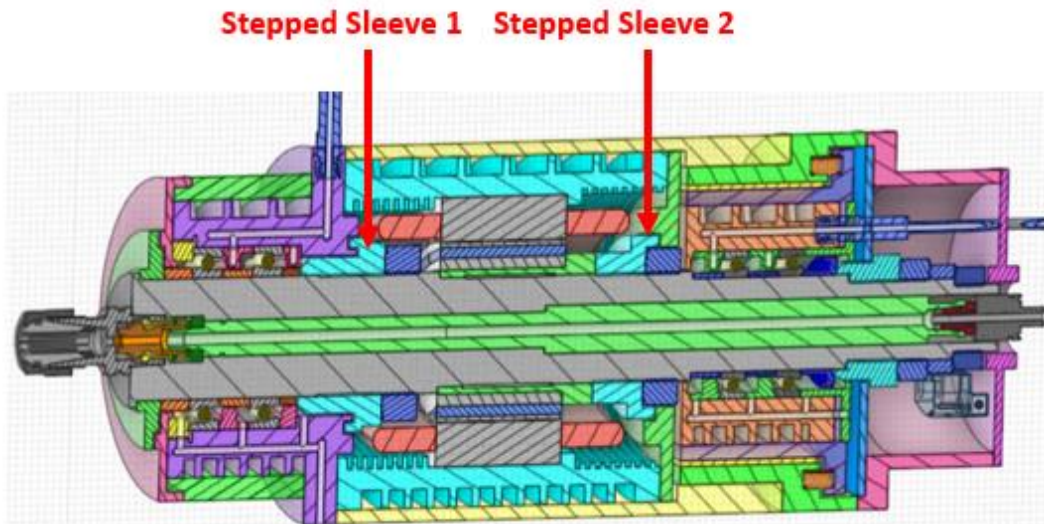


Fig. 3.46 The stepped sleeves for the final spindle design

3.8.7.2. Labyrinth Seals and Pneumatic Sealing Channels

The use of labyrinth seals can be an effective way to avoid solid and liquid particle splash and contamination. These seals consist of both rotor and stator parts, with the rotor part playing a key role in increasing forced convection and enabling heat dissipation. When designing a spindle, it is important to incorporate labyrinth seal structures for the front bearing, motor, and rear bearing regions to ensure maximum protection against contamination. In fact, Fig.47 shows how facilities can serve as a labyrinth seal with the help of pneumatic sealing channels. To ensure high-speed spindle applications are protected, pneumatic sealing channels with a diameter of 3mm are required. The only exception is at the front bearing area, near the balance ring, where the diameter is 2mm. Inlets and outlet regions are also included for the pneumatic sealing channels, and all these details can be found in Fig. 47.

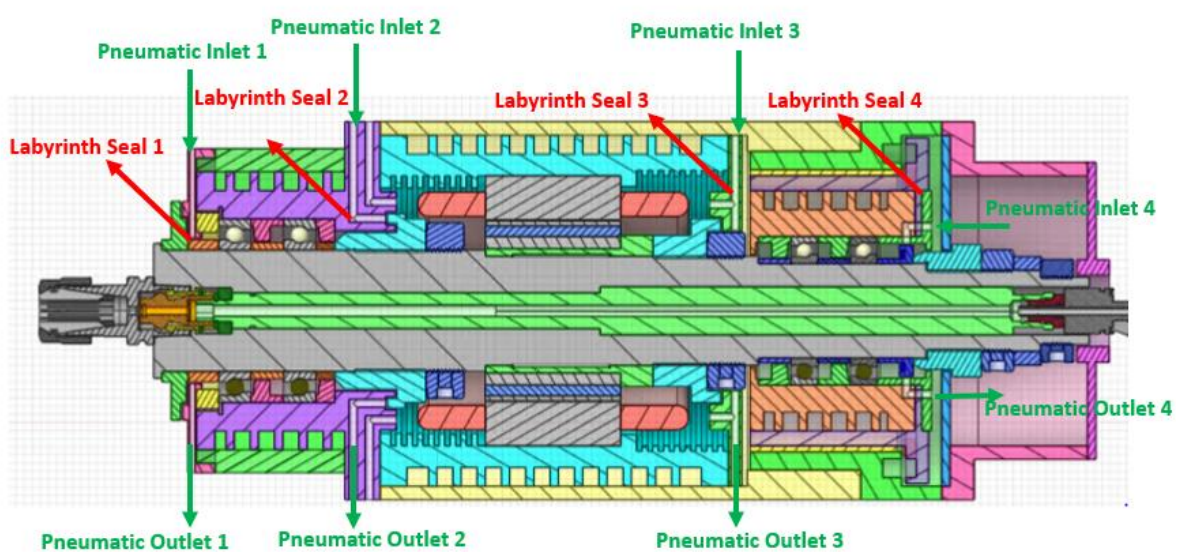


Fig. 3.47 The labyrinth sleeves and pneumatic inlet & outlets for the final spindle design

3.9. Conclusions

This study presents a conceptual design of an ultra-high-speed spindle without giving details of optimization studies. The fundamental requirements to draft a spindle shaft are introduced. The selection of fundamental components are as follows: Tool holder and collect, motor, cutting conditions, bearing selection, and drawbar selection. To draft the spindle shaft, the first bearings are selected based on a static analysis, and this static deflection analysis is taken as the base to determine the minimum shaft dimensions. A parametric analysis that sets double the minimum critical speeds based on Campbell diagrams determines the maximum shaft dimensions. Auxiliary spindle components are introduced, as well as fundamental components. The design of these auxiliary components also contributes to improving the spindle structure's dynamic and thermal behavior. For instance, a stepped sleeve fixes bearing positions and improves the dynamic rigidity via press-fitted surfaces on the shaft.

Additionally, since these elements are located on the rotating shaft, due to spinning, forced convection accelerates heat dissipation. The surface area positively affects the natural convection. A spindle design requires a trade-off between the dynamic and behavior, which involves a lot of iterations. One structural change result in a change in the entire structure. The final design of an ultra-high-speed spindle is presented by comparing a base spindle before the optimization. The effects of the structural changes on the whole structure tried to be demonstrated. The results are shared by elaborating on the bearing preload mechanism and cooling system together with the lubrication and pneumatic systems.

In this study, we have explored a conceptual design for a high-speed spindle, offering a wealth of technical information and manufacturing strategies for its successful implementation. We've also included a step-by-step guide on how to design and lay out a high-speed spindle, which can greatly enhance its structure. Practical design issues that commonly arise with high-speed spindles are also addressed and design parameters for optimal performance are outlined. This study is an invaluable resource for anyone seeking to create an efficient high-speed spindle.

4. VIRTUAL MODELLING OF A HIGH-SPEED SPINDLE STRUCTURE FOR OPTIMIZATION

4.1. Summary and Novelty

The virtual models of high-speed spindle structures (RCSA, bearing, and thermal ROMs (Reduced Order Models)) are assembled in a TLBO-based optimization platform for spindle design. The developed optimization platform is much more potent than other spindle optimization platforms since the ROMs can give FE simulation flexibility and power while offering the speed of analytical models. For instance, the dimensions of a spindle shaft and various press-fit auxiliary elements have a significant impact on the dynamic and thermo-mechanical behavior of machine tool spindles, which are complex dynamic systems under thermal growth. Although bearing-shaft optimization is a significant performance indicator for a spindle, the design of auxiliary shaft elements offers a considerable chance to optimize spindle performance more effectively. A study conducted a detailed sensitivity analysis on auxiliary components-shaft dimensions that most effectively enhance the frequency response function (FRF) and minimize thermal growth. The study formulated a multi-objective optimization problem to improve dynamic performance and thermal behavior, and optimization was achieved with the metaheuristic Teaching Learning Based Algorithm (TLBO). The optimization study revealed that the identified components could achieve a rigid spindle assembly by taking advantage of the mode-splitting phenomenon, lower thermal growth, and significant weight reduction.

4.2. Introduction

Dynamic and thermal behaviors are critical performance indicators for high-speed machine tool spindles. As thermomechanical devices are subject to dynamic cutting forces and have heat source components like bearings and motors, spindles are a principal candidate for improving the thermal and dynamic performance of machine tools. In spindle dynamics, the goal is to maximize rigidity, which is judged by the frequency response function (FRF) at the spindle tip. Specifically, the vibration amplitudes and natural frequencies of the dominant assembly modes in the FRF are strong contributors of structural rigidity. On the other hand, thermal behavior is linked to the spindle structure and dynamics through issues such as thermal growth and thermally induced bearing preloads. Li and Shin [1], in their benchmark study on the thermo-mechanical modeling of high-speed spindles, developed a modular approach to characterize the interactions between various thermal and dynamic behaviors occurring in a high-speed spindle. Their work also differentiated the effects of different bearing configurations and preloading mechanisms. Cao and Altintas [2] demonstrated the need for holistic spindle modeling by considering the effects of components like tool holder, housing, and machine mounting in their dynamic calculations. They concluded that considering such components increased modeling accuracy. The conclusion from [1] and [2] indicates the need to include auxiliary spindle shaft components in thermal and dynamic modeling. The auxiliary spindle shaft components may not directly be part of the shaft-bearing system but affect the structural behavior of the bearing-shaft system.

Design optimization of the spindle assembly has proven to be a promising method for achieving these goals. The literature on this topic can be classified based on the different structural

elements of spindles they have studied. The first, and initial, group focused on optimizing the non-linear bearing stiffnesses and their locations on the spindle shaft. In [3], a formulated classical optimization problem was formulated to compute the optimal bearing stiffnesses and locations for improving the static compliance and weight of a spindle structure. Tong et. al. [4] used the Particle Swarm Optimization (PSO) algorithm to optimize the static stiffness, natural frequencies, and friction torque of a spindle. They treated the bearing preloads and positions on the shaft as design variables in their optimization problem. In [5], a model was developed to study the effects of the interference fit between bearings and shaft on spindle dynamic characteristics. They found that a tighter fit stiffens the shaft. However, their study did not consider the thermal aspects associated with tight fits, as studied in [6]. An experimental thermo-elastic design optimization method was presented in [7], who treated the spindle housing diameter and length, bearing-housing clearance, and bearing span as structural parameters along with bearing preload and coolant temperature. Their optimization problem comprised both dynamic and thermal objectives/constraints. They noted, however, that most design variables were unchangeable in practical contexts.

The second branch of research in this area deals with structural modifications targeted at the most sensitive locations of the spindle with respect to thermal and dynamic performance. An inverse structural modification formulation based on analytical sensitivity analysis with respect to geometric dimensions of the constituent structural elements developed in [8]. They utilized classical gradient-based optimization in their case study problems to find the best dimensions and locations of additional structures required to cause the desired frequency shifts. Belotti et. al. [9] adapted a similar approach for dynamic optimization by introducing arbitrary auxiliary structures to an existing structure. Their homotropy optimization problem achieved inverse eigenfrequency assignment by varying the mass and stiffness of these auxiliary units. The intuition behind these theoretical structural modification methods have been applied in literature specific to spindles. Erturk et. al. [10] reported that the tooltip FRF of a given spindle assembly can be made more rigid by tuning the tool overhang and tool holder geometry. They also reported on the dynamic absorber effect observed when the length of the spindle's tail section is increased. The tail length tuning creates the dynamic absorber effect, where multiple modes merge and lessen each other's response in [11], a method to predict the chatter stability limits for parallel turning processes was developed. They demonstrated an improvement in the stability limits of the process by tuning the relative masses and lengths of both cutting tools to conform to specific natural frequency ratios. Fan et. al. [12] approached structural optimization from a thermal point of view. They optimized the material, contact pressure, and surface roughness of the sleeve between bearings and housing to minimize thermal elongation in a grinding spindle. It is a compelling example of how spindle auxiliary elements can contribute to the overall dynamic behavior of spindles under thermal growth.

4.3. Research Gap

This work aims to provide a spindle optimization problem and solution platform by including possible rotating auxiliary elements to alter a spindle shaft structure by considering dynamic and thermal behavior. Balancing dynamic and thermal performance is essential to achieve the best spindle design. To find the perfect balance, we have included rotating auxiliary elements such as stepped sleeves, bearing spacers, and labyrinth seals to alter the spindle shaft structure. These changes can improve the spindle shaft's shoulder, central hole, and tail, resulting in better

spindle performance. Our study is the first to explore the potential improvement of dynamic and thermal behavior through auxiliary elements in a high-speed spindle shaft.

4.4. Dynamic and Thermal Modelling

In this study, a quasi-static model for angular contact ball bearings (ACBBs) is presented and employed in dynamic and thermal models. The model assumes a fixed outer ring and a displacing inner ring under loading. This is the primary building block for both calculations. The RCSA is a practical tool that allows using different materials for the auxiliary elements, and it is used to predict spindle dynamics with composite Timoshenko beam theory. Furthermore, a quasi-static FE model is employed to predict thermal behavior.

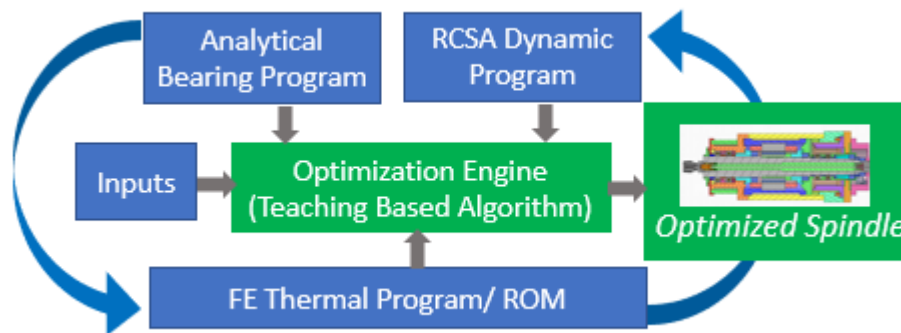


Fig. 4.1 The offered optimization components for dynamic and thermal behavior prediction

4.4.1. Bearing Modelling

Fig.2 shows the global coordinate system, the local coordinate system, and the free-body diagram for an arbitrary rotating element of an ACBB. In Fig. 2a, the external load vector, $\{F\}$, and the displacement vector, $\{\delta\}$, are defined respectively.

$$\{F\} = \{F_x, F_y, F_z, M_x, M_y\}^T, \{\delta\} = \{\delta_x, \delta_y, \delta_z, \gamma_x, \gamma_y\}^T \quad (1)$$

Fig. 2b demonstrates the displacement vector of the inner ring cross-section and the corresponding inner ring contact load vector defined at the local ball.

$$\{u\}^T = \{u_r, u_z, \theta\}, \quad \{Q\}^T = \{Q_r, Q_z, T\}, \quad (2)$$

Here, u_r, u_z, θ denote as the radial displacement, axial displacement, and rotation of the inner ring. Whilst Q_r, Q_z, T correspond to the radial and axial contact load, and the contact moment at the local ball. Fig. 1(c) displays the free-body diagram for the bottom ball of an ACBB. Here, Q_i and Q_e denotes the contact loads between the inner and outer rings, respectively. Their corresponding contact angles can be expressed as α_i and α_e . The centrifugal force F_c of the ball is expressed in Eq. 3. $m, d_m,$ and ω_c are the mass of a ball, bearing pitch diameter, and ball orbital speed. The gyroscopic moment M_g is expressed by Eq.4.

$$F_c = 1/2 m d_m \omega_c^2 \quad (3)$$

$$m_g = 1/10 m D_B^2 \omega_c \omega_r \sin \beta \quad (4)$$

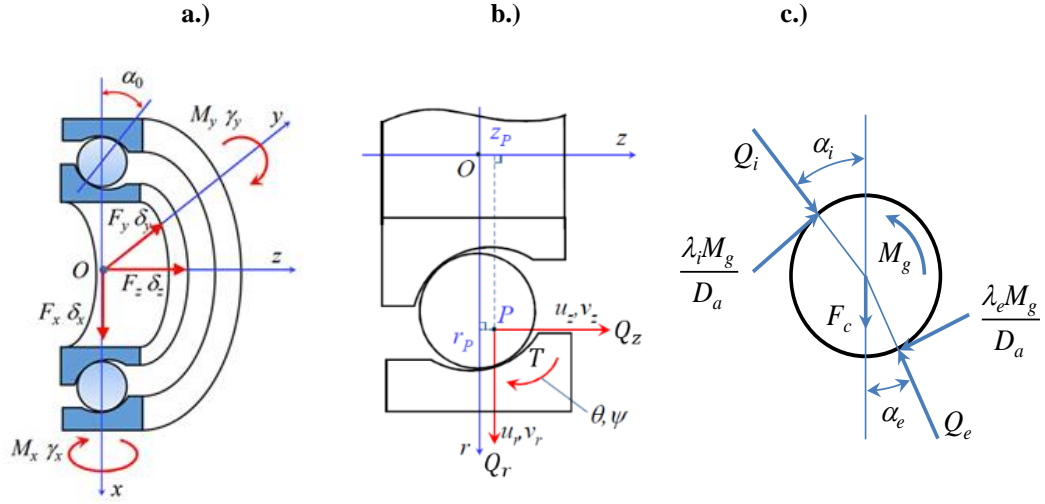


Fig. 4.2 Bearing coordinate systems and ball free-body diagram, a.) Global coordinate system, b.) Local coordinate system, and c.) Free-body diagram of the bottom ball.

D_B is the diameter of the ball, and ω_r and β are the ball's rotational speed and the pitch angle. The contact loads at ball-inner ring contact and the ball-outer ring contact are obtained from the Hertz contact theory as;

$$Q_i = K_i \delta_i^{1.5}, Q_e = K_e \delta_e^{1.5} \quad (5)$$

δ_i and δ_e stand for deformation between the inner ring and the ball and the outer ring and the ball, and K_i and K_e are the corresponding load-displacement proportional coefficients. From the free-body diagram in Fig2 c, the Eq.6 equation is obtained.

$$Q_i \cos(\alpha_i) - Q_e \cos(\alpha_e) + F_c - \frac{M_g}{D} (\lambda_i \sin(\alpha_i) - \lambda_e \sin(\alpha_e)) = 0$$

$$Q_i \sin(\alpha_i) - Q_e \sin(\alpha_e) - \frac{M_g}{D} (\lambda_i \cos(\alpha_i) - \lambda_e \cos(\alpha_e)) = 0 \quad (6)$$

λ_i and λ_e stand for the support ratios of the inner and outer rings to the gyroscopic moment. In a high-speed spindle it can be assumed that the outer race control mode is a rolling motion

based on the outer ring, leaving $\lambda_e=2$, otherwise $\lambda_i=\lambda_e=1$. The equilibrium equation for the entire bearing in the global coordinate system is indicated in Eq. 7.

$$\{F\} + \sum_{j=1}^Z [T_\psi]_j^T \{Q\}_j = 0 \quad (7)$$

Here, Z is the number of balls and $[T_\psi]_j^T$ is a transformation matrix from the center coordinates of the inner ring curvature radius to the global coordinates. Eq. 6 and Eq. 7 are non-linear, and Eq. 6 is obtained while solving Eq. 7. In this process, all displacements of the bearing center coordinates are calculated. The bearing stiffness is obtained from Eq. 7 as follows:

$$K = \frac{\partial \{F\}}{\partial \{\delta\}} = - \sum_{j=1}^Z [T_\psi]_j^T \left[\frac{\partial \{Q\}_j}{\partial \{u\}} \right] [T_\psi]_j \quad (8)$$

4.4.2. Dynamic Modelling

Receptance Coupling Substructure Analysis (RCSA)

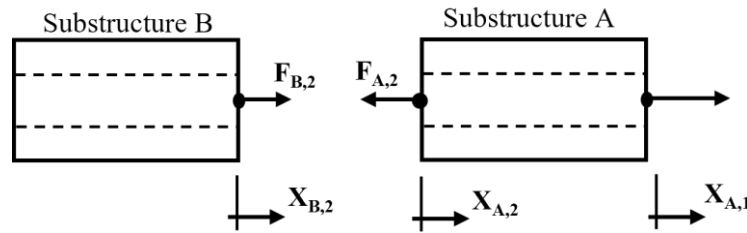


Fig. 4.3 Rigid coupling of two substructures

RCSA is an analytical method to predict mechanical assemblies' dynamic response, or the frequency response function (FRF), by joining their individual substructures' receptances. After it was first applied to machine tool spindles by [] to predict tooltip FRF, it has been adapted as a primary spindle dynamics analysis tool. The assembly response for the general receptance coupling equation for the two substructures in Fig. 3 is given by Eq. 9 []

$$\begin{Bmatrix} X_1 \\ X_2 \end{Bmatrix} = \begin{bmatrix} R_{A,11} - R_{A,12}(R_2)^{-1}R_{A,21} & R_{A,21} - R_{A,12}(R_2)^{-1}R_{A,22} \\ R_{A,21} - R_{A,22}(R_2)^{-1}R_{A,21} & R_{A,22} - R_{A,22}(R_2)^{-1}R_{A,22} \end{bmatrix} \begin{Bmatrix} Q_1 \\ Q_2 \end{Bmatrix} \quad (9)$$

The force function, Q , comprises the linear force and couple excitation at both ends of the substructure. The response, \bar{X} , is the corresponding linear and rotational displacements of the substructure. The square matrix components, $R_{a,ij}$, are the fully populated 2×2 matrices of the endpoint receptance of substructure a . The subscripts, i and j , are the points of response and excitation, respectively. In this study, these are numerically computed by solving the Timoshenko beam model [17] with free-free boundary conditions. They are of the form Eq. 10:

$$\begin{bmatrix} h_{ij} & l_{ij} \\ n_{ij} & p_{ij} \end{bmatrix} \quad (10)$$

The superscripts: h , l , n , and p , are the displacement-force, displacement-couple, rotation-force, and rotation-couple receptance functions of the corresponding substructure; respectively. For non-rigid connections such as shaft elements with bearings, the matrix R_2 is modified to include the bearing stiffness and damping matrix, K . The modified R_2 and K are given Eq. 11 and Eq. 12., respectively.

$$R_2 = R_{A,22} - R_{B,22} + K^{-1} \quad (11)$$

$$K = \begin{bmatrix} k_{yf} + i\omega c_{yf} & k_{\theta f} + i\omega c_{\theta f} \\ k_{ym} + i\omega c_{ym} & k_{\theta m} + i\omega c_{\theta m} \end{bmatrix} \quad (12)$$

The four stiffness values for populating the K matrix are extracted from the standard 5x5 bearing stiffness matrix. For damping, general values from literature are used.

4.4.3 Thermal Modelling

The FE model consists of heat sources as bearings and motor, heat sinks as a trough and shaft coolant, and thermal resistance mediums as auxiliary components, enlarging the forced convection area on the shaft. Bearing frictional moments of inner (M_i) and outer (M_e) rings are calculated for thermal modeling as indicated in Eq.13 and in [1]. f_o and f_1 changes with respect to bearing parameters and lubrication conditions while D is bearing diameter and γ kinematic viscosity.

$$M_i = \left[0.675f_o(\gamma\omega_c)^{2/3}D^3 + f_1(Q_i/Q_{i_max})^{1/3}Q_iD \right]$$

$$M_e = \left[0.675f_o(\gamma\omega_c)^{2/3}D^3 + f_1(Q_e/Q_{e_max})^{1/3}Q_eD \right] \quad (13)$$

Additionally, spin moments of the bearings at inner and outer rings (M_{si}) and (M_{se}) is calculated as shown in Eq. 14. μ_s is the friction coefficient, a_i and a_e are the major axes of the contact at bearing rings.

$$M_{si} = 3\mu_s Q_i a_i \zeta / 8, \quad M_{se} = 3\mu_s Q_e a_e \zeta / 8 \quad (14)$$

The heat generation from bearings according to Eq. 13 and Eq. 14 is given by Eq. 15. The calculated heat values are applied as boundary conditions in the FE model.

$$H_i = \omega_c \cdot M_i + \omega_{ri} \cdot M_{si}, \quad H_e = \omega_c \cdot M_e + \omega_{re} \cdot M_{se} \quad (15)$$

Another major heat source for a spindle thermal growth is the heat produced by built-in motor for high-speed electro spindles. There is not a well-established calculation method for motor heat prediction in the literature. In this study, an empirical heat generation formula was given by the step motor producer.

During the FE analyses, two types of heat sinks are considered. The first is heat dissipation due to forced convection at trough and shaft cooling regions. Forced convection coefficient(

h_{liquid}) inside the trough and shaft cooling hole is calculated by Eq. 16 and Eq. 17. In Eq. 16, Nu is Nusselt number, k_{liquid} is fluid conductivity, and D is flow cross-section of a tube. The Reynolds number is calculated by considering u (average speed of fluid) and η (fluid kinematic viscosity).

$$h_{liquid} = Nu \cdot k_{liquid} / D \quad (16)$$

$$Re = u \cdot D / \eta \cdot k_{liquid}, \text{ where } u = \sqrt{u_{axial}^2 + u_{radial}^2} \quad (17)$$

The second is thermal resistance mediums as auxiliary components, enlarging the forced convection area on the shaft. The forced convection coefficient outside of the shaft (h_{air}) is calculated by Eq. 18. and Eq. 19. ϑ_{air} is kinematic viscosity, and l_{shaft} is perimeter of the shaft assembly with auxiliary components. The Reynolds number is predicted by employing u_{air} (air speed around shaft) and depending on n which is spindle speed. These predicted forced convection coefficients are applied as boundary conditions to the FE model as well.

$$h_{air} = Nu \cdot \vartheta_{air} / l_{shaft}, \text{ where } l_{shaft} = \pi d_{shaft} \quad (18)$$

$$Re = u_{air} l_{shaft} / \vartheta_{air}, \text{ where } u_{air} = l_{shaft} \cdot n / 60 \quad (19)$$

These predicted forced convection coefficients are applied as boundary conditions to the FE model as well. The FE model is parameterized to reflect the design changes on the shaft (See Fig. 3.) and auxiliary components for optimization, and a reduced-order model is created. The bearing and electric motor cooling is not considered for this FE model and the shaft hole is 10.5 mm and parameterized as an input together with forced convection coefficients in the FE model.

4.5.Reduced Order Models (ROMs) for Optimization Studies

We are conducting a study to model and analyze the nonlinear and complex behavior of a high-speed spindle. To achieve this, we plan to create a digital twin by combining an analytical dynamic spindle model based on the receptance coupling method, and a thermo-mechanical bearing model based on an analytical and FE-based approach. A reduced order model, or surrogate model, will form the basis of the digital twin, which will allow us to simulate the spindle's behavior with online or offline inputs. Through this approach, we hope to gain a better understanding of the spindle's dynamic and thermal behavior, and ultimately improve its performance.

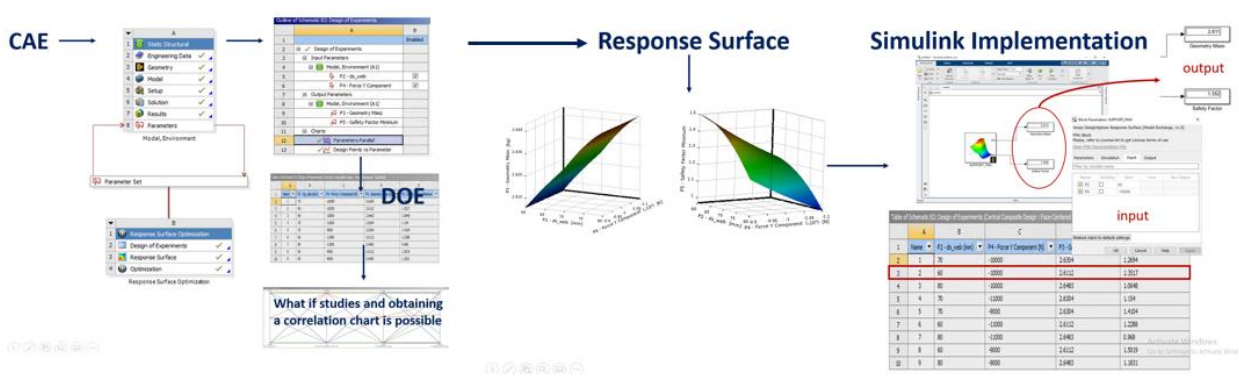


Fig. 4.4 The workflow from CAE to ROMs

We are working on optimizing the shaft cooling system for the new spindle design using the digital twin. To achieve this, we are combining the dynamics and thermal models in the Simulink environment. To reflect the complex spindle behavior, we plan to employ a thermal FE model for the optimization studies. However, analyzing different scenarios with different shaft dimensions is a time-consuming process. To reduce the necessary time and combine all the models in the Simulink environment, we created a Reduced Order Model (ROM) for the thermal FE model. We achieved this by creating response surfaces. We saved it as a functional mock-up unit (.fmu file). You can see the workflow we used to create a ROM for the optimization studies in Fig.4.

We created a FE model to produce ROM, which is demonstrated in Fig.5. To optimize shaft cooling, only the heat sources for the shaft were modeled. The bearings and electric motor were the specific heat sources that were considered.

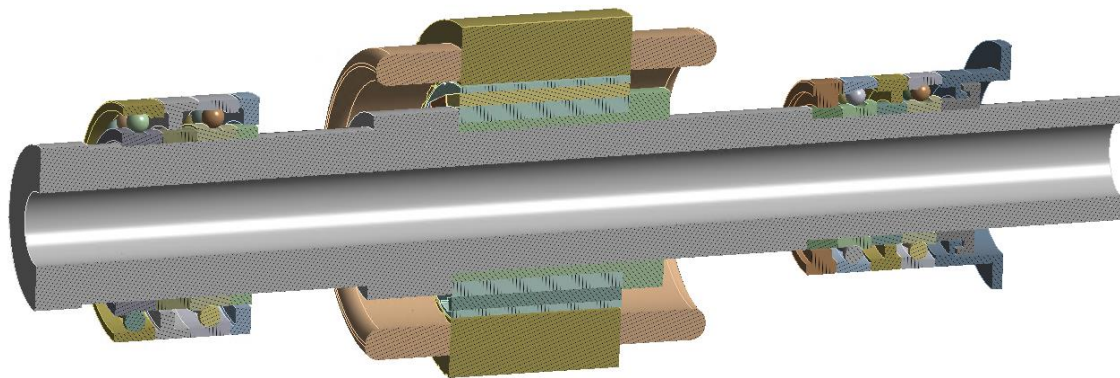


Fig. 4.5 The simplified shaft-bearing structure for ROM studies

Based on the FE model, it was found that the bearing and electric motor cooling were not taken into consideration. The primary FE model was justified with a hole radius of 10.5 mm. For the simulations, the shaft hole radius was parametrized as input. The outputs from the FE analysis were bearing and motor temperatures, thermal growth, and safety factors.

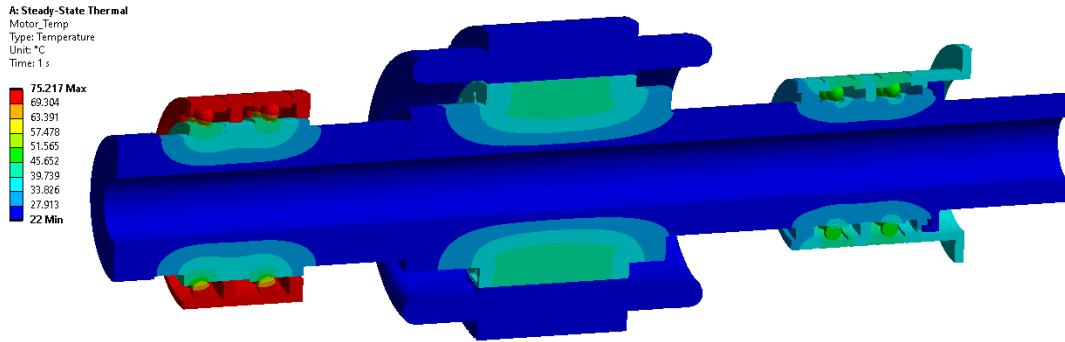


Fig. 4.6 The temperature distribution for shaft cooling for ROM studies (Only shaft cooling is considered.)

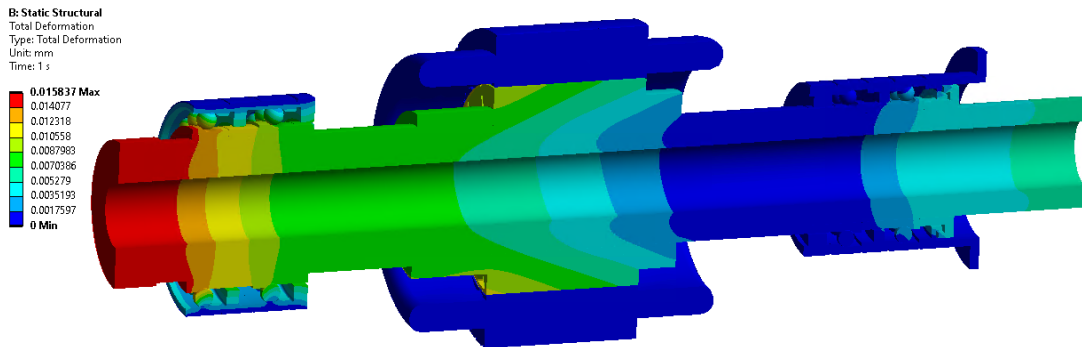
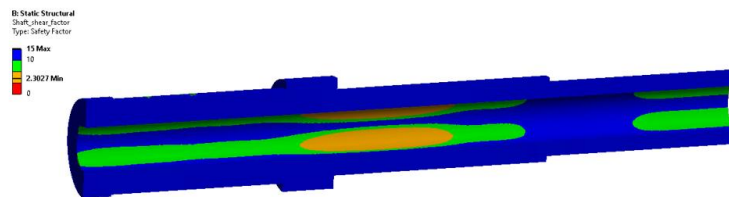


Fig. 4.7 The thermal growth for shaft cooling for ROM studies (Only shaft cooling is considered.)

We found some interesting information regarding the temperature distribution and thermal growth of a 10.5 mm shaft hole radius. Based on the FE analyses in Figs. 6 and 7, it seems that a giant shaft hole can increase the cooling capacity, which in turn reduces temperature gradients and thermal distortions. This could potentially be very useful in certain applications.

a.) Shear Safety Factor (sectional view)



b.) Shear Safety Factor (full view)

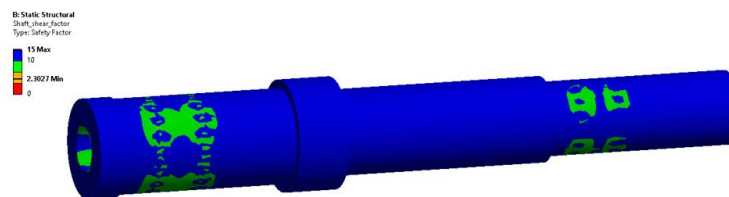
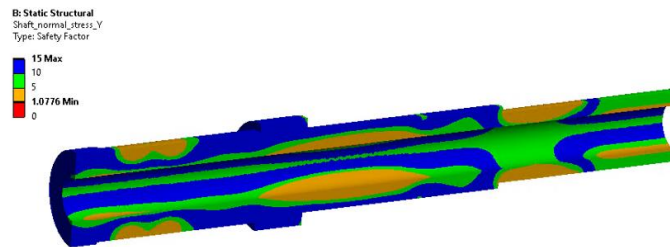


Fig. 4.8 The shear safety factor for ROM studies (Shaft Hole Radius:10.5 mm)

For our optimization study on a shaft cooling system, we found that a larger shaft hole radius can greatly improve thermal behavior for a spindle. However, we also took into consideration the safety factor when implementing larger shaft holes, as it can weaken the structure. To ensure safety, we added safety factors to limit the hole radius and examined the effects of thermal loading conditions on shear and normal stress.

a.) *Normal Safety Factor (sectional view)*



b.) *Shear Safety Factor (full view)*

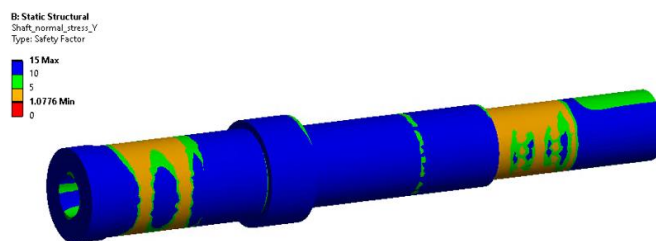


Fig. 4.9 The normal safety factor for ROM studies (Shaft Hole Radius:10.5 mm)

Based on the FE results for shear and normal stress safety factors for a 10.5 mm shaft radius, the new spindle design has a minimum shear safety factor of around 2.3. However, it's important to note that the parameterized FE results indicate that the shear safety factor behaves nonlinearly. Additionally, the minimum normal safety factor for the new spindle design is approximately 1.07, and the parameterized FE results show that the normal stress safety factor behaves nonlinearly like the shear stress safety factor. These findings suggest that further analysis and testing may be necessary to ensure optimal safety and performance for the spindle design.

4.6. Rotating auxiliary components and shaft design

When it comes to shaft assembly, there are a number of components that can impact both the dynamic and thermal performance of the system. Usually, it's the ones with higher mass or stiffness contributions that have the greatest impact. To really understand how each component contributes to the system, it's important to investigate their individual effects due to the inherent nonlinearity of the spindle dynamic system. One key indicator of this nonlinearity is the thermal response of each component, which is influenced by factors like the distance of heat sources and sinks in the spindle, as well as enforced convection caused by rotation. Some specific

components that can have a significant impact on performance include press-fitted sleeves (both stepped and motor sleeves), bearing spacers, preload locknuts, and shaft geometry.

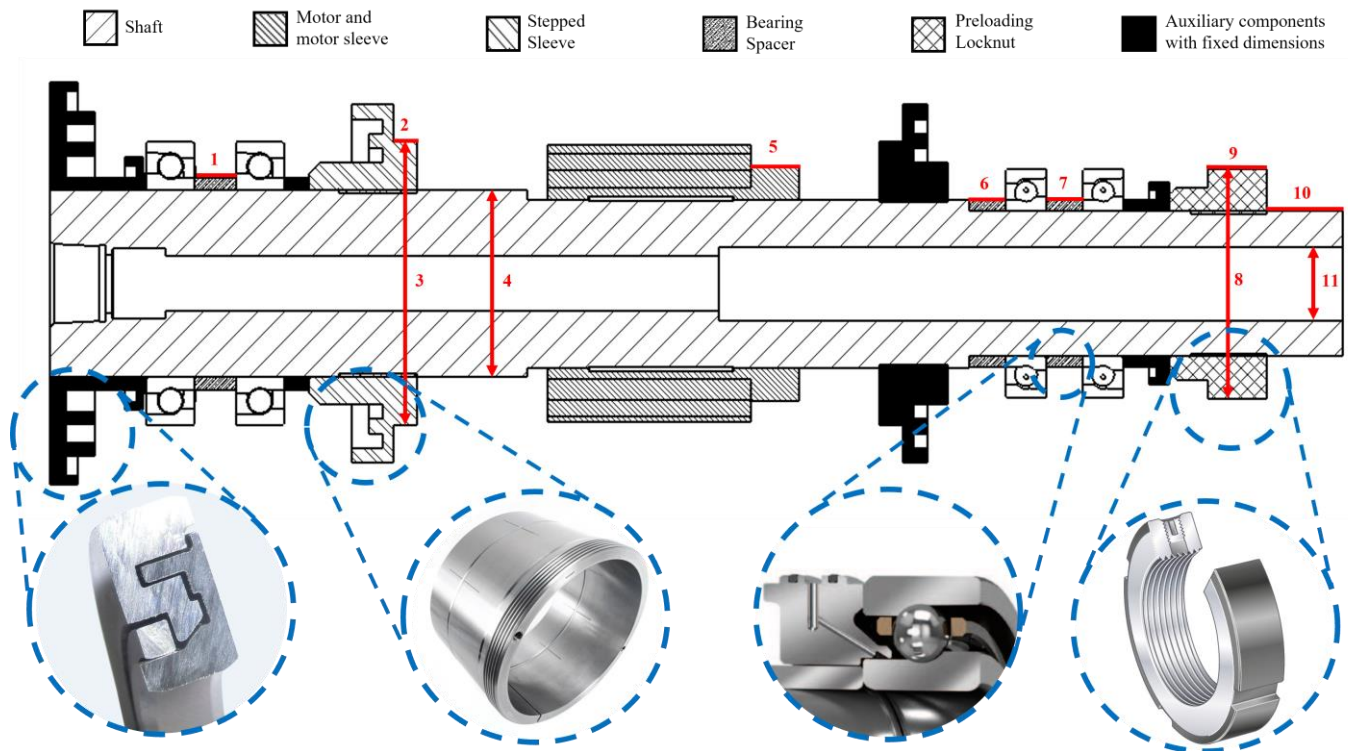


Fig. 4.10 Spindle shaft auxiliary components and adjustable dimensions

4.7.Sensitivity analysis

An in-house spindle design (see Fig.10) was used for this study. Although the nominal dimensions were chosen based on operational requirements and general design sense, eleven auxiliary and shaft dimensions were identified to be adjustable within certain bounds based on practical assembly constraints, as shown in **Error! Reference source not found.**

Table 4.1 Upper and lower bounds of variable dimensions

Variable No.	Variable Name	Lower Bound (mm)	Upper Bound (mm)
1	Front bearing spacer length	5	15
2	Front stepped sleeve length	5.75	25
3	Front stepped sleeve diameter	55	80

4	Motor shoulder diameter	45	65
5	Motor sleeve length	5	20
6	First rear spacer length	6	12
7	Second rear spacer length	6	12
8	Rear locknut diameter	40	70
9	Rear locknut length	15	35
10	Tail length	0	150
11	Shaft central hole diameter	10	30

4.7.1. Dynamic Sensitivity

When we alter the dimensions of a structure, it has a significant impact on its dynamic performance. This is because it changes the mass and stiffness of the structure. To better understand the impact of auxiliary rotating components, we can look at the FRF of a shaft assembly with and without these parts. As shown in Fig.11, the structure is more rigid when all the auxiliary components are included in the simulation. This highlights the importance of

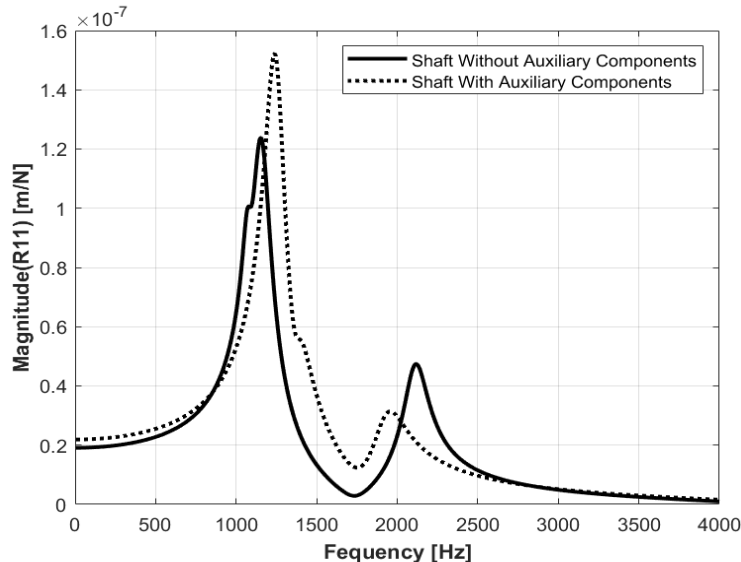


Fig. 4.11 Spindle-tip FRF with and without auxiliary components

considering all components when analyzing and designing structures for optimal performance.

In order to evaluate the dynamic performance indicators of natural frequency and FRF amplitude, a sensitivity analysis was conducted. This analysis aimed to determine the

individual effects of each variable dimension, and only one dimension was changed for each analysis, while the rest of the geometry remained constant. The performance indicators were checked at various points within the determined bounds, and the most significant change in each indicator was recorded for each variable. Fig 12 displays the sensitivities of each variable concerning both performance indicators, and a 5% change in dynamic behaviors was set as the minimum threshold for a dimension to be classified as 'sensitive.' The plot shows that six dimensions meet these criteria in Fig 11. The findings also reveal that the natural frequency is much less sensitive to change than the FRF amplitude, which offered more than $\pm 10\%$ change in some instances. However, the natural frequency remained unchanged for many cases. It is interesting to note that some of these sensitive dimensions are discussed further in the remainder of the section.

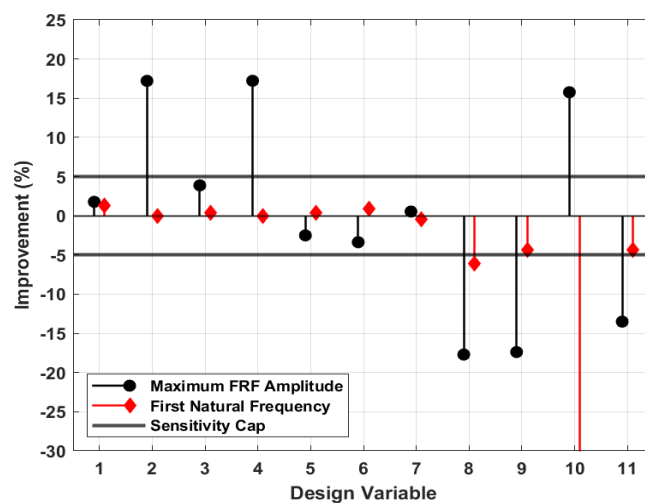


Fig. 4.12 Summary of sensitivity analysis

Front stepped sleeve and motor shoulder

Based on the data presented in Figure 10, it can be observed that the length of the front stepped sleeve and the diameter of the motor shoulder have a significant impact on the dominant FRF amplitude. These variables affect the same section of the shaft and therefore have a similar effect on the dynamic performance of the system. As shown in Figure 13, increasing the

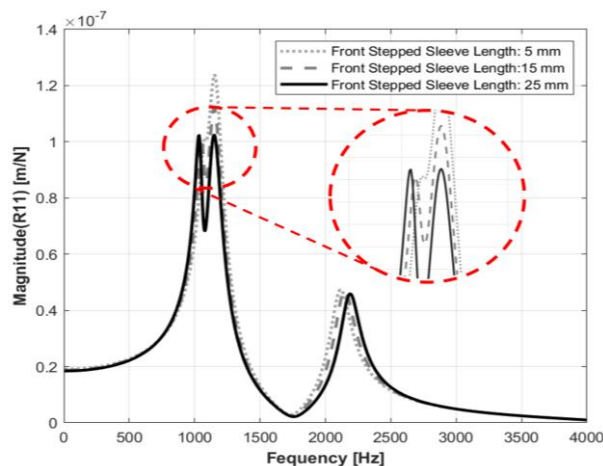


Fig. 4.13 Sensitivity of front stepped sleeve length

sleeve's length from 5 mm to 25 mm led to a reduction in the amplitude of the dominant peak by 17%. This can be attributed to mode-splitting phenomena, which caused the dominant mode to split into two minor modes with similar peak amplitudes. Although this may seem like a negative consequence, it leads to a decrease in dynamic vibration response, which is a desirable outcome.

Spindle tail components (shaft tail and preloading locknut)

In the sensitivity analysis, the diameter and length of the rear-side preloading locknut and the tail length were taken into consideration. The results were like those reported in the previous section, and adjustments to any of these dimensions can enhance spindle rigidity through mode splitting. The variation of tail length (variable 10) was particularly remarkable, where reducing the tail length from 20 mm to 0 mm led to a nearly perfect occurrence of mode splitting (Fig 14). This is different from previous reports, where elongating the tail was necessary to achieve the mode-splitting effect, adding significant mass to the assembly. By decreasing the tail length to 0 mm, a 2.5% weight reduction was achieved, which will positively affect general spindle performance. For example, the bearings will carry less weight, generating less heat, and the motor will be capable of higher acceleration due to experiencing lower rotational inertia.

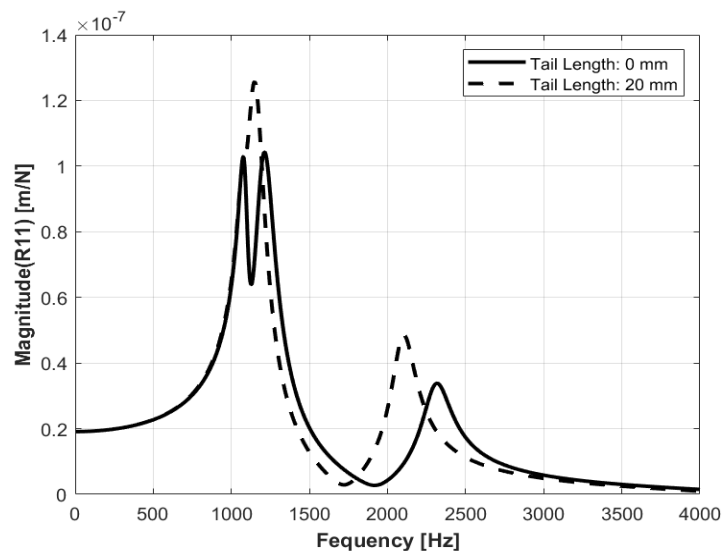


Fig. 4.14 Tail length sensitivity

Shaft central hole

When it comes to the spindle shaft, it's important to note that the hole at the center plays a crucial role in holding and actuating the tool holder. Not only that, but it also serves as a channel for through-cooling, which is responsible for delivering coolant to the cutting tool. Although the diameter of the shaft hole is not entirely free to change, it can still be adjusted to a certain extent by selecting the appropriate tool holder. For example, if a larger shaft hole is needed, designers could opt for the HSK-E 32 tool holder instead of the HSK-E 25 currently in use. It's worth noting that changing the diameter of the central hole can also improve dynamic performance indicators through mode splitting/modal interactions, as seen in Fig 15.

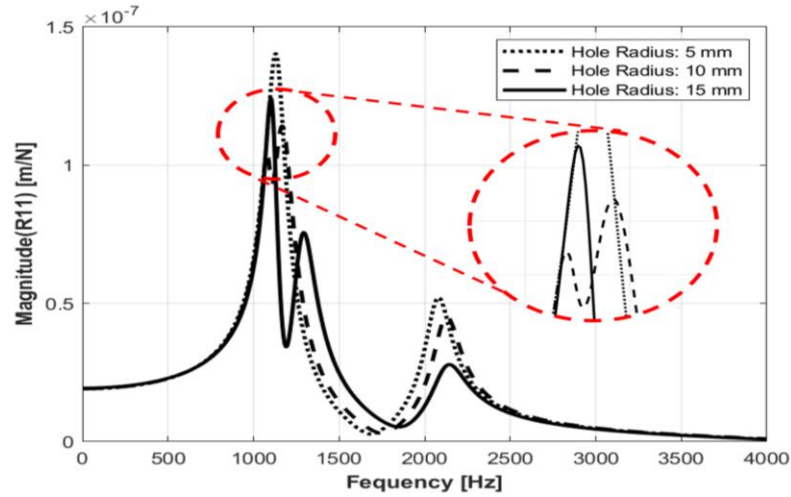


Fig. 4.15 Sensitivity of shaft hole radius

4.7.2. Thermal sensitivity

Based on the FE results, it has been found that the most influential variable for thermal performance is the central hole of the shaft. This is because it is an essential part of the cooling system. In Fig 16, you can see how these parameters change throughout the whole range of the central hole radius. Interestingly, it has been observed that the spindle-tip thermal growth and front-bearing temperature decrease as the hole radius increases. This is because a larger hole can accommodate more coolant, leading to a higher heat transfer rate. However, it is not practical to choose the maximum shaft hole radius as this would result in a loss of strength. The trends of shear stress and normal stress safety factors confirm this. Therefore, it is important to strike a trade-off between the thermal performance factors and stress safety factors. An appropriate balance between the two must be determined to make a sound design decision.

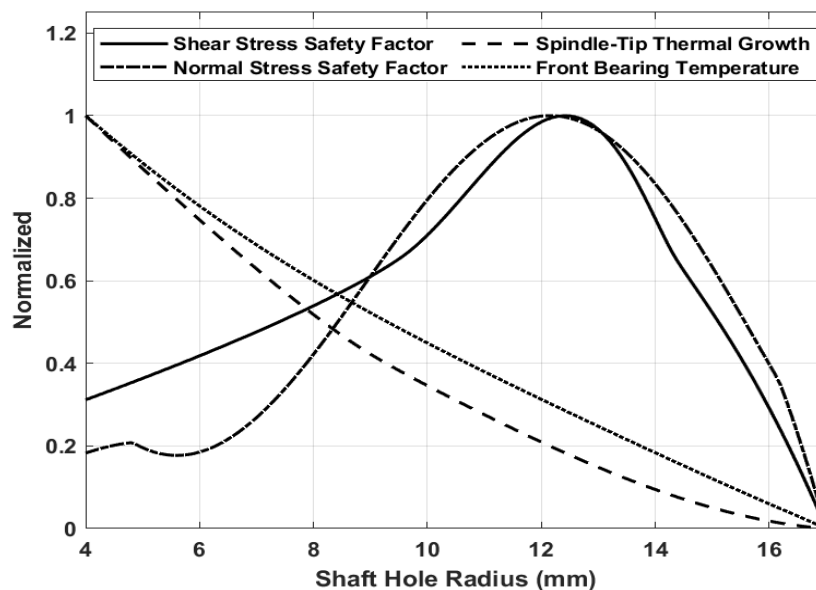


Fig. 4.16 Thermal sensitivity of shaft's central hole

4.8. Optimization case study

The thermal and dynamic effects of auxiliary components and shaft dimensions present a substantial opportunity for structural optimization. A multi-objective optimization case study was planned to use the findings of the sensitivity analysis performed above. Teaching-Learning Based Optimization (TLBO), a meta-heuristic algorithm introduced by Rao et al. in 2011 [18], was used to solve the optimization problem. Since multiple objectives were used, the niche-preserving and ranking mechanism of the Non-Dominated Sorting Genetic Algorithm-III (NSGA-III) [19] was adopted to identify Pareto optimal solutions. An external archive of these optimal solutions was maintained and updated each iteration to record the best answers. The archive size was set at 25 for this study. The formulated optimization problem was Eq. 19.

$$\begin{aligned} \text{Min} \quad & J(1): \max(|\mathbf{R}_{11}|) \\ \text{Min} \quad & J(2): 1/\omega_1 \\ \text{Min} \quad & J(3): \alpha_{\text{spindle-tip}} \\ \text{Min} \quad & J(4): m \\ \\ \text{s.t} \quad & 5.75 < X(1) < 12 \\ & 53 < X(2) < 65 \\ & 45 < X(3) < 70 \\ & 10 < X(4) < 20 \\ & 0 < X(5) < 150 \\ & 9.7 < X(6) < 14.5 \end{aligned} \tag{19}$$

In equation 19, we can see that the objective function matrix 'J' contains various parameters like the maximum FRF amplitude, first natural frequency, spindle tip thermal growth, and spindle mass. On the other hand, the design variable matrix 'X' has six components that include front stepped sleeve length, motor shoulder diameter, rear stepped sleeve length, back stepped sleeve diameter, tail length, and shaft central hole. To run the simulation, all objectives were normalized against their nominal values, and the simulations were performed at a speed of 40,000 RPM. It is important to note that while the bearing softening effects were included for this high-speed analysis, the shaft softening was ignored.

4.9. Discussion

The optimization simulation was carried out for 50 iterations with a population size of 25, and the Pareto front consisted of 25 Pareto optimal solutions. It was observed that the Pareto front was roughly divided into two clusters. In the first cluster, most solutions showed improvement in all four objectives, while the remaining solutions had worsened only in terms of the first modal frequency. The second cluster differed mainly from the first in the modal frequency objective. However, their performance for other objectives was quite like the solutions in the first cluster. This suggests that an additional mode appeared in the FRF in the lower frequency range for this group, which worsened their performance in the second objective. Despite this, their excellent performance in other objectives allowed them to remain part of the Pareto front. Since the first modal frequency is a crucial indicator of spindle performance, the remaining discussion will concentrate only on the first cluster of solutions.

The aim of finding Pareto optimal solutions is to understand the trade-offs between multiple performance indicators for the system in question and identify the best designs within their bounds. By using this knowledge, designers can choose the most optimal design that performs the best in their preferred performance objectives while maintaining decent performance in other areas. The best-performing solutions for each objective are presented in Fig 17 and Table 2 to identify the solutions for the spindle under study.

Table 4.2 Pareto optimal solutions

	Front Stepped Sleeve Length (mm)	Motor Shoulder Diameter (mm)	Rear Stepped Sleeve Diameter (mm)	Rear Stepped Sleeve Length (mm)	Tail Length (mm)	Shaft Hole (mm)	Maximum FRF Amplitude (m/N)	1 st Natural Frequency (Hz)	Spindle-tip Thermal Growth (µm)	Mass (kg)
Nominal Value	5.75	53	55	14.6	18.8	6.6	1.29×10^{-7}	1130	22.9	4.8
Optimal Solution 1	5.75	53	66	10	0	9.7	1.03×10^{-7}	1085	16.9	4.3
Optimal Solution 2	5.75	53	45	10	81.9	14.5	1.17×10^{-7}	1190	11.2	3.6
Optimal Solution 3	5.75	53	45	10	102.9	14.5	1.09×10^{-7}	965	11.2	3.7
Optimal Solution 4	5.75	53	45	10	0	14.5	1.21×10^{-7}	1185	11.2	3.4

After conducting extensive analysis, it has been determined that Optimal solution 1 provided the best dynamic performance in terms of FRF amplitude, which saw a significant decrease of 20.01%. The FRF algorithm was able to take advantage of the mode-splitting phenomenon, resulting in the appearance of two very similar modes. We also saw improvements in spindle-tip thermal growth and mass reduction, thanks to the giant shaft hole which allows for higher coolant flow and reduced assembly volume. However, the first natural frequency did experience a slight decline, which was anticipated due to the mode-splitting phenomenon. It's worth noting that the optimal value of the spindle tail length was also discovered during testing. While it's common to elongate the tail to achieve the dynamic absorber effect, our algorithm suggests that eliminating the tail portion altogether and converging to an optimal tail length of 0 mm may be the better approach. This finding has significant practical implications for spindle design, as longer tails can cause issues with unbalanced motion, assembling shaft components like the rotary union, and creating space for the spindle within the machine tool. Overall, Optimal solution 1 is the clear winner in terms of dynamic performance and practicality.

Based on the data analysis, it was found that Optimal solution 2 had the most significant increase in the first natural frequency, with an impressive improvement of 5.31%. This solution also resulted in a higher reduction in spindle-tip thermal growth and mass compared to Optimal solution 1. However, the FRF amplitude did not decrease significantly, and the dominant peak in the FRF plot indicated a potential interaction between two modes. The algorithm identified the higher frequency mode as the 'first' natural frequency. It should be noted that the tail length for this solution was 81.9mm, which is over four times longer than its nominal value, making it an impractical design. In such cases, it may be necessary to adjust the dimensions of other components comprising the tail, such as the rear stepped sleeve, to achieve a similar tail mass and dynamic performance. Another potential solution could be through appropriate material selection of the auxiliary components. Different densities and mechanical properties can be exploited to achieve optimal performance while maintaining practical design specifications.

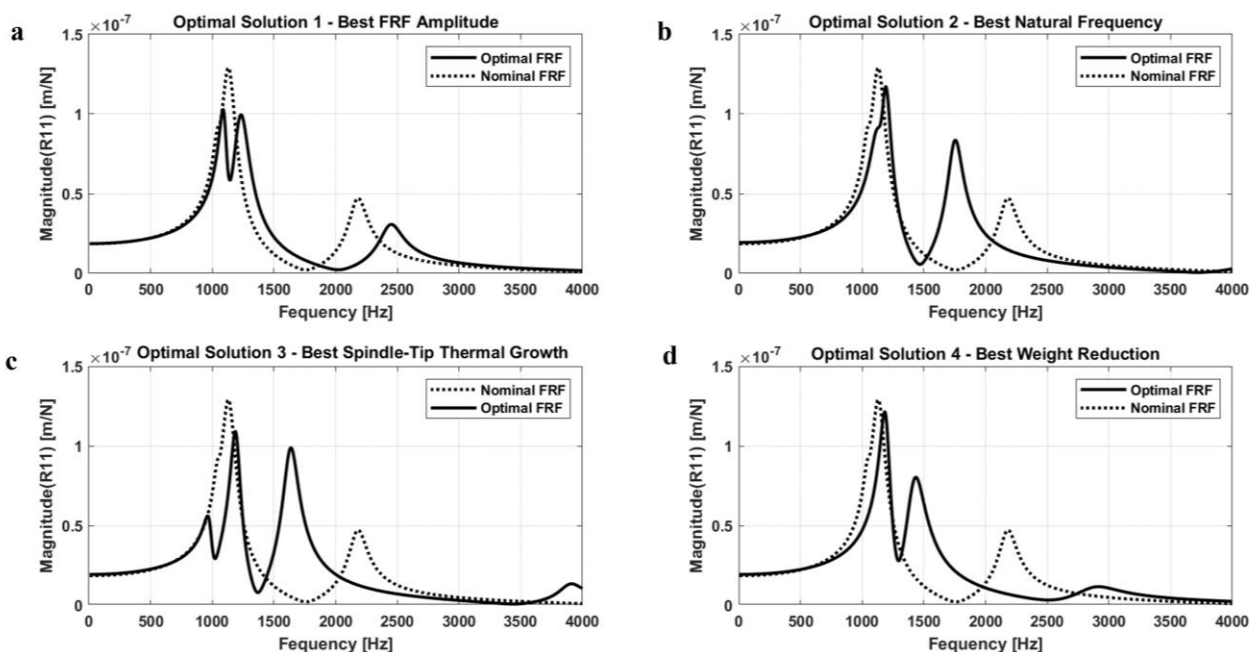


Fig. 4.17 FRF's of pareto optimal solutions

Overall, these findings demonstrate the importance of careful analysis and consideration of all factors when optimizing designs.

After careful analysis, it was found that optimal solution 3 had a significant decrease of 51% in spindle-tip thermal growth, which was reduced to 11.2 μ m owing to a giant shaft hole. Additionally, a similar situation was observed with the tail length, which measured 102.9mm. It is worth noting that the FRF displayed a minor vibration mode at 965 Hz, which is much lower than its nominal value. Therefore, if spindle designers prioritize minimal thermal growth and the spindle operating frequency is not within this range, this solution can be a viable option.

On the other hand, optimal solution 4 managed to achieve a mass reduction of 28.8% and had spindle-tip thermal growth equivalent to that of optimal solution 3. However, these achievements came at the cost of almost no change in dominant dynamic behaviors.

4.10. Conclusions

This study presented a spindle sensitivity analysis by including possible rotating auxiliary elements to shape a spindle shaft structure by considering dynamic and thermal behavior after optimization of bearing location during the design stage of a high-speed spindle. Some of the results can serve as design takeaways during the design of a spindle shaft and auxiliary elements, as summarized:

- In the literature, spindle tail length creates a mode-splitting/absorber effect. However, sensitivity analysis revealed that front-stepped sleeves and central shaft holes or adjusting these three parameters could create an absorber effect with better thermal stability.
- A short yet thick shaft design is generally advised in high-speed spindles. Thus, the tail length should be kept short, resulting in lighter spindle shafts that cause less heat generation, avoid dynamic problems, and lead to a smooth operation experience at high speeds. The sensitivity results revealed that adjusting the tail length to zero is possible with better dynamic and thermal behavior via the auxiliary elements.
- The auxiliary elements alter the spindle shaft and can be used to select and optimize the drawbar dimensions and tool holder selection by adopting a similar approach in this study.

However, the findings of this study are specific only to the spindle design and bearings used in this study. Furthermore, the presented methodology can serve as a preliminary study to identify suitable design variables for a systematic structural optimization framework.

5. REFERENCES

- 1) Budak, E., Matsubara, A., Donmez, A., & Munoa, J. (2022). Mechanical interfaces in machine tools. *CIRP Annals*, 71(2), 647-670.
- 2) Kikuchi, N., & Oden, J. T. (1988). *Contact problems in elasticity: a study of variational inequalities and finite element methods*. Society for Industrial and Applied Mathematics.
- 3) Kravchuk, A. S. (2009). The variational method in contact problems. The present state of the problem and trends in its development. *Journal of applied mathematics and mechanics*, 73(3), 351-357.
- 4) Fichera, G. (1972). Existence theorems in elasticity. In *Linear Theories of Elasticity and Thermoelasticity: Linear and Nonlinear Theories of Rods, Plates, and Shells* (pp. 347-389). Berlin, Heidelberg: Springer Berlin Heidelberg.
- 5) Panagiotopoulos, P. D. (1975). A nonlinear programming approach to the unilateral contact-, and friction-boundary value problem in the theory of elasticity. *Ingenieur-Archiv*, 44(6), 421-432.
- 6) Wriggers, P. (2006). *Computational contact mechanics* (Vol. 2). T. A. Laursen (Ed.). Berlin: Springer.
- 7) Wriggers, P. (2006). *Analysis and simulation of contact problems*. U. Nackenhorst (Ed.). Berlin/Heidelberg: Springer-Verlag.
- 8) Schmitz, T., Betters, E., Budak, E., Yüksel, E., Park, S., & Altintas, Y. (2022). Review and status of tool tip frequency response function prediction using receptance coupling. *Precision Engineering*.
- 9) Bendsøe, M. P., & Kikuchi, N. (1988). Generating optimal topologies in structural design using a homogenization method. *Computer methods in applied mechanics and engineering*, 71(2), 197-224.
- 10) Novotny, A. A., Sokołowski, J., & Źochowski, A. (2019). *Applications of the topological derivative method*. Springer.
- 11) Konyukhov, A., & Izi, R. (2015). *Introduction to computational contact mechanics: a geometrical approach*. John Wiley & Sons.
- 12) Konyukhov, A., & Schweizerhof, K. (2009). Incorporation of contact for high-order finite elements in covariant form. *Computer Methods in Applied Mechanics and Engineering*, 198(13-14), 1213-1223.
- 13) Liu, F., & Borja, R. I. (2010). Stabilized low-order finite elements for frictional contact with the extended finite element method. *Computer Methods in Applied Mechanics and Engineering*, 199(37-40), 2456-2471.
- 14) Galin, L. A. (2008). *Contact problems: the legacy of LA Galin* (Vol. 155). Springer Science & Business Media.
- 15) Kim, N. H. (2014). *Introduction to nonlinear finite element analysis*. Springer Science & Business Media.
- 16) Sanders, J. D., Dolbow, J. E., & Laursen, T. A. (2009). On methods for stabilizing constraints over enriched interfaces in elasticity. *International Journal for Numerical Methods in Engineering*, 78(9), 1009-1036.

- 17) Kim, T. Y., Dolbow, J., & Laursen, T. (2007). A mortared finite element method for frictional contact on arbitrary interfaces. *Computational Mechanics*, 39, 223-235.
- 18) Bendsøe, M. P., & Sigmund, O. (1999). Material interpolation schemes in topology optimization. *Archive of applied mechanics*, 69, 635-654.
- 19) Stolpe, M., & Svanberg, K. (2001). An alternative interpolation scheme for minimum compliance topology optimization. *Structural and Multidisciplinary Optimization*, 22, 116-124.
- 20) Yüksel, E., Budak, E., & Ertürk, A. S. (2017). The effect of linear guide representation for topology optimization of a five-axis milling machine. *Procedia Cirp*, 58, 487-492.
- 21) Zhang, W., & Niu, C. (2018). A linear relaxation model for shape optimization of constrained contact force problem. *Computers & Structures*, 200, 53-67.
- 22) Johnson, K. L. (1982). One hundred years of Hertz contact. *Proceedings of the Institution of Mechanical Engineers*, 196(1), 363-378.
- 23) Ertürk, A., Özgüven, H. N., & Budak, E. (2007). Effect analysis of bearing and interface dynamics on tool point FRF for chatter stability in machine tools by using a new analytical model for spindle-tool assemblies. *International Journal of Machine Tools and Manufacture*, 47(1), 23-32.
- 24) Yuksel, E., Erturk, A. S., & Budak, E. (2020). A hybrid contact implementation framework for finite element analysis and topology optimization of machine tools. *Journal of Manufacturing Science and Engineering*, 142(8), 081001.
- 25) Harris, T. A., & Mindel, M. H. (1973). Rolling element bearing dynamics. *Wear*, 23(3), 311-337.
- 26) Yüksel, E., Budak, E., & Ertürk, A. S. (2017). The effect of linear guide representation for topology optimization of a five-axis milling machine. *Procedia Cirp*, 58, 487-492.
- 27) Yalçın, T. K. (2016). Thermal modelling of high-speed machine tool spindles (Doctoral dissertation).
- 28) Altintas, Y., & Ber, A. A. (2001). Manufacturing automation: metal cutting mechanics, machine tool vibrations, and CNC design. *Appl. Mech. Rev.*, 54(5), B84-B84.
- 29) Engin, S., & Altintas, Y. (2001). Mechanics and dynamics of general milling cutters.: Part I: helical end mills. *International journal of machine tools and manufacture*, 41(15), 2195-2212.
- 30) Uriarte, L., Zatarain, M., Axinte, D., Yagüe-Fabra, J., Ihlenfeldt, S., Eguia, J., & Olarra, A. (2013). Machine tools for large parts. *CIRP annals*, 62(2), 731-750.
- 31) Schellekens, P., Rosielle, N., Vermeulen, H., Vermeulen, M. M. P. A., Wetzels, S. F. C. L., & Pril, W. (1998). Design for precision: current status and trends. *Cirp Annals*, 47(2), 557-586.
- 32) Slocum, A. H. (1992). *Precision machine design*. Society of Manufacturing Engineers.
- 33) Umbach, R. (1965). Problems of stiffness and accuracy of large size machine tools. *Proc. 6th International MTDR*, 99-122.

- 34) Do Suh, J., Kim, H. S., & Kim, J. M. (2004). Design and manufacture of composite high speed machine tool structures. *Composites Science and Technology*, 64(10-11), 1523-1530.
- 35) Mehta, K. P. (2019). Sustainability in welding and processing. *Innovations in manufacturing for sustainability*, 125-145.
- 36) Liu, S., Li, Y., Liao, Y., & Guo, Z. (2014). Structural optimization of the cross-beam of a gantry machine tool based on grey relational analysis. *Structural and Multidisciplinary Optimization*, 50, 297-311.
- 37) Altintas, Y., Brecher, C., Weck, M., & Witt, S. (2005). Virtual machine tool. *CIRP annals*, 54(2), 115-138.
- 38) Mayr, J., Jedrzejewski, J., Uhlmann, E., Donmez, M. A., Knapp, W., Härtig, F., ... & Wegener, K. (2012). Thermal issues in machine tools. *CIRP annals*, 61(2), 771-791.
- 39) Van Dijk, N. P., Maute, K., Langelaar, M., & Van Keulen, F. (2013). Level-set methods for structural topology optimization: a review. *Structural and Multidisciplinary Optimization*, 48, 437-472.
- 40) Murakami, T., Inoue, T., Shimura, H., Nakano, M., & Sasaki, S. (2006). Damping and tribological properties of Fe–Si–C cast iron prepared using various heat treatments. *Materials Science and Engineering: A*, 432(1-2), 113-119.
- 41) Li, B., Hong, J., & Liu, Z. (2014). Stiffness design of machine tool structures by a biologically inspired topology optimization method. *International Journal of Machine Tools and Manufacture*, 84, 33-44.
- 42) Eschenauer, H. A., & Olhoff, N. (2001). Topology optimization of continuum structures: a review. *Appl. Mech. Rev.*, 54(4), 331-390.
- 43) Stolpe, M., & Svanberg, K. (2001). An alternative interpolation scheme for minimum compliance topology optimization. *Structural and Multidisciplinary Optimization*, 22, 116-124.
- 44) Huang, X., & Xie, M. (2010). *Evolutionary topology optimization of continuum structures: methods and applications*. John Wiley & Sons.
- 45) Bendsoe, M. P., & Sigmund, O. (2003). *Topology optimization: theory, methods, and applications*. Springer Science & Business Media.
- 46) Abele, E., Altintas, Y., & Brecher, C. (2010). Machine tool spindle units. *CIRP annals*, 59(2), 781-802.
- 47) Cao, Y., & Altintas, Y. (2004). A general method for the modeling of spindle-bearing systems. *J. Mech. Des.*, 126(6), 1089-1104.
- 48) Altintas, Y., & Cao, Y. (2005). Virtual design and optimization of machine tool spindles. *CIRP annals*, 54(1), 379-382.
- 49) Cao, H., Holkup, T., & Altintas, Y. (2011). A comparative study on the dynamics of high speed spindles with respect to different preload mechanisms. *The International Journal of Advanced Manufacturing Technology*, 57, 871-883.
- 50) Maeda, O., Cao, Y., & Altintas, Y. (2005). Expert spindle design system. *International journal of Machine tools and Manufacture*, 45(4-5), 537-548.

- 51) Li, H., & Shin, Y. C. (2004). Analysis of bearing configuration effects on high speed spindles using an integrated dynamic thermo-mechanical spindle model. *International Journal of Machine Tools and Manufacture*, 44(4), 347-364.
- 52) Jorgensen, B. R., & Shin, Y. C. (1997). Dynamics of machine tool spindle/bearing systems under thermal growth.
- 53) Li, H., & Shin, Y. C. (2004). Integrated dynamic thermo-mechanical modeling of high speed spindles, part 1: model development. *J. Manuf. Sci. Eng.*, 126(1), 148-158.
- 54) Rao, J. S. (1996). Rotor dynamics. New Age International.
- 55) <https://www.heidenhain.com/>
- 56) <https://www.rls.si/eng/spinco-incremental-magnetic-encoder-system>
- 57) Cao, H., Zhang, X., & Chen, X. (2017). The concept and progress of intelligent spindles: a review. *International Journal of Machine Tools and Manufacture*, 112, 21-52.
- 58) <https://www.fischerspindle.com/en/technology>
- 59) Cao, Y. (2006). Modeling of high-speed machine-tool spindle systems (Doctoral dissertation, University of British Columbia).
- 60) Ohura, Y., Katsuno, Y., & Sugita, S. (2000). Robust series high-speed precision angular contact ball bearings for machine tool spindles. *EA Spherical Roller Bearings*, 7.
- 61) NSK. (2013). Technical Report CAT. No. E728g. <https://www.nsk.com/common/data/ctrGpdf/bearings/e728g.pdf>
- 62) FAG Catalogue. (2008). Super Precision Bearings AC 41 130/7 EA. https://www.schaeffler.com/remotemedien/media/_shared_media/08_media_library/01_publications/schaeffler_2/brochure/downloads_1/ac_41130_7_de_en.pdf
- 63) J Denkena, B., Bergmann, B., & Klemme, H. (2020). Cooling of motor spindles—a review. *The International Journal of Advanced Manufacturing Technology*, 110, 3273-3294.
- 64) Weber, J., Shabi, L., & Weber, J. (2018). State of the art and optimization of the energy flow in cooling systems of motorized high-speed spindles in machine tools. *Procedia Cirp*, 67, 81-86.
- 65) <https://www.dmgmori.co.jp/en/theme/movie/id=6027>
- 66) <https://kessler-group.biz/en/spindle-technology/milling/>
- 67) Satrustegui, M., Martinez-Iturralde, M., Ramos, J. C., Gonzalez, P., Astarbe, G., & Elosegui, I. (2017). Design criteria for water cooled systems of induction machines. *Applied Thermal Engineering*, 114, 1018-1028.
- 68) Krishnan, S., Herson, D., Hodes, M., Mullins, J., & Lyons, A. M. (2011). Design of complex structured monolithic heat sinks for enhanced air cooling. *IEEE Transactions on Components, Packaging and Manufacturing Technology*, 2(2), 266-277.
- 69) Ellison, G. (2010). Thermal computations for electronics: conductive, radiative, and convective air cooling. CRC press.
- 70) Hyeon, S., Kim, C., & Lee, K. S. (2022). Thermal enhancement of an air-cooled motor with a flow guide. *International Journal of Heat and Mass Transfer*, 183, 122228.

71) <https://koyo.jtekt.co.jp/en/support/catalog-download/uploads/catb2005e.pdf>